An Integrated Shale Oil Characterization Workflow for Hydrocarbon Gas Huff-n-Puff Candidates

By

Sherifa Enna Cudjoe

M.S., New Mexico Institute of Mining and Technology, 2014

B.Sc., Kwame Nkrumah University of Science and Technology, 2011

Submitted to the graduate degree program in Chemical and Petroleum Engineering and the Graduate Faculty of the University of Kansas in partial fulfillment of the requirements for the degree of Doctor of Philosophy.

Committee:

Chair: Dr. Reza Barati

Dr. Anil Misra

Dr. John Doveton

Dr. Shapour Vossoughi

Dr. Russ Ostermann

Dr. Jyun-Syung Tsau

Dr. Georgios Tsoflias

Date Defended: _____

The dissertation committee for Sherifa Enna Cudjoe certifies that this is the approved version of the following dissertation:

An Integrated Shale Oil Characterization Workflow for Hydrocarbon Gas Huff-n-Puff Candidates

Committee:

Chair: Dr. Reza Barati

Dr. Anil Misra

Dr. John Doveton

Dr. Shapour Vossoughi

Dr. Russ Ostermann

Dr. Jyun-Syung Tsau

Dr. Georgios Tsoflias

Date Approved: _____

ABSTRACT

The complexity of unconventional shales is inherent in the variation of mineral micro-structure and heterogeneous pore space, which contributes to the fast decline of primary oil production in shale oil reservoirs resulting in small recovery factors (< 10%). Furthermore, the implementation of hydrocarbon gas huff-n-puff has proven to be effective for enhancing the production of liquid hydrocarbons from the horizontal wells with multistage hydraulic fracturing in shale oil reservoirs. However, accurate simulation of the huff-n-puff process for optimum recovery proves challenging. Therefore, this work employs a multi-scale characterization approach to understand the complexity of the shale medium and investigate the underlying mechanisms of the hydrocarbon gas huff-n-puff process in shale oil samples.

The integrated workflow comprises of large-scale and pore-scale characterization, respectively. Large-scale characterization involves regional characterization of a shale oil formation using laboratory measured petrophysical parameters, wireline log measurements, and seismic data. While pore-scale characterization makes use of the scanning electron microscopy (SEM), energy-dispersive X-ray spectroscopy (EDS), focused ion beam-scanning electron microscopy (FIB-SEM). The integrated workflow considers seismic – wireline log correlations beyond the wellbore for large-scale characterization. On the other hand, the pore-scale characterization provides detailed heterogeneity information of the shale oil samples in addition to a 3D generated pore network model to approximate the geometric and transport properties. Raman spectroscopy and nuclear magnetic resonance (NMR) methods are employed to determine structural changes associated with the maturation of organic matter and to evaluate the hydrocarbon gas huff-n-puff recovery process, respectively. The NMR results also estimates core-scale petrophysical properties such as porosity and hydrocarbon saturation after a high pressure,

high temperature (HPHT) system is used to subject Eagle Ford shale oil samples to hydrocarbon gas huff-n-puff.

A quality index map was generated as part of the reservoir-scale characterization to identify sweet spots for well placement and optimize hydraulic fracturing for hydrocarbon recovery in the Chattanooga shale formation. Significant findings for pore-scale characterization using SEM/BSE, EDS, and FIB-SEM include the differentiation of depositional kerogen from migrated organic matter with developed nanopores and identifying the rock fabric of Eagle Ford shale oil to be dominated by carbonate with a mix of quartz, pyrite, and clay minerals. The organic pore tortuosity averaged at 2.36, 1.49, and 2.03 in the *x*, *y*, and *z*- directions, respectively, and an average permeability of ~ 0.00364 mD are among the estimated geometric properties of the shale samples. Furthermore, the equivalent pore diameter of the Eagle Ford shale samples are approximated from 13 nm – 580 nm for organic pores and 20 nm – 4 μm for inorganic pores. Furthermore, Raman thermal maturity measurement is shown to be dependent on the original maceral/source chemistry. NMR T_2 distributions exhibited reduced amplitude to indicate oil/hexadecane recovery and a shift to the left is interpreted as remaining heavier fractions. The estimated oil/hexadecane recovery was comparable to that of mass balance estimations.

This integrated workflow to shale oil reservoirs is capable of optimizing hydrocarbon recovery in shale oil reservoirs at the large-scale through sweet-spot identification as well as understanding the heterogeneity of the shale medium at the pore-scale and estimating the fluid flow properties for simulation.

Acknowledgments

Several people have contributed to the progress and achievement of this work in their own way and without their help, this work would not be possible. First is my advisor, Dr. Reza Barati, for his supervision, and substantial knowledge during the course of my study. I am forever indebted to him for the opportunity to learn and grow under his guidance.

I would like to thank my committee members, Dr. John Doveton, Dr. Shapour Vossoughi, Dr. Russ Ostermann, Dr. Anil Misra, and Dr. Jyun-Syung Tsau for their time and constructive criticisms and insightful comments and recommendations.

My gratitude also extends to Dr. Robert Goldstein from KICC, Geology department for his immense contributions and insights in the petrographic interpretations on sections of this work. Special thanks also go to Dr. Craig Marshall for his help in interpreting the Raman results and his contributions to the Raman work.

I would like to thank the Tertiary Oil Recovery Project (TORP) for funding different parts of this work and also extend my appreciation to Dr. Tsau at the TORP lab for his immense contribution to the huff-n-puff work on the Eagle Ford samples. I would also like to thank Dr. Prem Thapa at the KU Imaging Center for helping me acquire the SEM/BSE images as well as Randy Polson for his assistance in acquiring the FIB-SEM images.

My appreciation extends to Chesapeake Energy for funding parts of the work and providing the shale samples for this study as well as the Kansas Interdisciplinary Carbonates Consortium (KICC) for providing a platform for collaboration and for partially funding parts of this project.

My deepest gratitude goes out to my family for their unconditional love and unwavering support throughout this tumultuous and smooth journey. To my friends and fellow graduate students, thank you for your friendship and support during my stay at the University of Kansas.

Table of Contents

List of Figures

List of Tables

1 CHAPTER 1: SWEET-SPOT MAPPING FOR HYDRAULIC FRACTURING

Devonian-Mississippian Chattanooga shale plays in North America are referred to as unconventional reserves with potential hydrocarbon accumulations. Unlike Chattanooga shale in the Appalachian region, less effort has been dedicated to its extension in the Ozark region. Having established the complexity of shales contributes to low primary hydrocarbon recovery, there is the need to fully understand the shale medium to aid in delineating sweet-spots for well placement and improved hydrocarbon recovery.

This chapter presents regional characterization of the Chattanooga shale formation in Sumner County, KS, by making use of laboratory measured petrophysical parameters, wireline log measurements, and seismic data as part of the integrated workflow for shale oil reservoirs.

1.1 Introduction

Chattanooga shale in southern Kansas has always been thought of as the source rock for most conventional hydrocarbon reservoirs in the Wellington field until the recent recovery of shale plays as a resource. It is characterized as a shale oil resource with an average thickness of ~43ft. Chattanooga shale is the name given to black shale sequences deposited in the Late Devonian era in North America [1].

Shale oil reservoirs are susceptible to lower recovery efficiency due to the viscous nature of oil and possible two-phase flow conditions below the bubble point pressure, which occur in an ultra-tight matrix with heterogeneous pore space. To probe such a complex medium proves challenging, hence, the need to couple different datasets (laboratory measurement, well logs, and seismic) for a better understanding.

Regional characterization starts with the interpretation of the seismic data from which a layer property (acoustic impedance) is developed. This is followed by computing petrophysical

properties (porosity, TOC, water saturation) from well logs to be subsequently correlated to laboratory core measurements and seismic attributes. The well log – acoustic impedance correlations goes beyond wellbore characterization. The mineral composition of the Chattanooga shale from the well logs is generated through a volumetric probabilistic model [2]. Geomechanical properties such as the fracability index (FI) and mineral-based brittleness index (MBI) are estimated to indicate the prospect of the shale oil resource for hydraulic fracturing. Finally, a quality index map was developed based on the different estimated properties for the Chattanooga shale to identify sweet-spots for effective well placement and improved oil recovery.

1.1.1 Study Area

Figure 1.1 (top image) shows a statewide view of the Wellington field (enclosed in red box) regarded as an active oil field with Kansas City and Mississippian limestone identified as the main producing formations. The Chattanooga shale lies between the Mississippian limestone and Simpson sandstone and perceived as a possible shale source rock for the producing formations. Figure 1.1 (bottom image) shows a zoomed-out section of the study area with the location of five (5) vertical wells namely, Wellington unit -128, Meridith-3, Meridith-4, Cole-1, and Peasel-1 used for this study. The shale play extends to Oklahoma as Woodford shale. However, this study focuses on the shale play in Southeastern Kansas with occasional references to the Woodford shale.

The Upper Devonian-Mississippian formation is divided into the lower, middle and upper shale members due to differences in uranium in addition to the basal Misener sandstone; the middle shale member is considered the most radioactive with a gamma ray (GR) reading of 254 API. Figure 1.2 shows the GR log in track 1 of the well sections passing through the Chattanooga shale interval. Lambert [1] believed the middle unit was deposited during the period of maximum

transgression which could explain its identification with the Chautauqua arch (Pre-Mississippian anticlinal extention), limiting its thickness to about 50 ft.

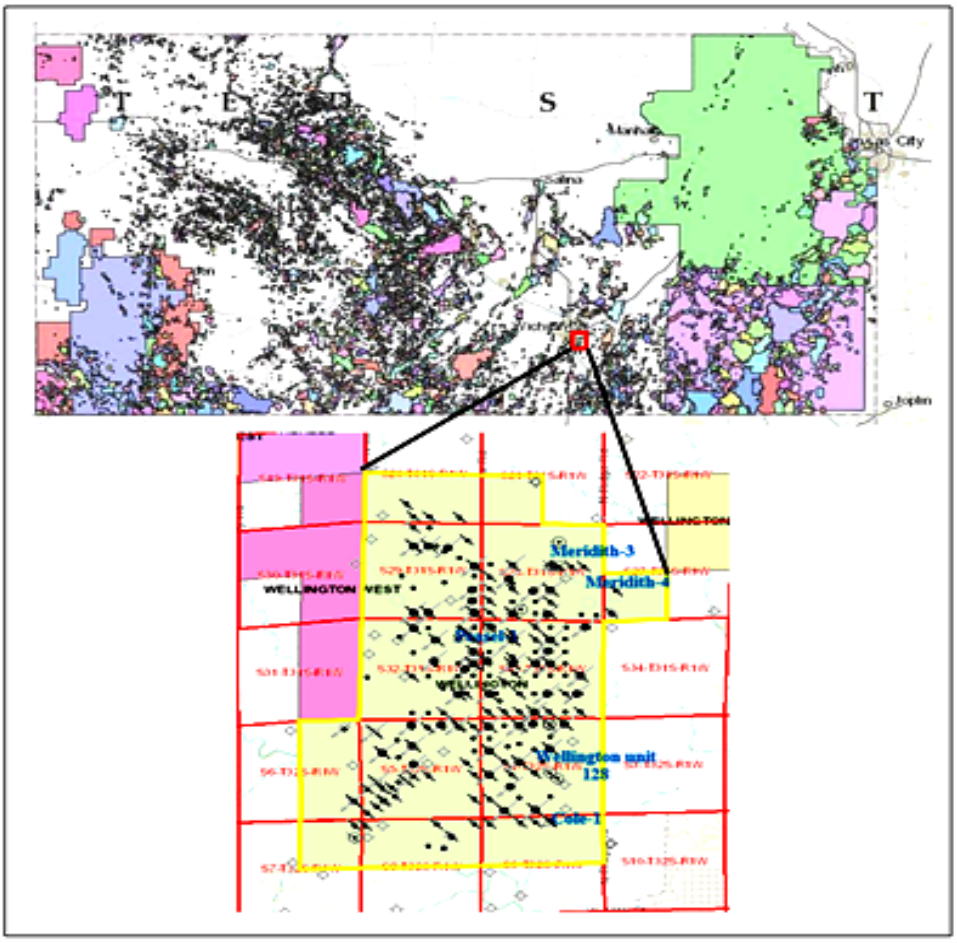

Figure 1.1: Statewide view of Wellington field, Sumner County, Kansas, enclosed in red box (top); a zoomed-in section of the Wellington field with displayed wells is shown at the bottom [3]

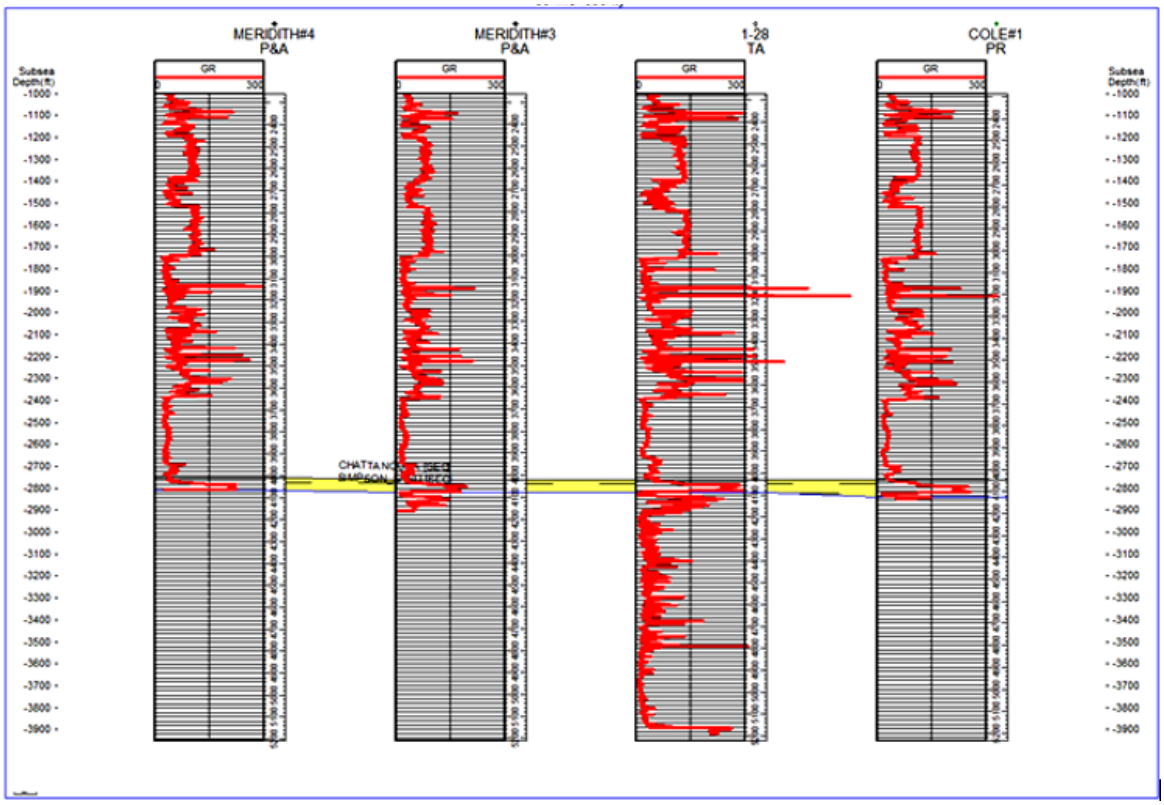

Figure 1.2: Wells passing through the Chattanooga shale interval; gamma ray (GR) log is shown in track 1 of the well section

1.2 Methods

1.2.1 Seismic Interpretation

Well logs from all five (5) wells identified above in Figure 1.2 were tied to the seismic data obtained for the entire Wellington field by generating a forward modeling synthetic seismogram for accurate correlations. The bulk density (RHOB) and sonic travel-time (DT) logs together with a 55 Hz Ricker wavelet were used as input; the synthetic seismogram in Figure 1.3 is sandwiched between the seismic inline 23 for the Wellington unit 128 well. The top of the Chattanooga shale interval has a negative reflectivity in track 2 which corresponds with a trough of high amplitude (blue) on the seismogram while the bottom of the interval has a positive reflectivity also in track 2 corresponding to a strong peak (red) on the seismogram. A close to perfect match of the seismic

and well logs can be seen within the Chattanooga shale interval which validates the quality of our data.

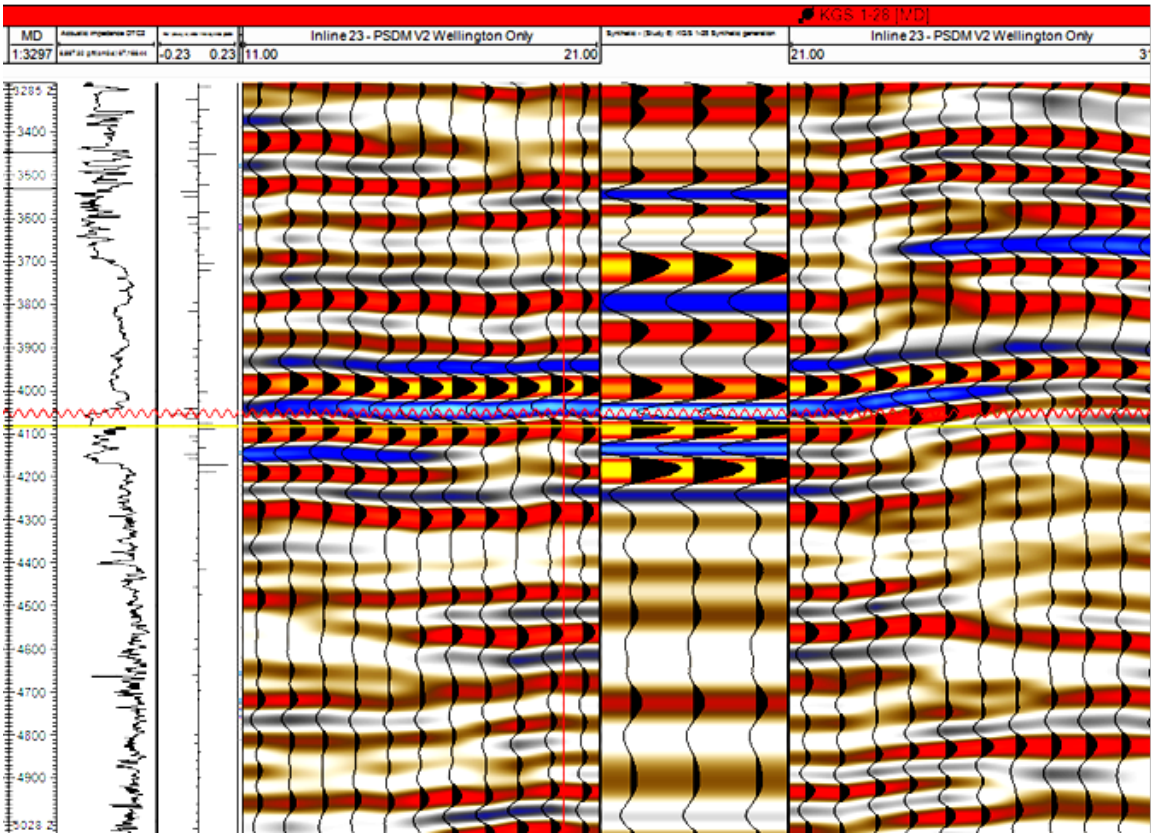

Figure 1.3: Forward modeling synthetic seismogram (middle window) for seismic- well tie

1.2.1.1 Seismic Acoustic Impedance

Information on the spatial variation of reservoir properties away from the wellbore improves reservoir characterization in regions lacking well logs. A layer property model from seismic data referred to as acoustic impedance is created for such spatial variation correlations. Acoustic impedance (*AI*) is defined as a physical (layer) property obtained from the product of seismic velocity and rock density (RHOB). It varies with the lithology, porosity and fluid content unlike seismic data which provides information only at the interfaces [4]. Therefore, by correlating

any of the reservoir properties especially porosity to the resulting inverted cube, a statistical correlation could be obtained to predict wells logs from neighboring seismic. The steps to obtain the inverted cube include:

a) Create a new acoustic impedance log (*AI*) with RHOB and DT from the well logs.

b) Genetic inversion of the *AI* log is created together with the seismic data.

c) An acoustic impedance cube is thus generated.

It is worth point out that, seismic inversion for acoustic impedance estimation is highly dependent on accurate estimation of the forward seismic model and relies on the availability of good quality data. Uncertainty in source wavelet estimation, noise in the seismic and log data, as well as a limited number of well data can affect impedance predictions and subsequent estimation of porosity. While relative porosity trends (high vs. low) presented in this work are believed to be representative of the Chattanooga formation spatial variability, the accuracy of quantitative predictions degrades rapidly away from well control.

1.2.1.1.1 Porosity Cube

Shale and kerogen corrections were applied to both the neutron porosity (NPHI) and density porosity (DPHI) according to steps developed by Crain [5]. The density porosity (DPHI) correction is expressed as

$$DPHI_c = DPHI - (V_{sh} \times DPHI_{sh}) - (V_{ker} \times DPHI_{ker}) \quad (1\text{-}1)$$

where, V_{sh} = the volume of shale, calculated from the total gamma ray (GR) curve

$DPHI_{ker}$ = the density porosity of kerogen, defaulted to 0.65

$DPHI_c$ = the corrected density porosity

$DPHI_{sh}$ = density porosity reading within the shale interval

V_{ker} = volume of kerogen

The effective porosity (of the Chattanooga shale interval was then calculated for all five (5) wells as an average value of the corrected DPHI and NPHI logs. Subsequently, a cross-plot was generated between the acoustic impedance (AI) log and effective porosity (φ_{eff}) resulting in an inverse relation with a correlation coefficient (R^2) of 99%. The statistical correlation is expressed as

$$\varphi_{eff} = 0.2 - 4.5 \times 10^{-6} AI \quad (1\text{-}2)$$

Artificial Neural Networks (ANN) are known to acquire knowledge from their surroundings by means of training and storing the acquired knowledge through the use of synaptic weights [6]. Porosity from the well logs were trained with the ANNs before correlating with seismic data by allocating 40% of the data for testing and 60% for training.

1.2.2 Petrophysical Properties

1.2.2.1 Water Saturation

Water saturation is an important petrophysical property required for accurate estimation of hydrocarbon volume in oil and gas reservoirs. A shale formation is electrically conductive due to the embedded ions in its layers as result the Archie's equation [7] for computing water saturation become unreliable since it solely depends on the effect of brine. Both Simandoux and Dual Water models incorporate the volume of shale and cation exchange capacity of shale, respectively, in estimating the water saturation. Notably, the dual water model (DWM) as the name implies, predicts the presence of the clay bound water (S_{wb}) in addition to the mobile formation water. Comparing both methods, this study relied on the Simandoux model, which works better in low porosity formations like the Chattanooga shale interval [5].

Similarly, the water saturation model was trained by ANN using density (DPHI), neutron (NPHI), and resistivity (RT) logs as input [8].

1.2.2.1.1 Simandoux Model

This model accounts for the volume of shale which contributes to the conductivity of the formation in addition to that of the formation water. The expression below Eq.(1-3) for the Simandoux model is based on the assumption that the conductivity of a mass of conductive particles saturated with conducting fluid can be represented by a group of parallel resistors [9].

$$\left(\frac{\varphi^m}{aR_w}\right)S_w^2 + \left(\frac{V_{sh}}{R_{sh}}\right)S_w - \frac{1}{R_T} = 0 \qquad (1\text{-}3)$$

where, R_w and R_{sh} are the resistivity of water and shale, respectively, specific to a given formation, and R_T is the formation resistivity.

1.2.2.2 Total Organic Carbon (TOC)

The log-derived bulk-density [10] and *Δlog R* method [11] are commonly used for estimating the TOC in shale formations. However, this study developed a correlation between the gamma ray (GR) log from Spriggs #1-34 and the Leco TOC laboratory measurement. Spriggs # 1-34 is one of the two wells passing through the Chattanooga shale interval in Barber County, KS. Rock-Eval pyrolysis and Leco TOC measurements were performed on sixteen (16) core plugs at different depths (4453 ft. - 4939 ft.) from the Spriggs well. Leco TOC carbon analyzer measures the carbon dioxide produced as a result of organic carbon combustion. The gamma ray (GR) – TOC correlation was developed by plotting the Leco TOC measurements at given depths to the corresponding gamma ray (GR) readings. The GR-TOC correlation Eq.(1-4) from the Barber

County was applied to the Chattanooga shale in Sumner County, and was comparable to log-derived bulk-density estimation of TOC.

$$TOC = 0.022 \times GR - 3.037 \quad (1\text{-}4)$$

1.2.3 Geochemical Composition

In the absence of a geochemical log for the Chattanooga shale interval under study, a volumetric probabilistic method was used to estimate the mineral composition of the shale interval by employing conventional logs such as gamma ray (GR), bulk density (RHOB), neutron porosity log (NPHI), uranium and photoelectric logs (PeF). The model adjusts typical mineral compositions initially specified from geochemical logs and in this particular case, mineralogical values of the Chattanooga shale in Barber County, Kansas, was used. The model outputs volumes of clay, quartz-feldspar-mica (QFM), pyrite, kerogen, and effective porosity (PHI_{eff}).

A similar volumetric model by Spears and Jackson [2] calculates carbonate in addition to the outputs of our model and it includes the resistivity (RT) and sonic travel-time (DT) logs as inputs. Table 1-1 below shows a typical Chattanooga Shale mineralogical composition from the Barber County, KS provided by the Kansas Geological Survey (KGS).

Table 1-1: A typical log readings for various minerals of Chattanooga shale, Barber County (provided by Dr. Doveton – KGS)

Well logs	Clay	QFM	Pyrite	Kerogen	PHI_{eff}
GR	220	33	33	1752	32
RHOB	2.7	2.65	5	1.2	1
PeF	11.2	4.77	82.2	0.312	0.5
NPHI	45	-2.1	-2.0	60	100
Unity	1	1	1	1	1

1.2.4 Geomechanical Analysis

Unconventional shale plays rely heavily on fracture networks for improved permeability and bulk transport due to the ultra-tight nature of the matrix. Geomechanical analysis offers a means to evaluate the prospect of a shale interval for effective hydraulic fracturing.

1.2.4.1 Mineral-Based Brittleness Index (MBI)

The mineral-based brittleness index (MBI) is a generalized completion quality indicator for hydraulic fracturing. Rickman et *al*. [12] describes a more brittle formation as one with higer silica content than clay and perceived to easily create fractures but its ability to keep the fractures open is another concern . The MBI is defined in different forms by different authors including the expression below by Wang [13]

$$MBI = \frac{(W_{QFM}+W_{CAR})}{(W_{CAR}+W_{QFM}+W_{CL}+TOC)} \tag{1-5}$$

where, W_{QFM} is the dry weight percentage (%) of QFM, W_{CAR} is the dry weight % of carbonate, W_{CL} is the dry weight % of clay, and TOC is the weight % of the total organic carbon.

1.2.4.2 Fracability Index (FI)

Fracability index (FI) modifies the term “brittleness” by incorporating a fracture toughness term which quantifies the amount of energy required to create a new fracture surface. Thus, a potential formation for hydraulic fracturing is not only dependent on the brittleness but also the energy required to create a new fracture surface is considered [14]. The fracability index is expressed as

$$FI = \frac{B_n+K_{ICn}}{2} \tag{1-6}$$

where, K_{IC} is the fracture toughness and B is the fracture brittleness. The fracture toughness is related to the Young's modulus (E), while the brittleness is expressed in terms of the Young's modulus (E) and the Poisson's ratio (v). Both parameters are given as

$$K_{IC} = 0.313 + 0.027 \times E \tag{1-7}$$

$$B = \frac{E+v}{2} \tag{1-8}$$

1.2.5 Quality Index (QI)

From the comprehensive petrophysical, geochemical, and geomechanical properties of the Chattanooga shale, a quality index (QI) reservoir property was developed to be used for easy and accurate identification of sweet-spots for fracturing. This quality map was computed for both matrix and natural fractures and is expressed as

$$QI_{matrix} = k \times S_o \times h \times \varphi \times TOC \times FI \tag{1-9}$$

$$QI_{fracture} = \vec{k} \times S_o \times h \times \varphi_f \times TOC \times FI \times \vec{\sigma} \tag{1-10}$$

where, k is the permeability of the shale interval (mD); φ, φ_f is the porosity of the matrix and fracture, respectively; h is the thickness, ft.; $\vec{\sigma}$ is the fracture shape factor and $\vec{k}$ is the fracture permeability in all three dimensions (i, j, k).

A matrix permeability (k) of 0.001 mD is obtained from the NMR log in Wellington unit-128 well, which passes through the Chattanooga shale interval. Whereas, the fracture permeability was obtained through fracture modeling from image logs within Wellington field; the estimated fracture permeability ranged from 3 - 6 mD.

1.3 Results and Discussion

1.3.1 Seismic – Well Log Correlation

Figure 1.4 shows an $AI - \varphi_{eff}$ map, where the middle shale member (MSM) of the Chattanooga shale interval has a higher value of 7***%***. The estimated porosity of the lower shale member (LSM) is in close range at ***6%***, while the upper shale member (USM) is the least porous. The input logs for training the ANN include the density porosity log (DPHI), the neutron porosity log (NPHI), the corrected density and neutron porosity logs, and the acoustic impedance log (AI).

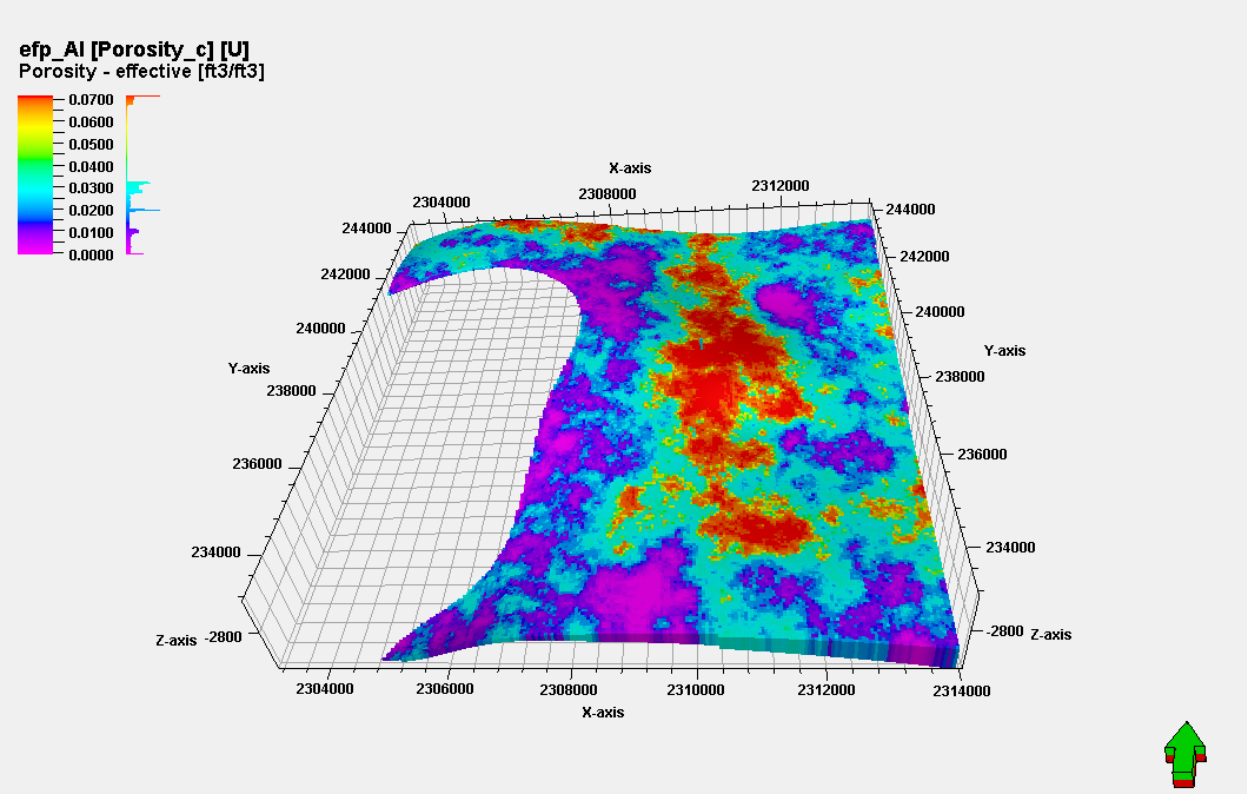

Figure 1.4: Acoustic impedance – effective porosity map for the middle member of the Chattanooga shale interval

1.3.2 Petrophysical Properties

1.3.2.1 Simandoux Water Saturation Model

From the Simandoux model in Eq. (1-3), the average water saturation is estimated at ~24%. Figure 1.5 below presents an oil saturation (*So*) distribution map in the most representative layer at a maximum of ~ 76%. This petrophysical property plays a major role in calculating the initial hydrocarbons-in-place. A challenge with this calculation lies in determining the cementation factor as well as the saturation index for unconventional shale resources and the resistivity of shale.

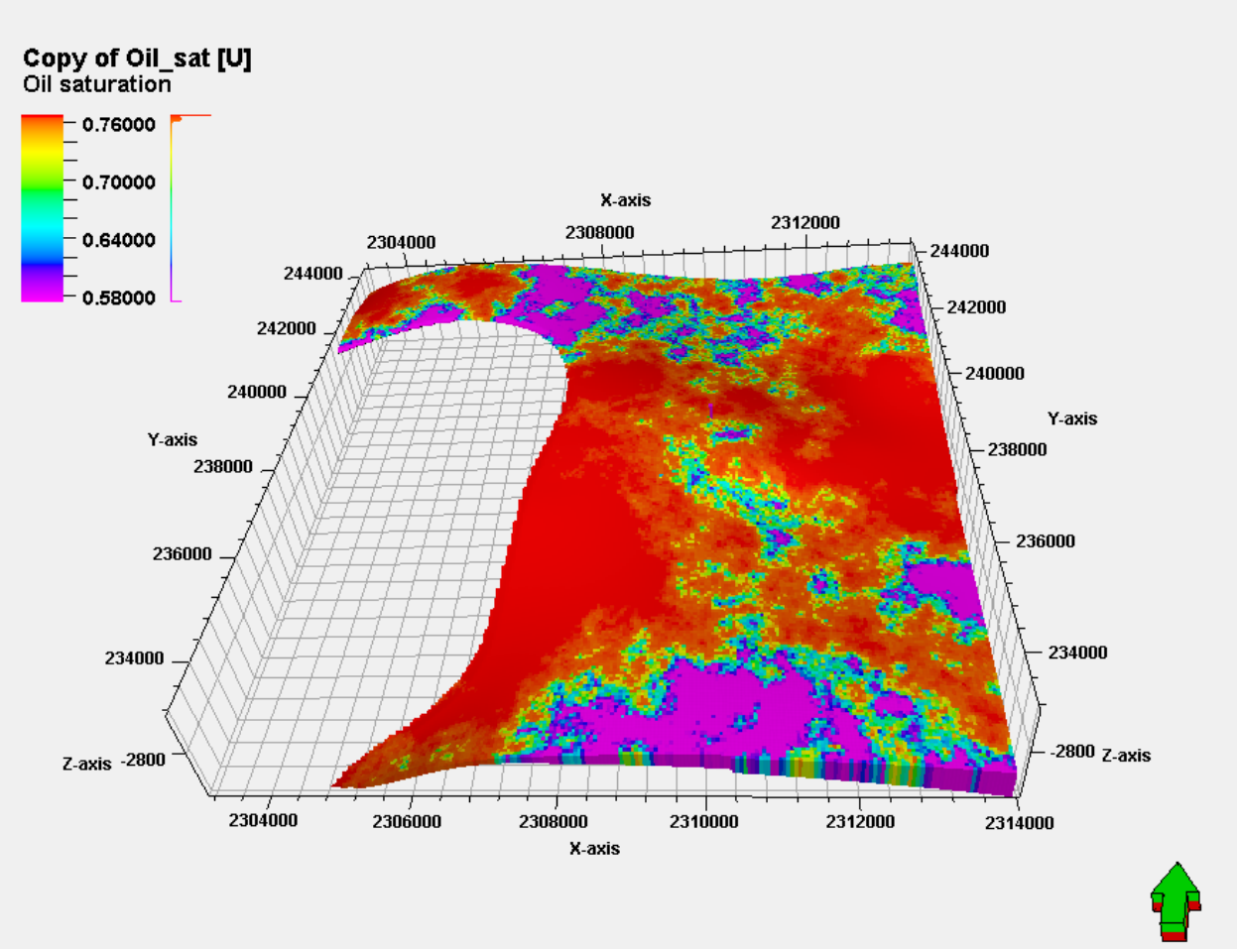

Figure 1.5: Oil saturation map of the middle member of the Chattanooga shale, Sumner County, KS

1.3.2.2 Gamma Ray (GR) – Total Organic Carbon (TOC) Correlation

The average TOC from the GR-TOC correlation in Eq. (1-4) for the middle shale member is ~2.53 *wt. %* compared to the bulk density – gamma ray (RHOB-GR) correlation [10] of ~2.26 *wt. %*. TOC is one of the main determining factors in characterizing a shale formation to be productive and a TOC > 1 *wt. %* is considered productive.

1.3.3 Hydrocarbon-in-Place

The estimated oil originally-in-place (*OOIP*) for a section of the reservoir at ~ 640 acres is 4 MM bbl. and the estimated free gas-in-place (*GIP*), for the same section of the reservoir is 32 MM scf.

1.3.4 Geochemical Composition

The mineral composition of the Chattanooga shale from the volumetric model is listed in Table 1-2. The clay and silica content are in a close range, and so the Chattanooga shale could have both brittle and ductile characteristics.

Table 1-2: Mineral composition of Chattanooga shale, Sumner County, KS

Mineral	Average Composition (wt. %)
QFM	43
Clay	45
Carbonate	3.5
Pyrite	2.2
Kerogen	2.6

1.3.5 Geomechanical Analysis

A mineral-based brittleness index (MBI) is calculated from the mineral composition (Table 1-2) and a value of 0.45 was obtained. According to Rickman [12], a MBI > 0.4 gives an indication of a prospective rock for hydraulic fracturing, to which the Chattanooga shale is a candidate. Moreover, a fracability index (FI) of 0.53 was obtained from the correlation by Jin [14]. The fracability index (FI) ranges from 0 to 1 with the latter being the most fracable; the Chattanooga shale formation shows more than 50 % potential for effective hydraulic fracturing.

1.3.5.1 Fracture Modeling

As part of modeling the natural fractures within the Chattanooga shale formation, a fracture analysis data from the shale interval produced a fracture intensity of ~45 area/volume (A/V) dipping at approximately 75° in the NE-SW direction. These fracture parameters in addition to the shape factors were used in computing the quality index (QI).

1.3.6 Quality Index (QI)

Figure 1.6 shows a generated quality index map based on the petrophysical and geomechanical properties estimated for the Chattanooga shale. The map is to aid in identifying area suitable for an effective fracturing. The quality index map ranges from 0 to 1 with the latter being the most productive; the Chattanooga shale shows a high potential of ~ 80%.

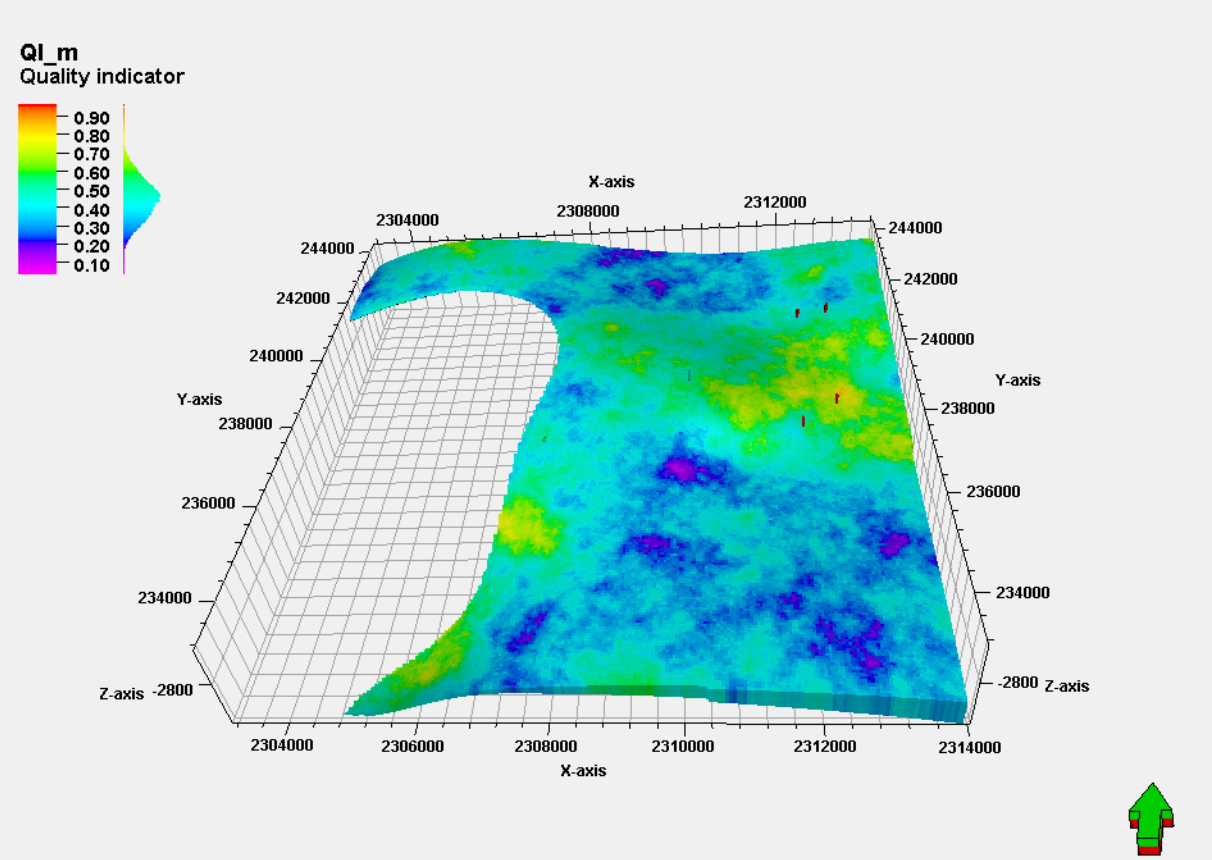

Figure 1.6: Quality index (QI) map for sweet-spot identification

1.4 Conclusions

- From the regional characterization of the Chattanooga shale, a better understanding of the formation is achieved for future development.
- Accurate petrophysical correlations were developed through multiple datasets and are applicable to resource shale plays in Southern and Central Kansas and possibly beyond.
- A quality index map is created from the properties obtained from the regional characterization process, which give a good indication of regions to create fractures for optimum hydrocarbon recovery.

Publication:

S. Cudjoe, M. Vinassa, H. B. Gomes and R. Barati, "A comprehensive approach to sweet-spot mapping for hydraulic fracturing and CO2 huff-n-puff injection in Chattanooga shale formation," *Journal of Natural Gas Science and Engineering,* vol. 33, pp. 1201-1218, 2016.

2 CHAPTER 2: PORE-SCALE CHARACTERIZATION AND HYDROCARBON GAS HUFF-N-PUFF

Huff-n-puff gas injection has proven to be ideal for recovering more liquid hydrocarbons from hydraulically fractured and horizontally drilled wells in ultra-tight unconventional shales. The complexity of shales, however, inherent in the variation of mineral microstructure and heterogeneous pore space, makes accurate simulation of the huff-n-puff process for optimum recovery challenging. Therefore, this chapter deals with the visualization and quantification of the microstructure of Lower Eagle Ford (LEF) shale samples before and after hydrocarbon gas huff-n-puff recovery. This is used to produce accurate estimations of petrophysical (porosity, permeability) and intrinsic rock (tortuosity) properties. The petrophysical and intrinsic rock estimations provide accurate measures for reservoir simulation for the huff-n-puff process.

Methods used for pore-scale characterization include, scanning/backscattered electron microscopy (SEM/BSE), energy-dispersive X-ray spectroscopy (EDS) and focused ion beam-scanning electron microscopy (FIB-SEM).

2.1 Introduction

Shale oil reservoirs are thought to be made up of the mineral matrix with isolated patches of organic matter, and are expected to possess very low matrix permeability. Primary micro-scale pores and micro-fractures, in addition to the nano-pores in organic matter are occupied by free, dissolved and/ or adsorbed liquid hydrocarbons, recoverable through horizontal wells and hydraulic fracturing. Oil from shale and/ or tight reservoirs contributes to about 68% of the total domestic crude oil production in the United States (U.S.) and continue to increase despite the low oil prices [15]. An effective shale oil resource is characterized by total organic carbon (TOC) (1.0

– 20 *wt. %*), the thickness of the organic-rich interval (> 10 ft.), kerogen type (type I & II) and thermal maturity (0.5% - 1.3% R_o), porosity (< 10%), permeability (< 0.1 mD) and its fracturing potential [16, 17].

The Eagle Ford Shale (EFS) play is an Upper Cretaceous formation located in south Texas, which extends about 400 miles from the Texas-Mexico border to the East Texas Basin here in the U.S. [18]; it is bounded on top by the Austin Chalk and overlies the Buda Limestone. It is regarded as a productive shale resource with TOC in the range of 2 – 12 wt. %, porosity of 8 – 12%, productive depths ranging from 2,500 – 14,000 ft., and thickness varying from 120 – 350 ft. Prior to its discovery as a productive shale resource in 2008 by Petrohawk, it was considered to be the source rock for the Austin Chalk [19, 20]. It is high in calcite content compared to clay minerals, contributing to its brittleness, rendering it suitable for hydraulic fracturing, but also rendering it prone to diagenetic alteration [21, 22]. Hydrocarbons produced from the Eagle Ford include, dry gas, gas condensate, volatile and black oil. The total recoverable oil reserves and resources of the EFS are estimated at 3.35 billion barrels of oil (BBO), whereas, the total gas reserves and resources are estimated at 21 trillion cubic feet (TCF) [23]. The EFS is divided into two main units, namely, the upper EFS (light & dark gray calcareous mudrock) and the lower EFS (dark-gray mudstone) based on the abundance of uranium [24]; the lower EFS within the oil-window (0.98% - 1.03% R_o) is the subject of this study.

Recoverable oil production in shale oil formations is controlled by the rock (e.g., permeability) and the fluid properties (e.g., viscosity of the oil) as well as the natural reservoir drive energy, which tends to deplete rapidly. Thus, primary recovery in shale oil reservoirs with horizontal wells and multi-stage hydraulic fracturing for fluid flow is very low (5 – 10% of the original oil in place (OOIP)) [25]. Therefore, implementing improved/enhanced oil recovery

techniques such as gas injection serves as a solution to maximize oil recovery. During gas injection, the fracture complexity (stimulated reservoir volume) provides a conductive pathway for injected gas to contact the matrix and the injected gas supplements the depleted reservoir energy. Continuous gas flooding is not ideal for organic-rich shales due to isolated, porous, oil saturated organic patches and low permeability of the matrix where pores are not effectively communicating with the fracture network. As a result, the injected fluid may circulate without a significant contact with the reservoir oil resulting in a premature breakthrough to the production wells. On the other hand, the huff-n-puff process uses a single well as both the injector and producer. It consists of three main stages; the huff time (injection stage), the soaking time, and the puff time (production stage); the soaking time allows the injected gas to diffuse through the conductive fracture and micro-fracture pathways into the matrix and isolated organic pores to interact with oil. The gas-oil interactions lead to reduced oil viscosity, increased oil volume due to swelling and reduced interfacial tension (IFT). Injected gases include carbon dioxide (CO_2) and produced hydrocarbon gas but hydrocarbon gas is significantly cheaper and more readily available [26] . Orozco [27] pointed out the need to contain the huff-n-puff process both laterally and vertically for success of operation. The EFS is known to possess vertical and lateral containment with inverse distribution of fluids, where the natural gas is at the bottom of the structure, condensate is in the middle and oil is at the top, contrary to the fluid distribution of conventional reservoirs [28]. Moreover, Sheng [29] recommended a set of parameters to optimize the huff-n-puff process through numerical simulation such as increasing the injection pressure to be above or equal to the initial reservoir pressure. The optimum huff time is attained when the pressure near the wellbore reaches the maximum injection pressure, while the optimum puff time is achieved when the pressure near the wellbore reaches to the minimum production pressure. Recovery factors

in the range between 20% - 80% have been reported in literature for gas huff-n-puff recovery in shale oil reservoirs, when contained within the stimulated reservoir volume (SRV) [30]. However, the interaction of organic matter, being it migrated (bitumen/solid bitumen) or depositional, with hydrocarbon gas at the pore-scale is not extensively studied as part of the huff-n-puff process.

The limitation of wireline logs to accurately capture the complexity and heterogeneity of shale microstructure and pore systems has given rise to pore-scale characterization, which involves the use of imaging techniques such as scanning electron microscopy (SEM) and focused ion beam-scanning electron (FIB-SEM), among others, to visualize and quantify rock properties through image analysis at the micrometer or nanometer scale. While, the SEM produces 2D surface images of shale samples of a larger field of view, the FIB-SEM produces 3D pore-scale images of a smaller field of view; the reconstructed 3D volume is then used as a medium for fluid flow simulations. Loucks [31] studied the morphology and distribution of organic nano-pores in the Barnett shale using the SEM and reported isolated intra-particle organic pores in the range of 5 nm - 750 nm with internal porosities up to ~20%. Organic nanopores with diameters less than 100 nm are estimated to constitute about 4.5% of the total pore volume [32]. Shabro et *al*. [33] estimated electrical resistivity and permeability of the lower Eagle Ford shale based on extracted streamlines from FIB-SEM images. While, Ko et *al*. [34] investigated the pore-scale variations in rock mineralogy and the distribution of pore types using SEM in the upper Eagle Ford Shale. Numerous other works have been reported, all focused on micro-/nano-scale imaging of organic-rich shales and estimating the bulk transport properties through image analysis [35, 36, 37, 38, 39]. Most of these studies do not address the representative elementary volume or area of the pores (REV or REA). The REV/REA refers to the smallest volume/area from which a petrophysical property can be measured to yield a representative value of the pores in the sample. Kelly [40] reported FIB-

SEM representative elementary volume (REV) to be ≥ 5000 μm³ by comparing FIB-SEM petrophysical properties with those of core-scale measurements of the same sample and that of neighboring samples. At such large coarse scale (≥ 5000 μm³), only macro- and some micro-pores, mainly micro-fractures, are considered, neglecting the nanopores, which makes the results questionable. Furthermore, the current body of literature is missing a comprehensive study utilizing advanced imaging and analysis to investigate organic vs. inorganic tortuosity and its relation to the success of huff-n-puff injections in organic-rich, ultra-tight shale oil reservoirs.

Therefore, the main objectives of this chapter are to: 1) characterize the microstructure of minerals and pores in Lower Eagle Ford (LEF) Shale samples from different lithofacies using different imaging techniques; 2) study the effect of hydrocarbon gas on both depositional kerogen and migrated petroleum; and 3) generate representative pore network models of the different lithofacies and estimate the petrophysical properties that are crucial for the design of gas huff-n-puff projects.

2.1.1 Lower Eagle Ford (LEF) Shale

The lower Eagle Ford (LEF) shale of interest is composed predominantly of dark organic-rich shale from a transgressive marine interval, light-gray calcareous mudrock, marl, and limestone. It is regarded as more oil-prone and characterized by high gamma ray values ranging from 90 – 135 API [18]. Depositional facies identified in the LEF shale based on texture, structure, calcareous material, and fossils include, massive foraminiferal lime wackestone, laminated foraminiferal peloidal packstone, laminated fossiliferous wackestone/packstone, and laminated foraminiferal mudrock [21, 41].

Diagenesis in the Lower Eagle Ford (LEF) shale includes authigenic minerals (calcite, pyrite, quartz, and kaolinite) that are thought to pre-date migrated organic matter (bitumen, solid bitumen, and/ or pyrobitumen) [42]. Fishman [43] listed the paragenetic sequence within the foraminiferal mudstone to begin with pyrite, followed by calcite, then quartz, kaolinite, bitumen, fractures and finally, organic porosity.

Three (3) samples labelled A, B, and C, are from slightly different depths with varying lithofacies, total organic carbon (TOC) and slight variation of thermal maturity (close to 1%Ro) in the range of the black oil window. Table 2-1 presents rock properties determined through tight rock analysis (TRA). The laboratory measurements show Sample C, at the greatest depth, to be the most permeable (0.00198 mD) yet with the least porosity (6.5 % BV); Sample B has the highest porosity (7.2% of BV) and is the least permeable. Table 2-2 lists the Leco TOC and Rock-Eval pyrolysis measurements, where Sample A has the highest TOC content (5.75 wt. %). Going by the guidelines set by Peters & Casa [44] to determine the quality of the source rock and the kerogen type, all three samples would be considered as excellent source rocks (TOC > 4, S1 > 4, and S2 > 10) with either kerogen type I (oil prone) or type II/III (mixed oil and gas). The hydrogen index (HI) of all three (3) samples range from 200 – 300 mg HC/g TOC, which classifies them as kerogen type II/III but their S2/S3 ratio is > 15, which falls under kerogen type I. Moreover, the hydrocarbon yield (S1) is higher in Sample A and B than Sample C, which factors into diagenetic (secondary) organic pore generation. Mineral composition of each sample in weight percent (wt. %) from the X-ray powder diffraction (XRD) analysis is listed in Table 2-3. The lithology of Sample A is observed to be rich in calcite (calcareous mudrock), while Sample B is found to be a slightly argillaceous siliceous marlstone. The content of clay minerals is observed to increase with depth; calcite composition decreases with depth.

Table 2-1: Tight Rock Analysis (TRA) of the LEF shale samples from Chesapeake Energy

LEF Samples	Depth (ft.)	Pressure-decay permeability (mD)	Porosity, % of BV	Bulk density, gm/cc	Water saturation, % of PV
A	10,492	0.001752	6.9	2.366	1.2
B	10,503	0.001332	7.2	2.384	1.2
C	10,523	0.001978	6.5	2.395	6.4

Table 2-2: Leco TOC and Rock-Eval pyrolysis data for the LEF shale samples from Chesapeake Energy

LEF Samples	TOC (*wt. %*)	Vitrinite reflectance ($\%R_o$)*	S_1 (mg HC/g)	S_2 (mg HC/g)	Hydrogen index (HI) (mg HC/ g TOC)
A	5.75	0.98	8.58	11.81	205.39
B	5.06	1.01	8.88	11.77	232.61
C	5.29	1.03	6.81	11.10	209.83

*vitrinite reflectance values are calculated from the maximum temperature (T_{max}) correlation by Jarvie [45]

Table 2-3: Bulk XRD mineral composition of the LEF shale samples from Chesapeake Energy

Mineral fraction	Sample A	Sample B	Sample C
Quartz	12.7	18.4	15.3
Plagioclase	2.9	2.0	1.9
Apatite	0.1	0.2	2.4
Pyrite	2.3	1.9	2.6
Calcite	63	54.5	49.6
Dolomite	0.6	1.7	2.9
Illite & Mica	3.0	4.2	4.6
Illite & Smectite	5.9	8.4	9.3
Chlorite	0.8	0.6	0.7
Kaolinite	2.8	2.8	5.3

2.2 Methods

Samples were imaged with both the scanning electron microscopy (SEM) and the backscattered electron (BSE) in addition to the energy-dispersive X-ray spectroscopy (EDS) and

focused ion beam-scanning electron microscopy (FIB-SEM). The SEM and BSE provide high resolution 2D images of the topography and mineral contrast, respectively, over larger areas than FIB-SEM; EDS identifies and quantifies the elemental composition of the SEM/BSE imaged areas to infer the mineralogy at the micro-scale. On the other hand, FIB-SEM, provides the 3D spatial distribution and connectivity of organic matter and pores. Therefore, these imaging techniques enable the visualization and quantification of the geometry, size, network and distribution of matrix minerals, organic matter, and pores of the LEF shale samples. The resolution of the imaging techniques (SEM/BSE, EDS, FIB-SEM) were such that the structure of the rock fabric of the samples is not lost in the process and yet detailed pore-scale information is not compromised.

2.2.1 Sample Preparation

The rectangular rock chips were cut from core plugs parallel and perpendicular to stratification. Two rock chips were obtained from each core plug, with approximate dimensions of 14mm x 12 mm x 8 mm as shown in Figure 2.1 . One set of the rock chips (3 in total) was used for SEM/BSE and EDS imaging as well as hydrocarbon gas huff-n-puff, whereas the other set (3 in total) of samples was used for FIB-SEM imaging. Samples were prepped to obtain a smooth surface by both mechanical polishing (thin section lab - KU) and non-contact argon (Ar)-ion mill polishing (NanoFab lab – Utah). Samples are attached to 25 mm diameter pin-type stubs using carbon tape.

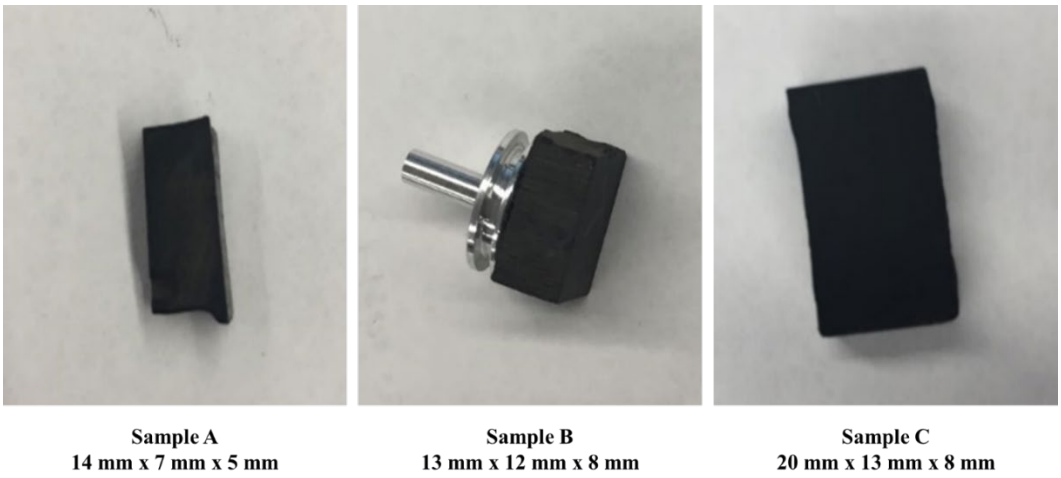

Figure 2.1: Dimensions of LEF shale rock chips used for pore-scale imaging and analysis

2.2.2 Scanning/Backscattered Electron Microscopy (SEM/BSE)

The FEI Versa 3D DualBeam (KU imaging center) was used to acquire both SEM/BSE and EDS images of all three samples with different lithofacies. A typical DualBeam dataset has a spatial resolution of 10 nm for a volume of 10 µm x 10 µm x 10 µm. The SEM/BSE images were collected at different magnifications to cover a range of resolvable mineral distributions and pore spaces. High-resolution images were taken of some organic matter (depositional/migrated) to resolve the organic pores within and estimate organic porosity. The gray scale level of the BSE images show the contrast between dark organic matter/pores (less dense), gray mineral matrix (intermediate), white/bright pyrite (dense).

2.2.3 Energy-Dispersive X-ray Spectroscopy (EDS)

The energy-dispersive X-ray spectroscopy (EDS) allows for identification of different elements within the rock samples at the micro-scale, where an X-ray spectrum is generated from the entire scan area of a selected SEM/BSE image. A proprietary EDS software associated with the DualBeam is then used to link the energy level of the X-rays with the elements and shell levels that generated them. In so doing, different types of minerals could be inferred from the elements;

some commonly accepted elements and their corresponding inferred minerals are listed below in Table 2-4.

Table 2-4: A list of inferred minerals and maceral from EDS elemental analysis

Elements	Inferred Minerals/Maceral
Carbon (C)*	Organic matter (OM)
Silicon (Si)*	Quartz (SiO_2)
Calcium (Ca)	Calcite ($CaCO_3$)
Magnesium (Mg)	Dolomite [$CaMg(CO_3)_2$]
Aluminum (Al)*	Clay minerals (kaolinite) [$Al_2Si_2O_5(OH)_4$]
Potassium (K)	Clay minerals (illite) [K,H_3O-repeating unit]
Sodium (Na)	Albite ($NaAlSi_3O_8$)
Iron (Fe), Sulphur (S)	Pyrite (FeS_2)

* These elements are found in other inferred minerals other than the dominant inferred mineral assigned to them

2.2.4 Hydrocarbon Gas Huff-n-Puff on SEM/BSE LEF Samples

The original microstructure, mineral distribution, and composition of the LEF shale samples were thoroughly studied with SEM/BSE and EDS imaging techniques before the samples were exposed to hydrocarbon gas; their positions & orientations during SEM/BSE imaging were fully documented in addition to mapping out key features of interest, presumed to be organic matter (OM) or kerogen from EDS analysis. The organic-rich LEF shale samples were then placed inside the huff-n-puff cell (SEM/BSE imaged surface up) as shown in Figure 2.2; the huff-n-puff cell is housed within a temperature controlled oven (Blue M Friction-Air HS-3802) set at 124.5°C (Figure 2.2 e). Subsequently, the hydrocarbon gas was injected at 3,500 psi to fill up the cell after the cell's temperature was reached. The valves connecting the cell were then closed and the samples were exposed to the injected hydrocarbon gas for three (3) days. After three (3) days, the

cell was depressurized to ambient pressure and room temperature and the samples were removed from the cell and re-imaged with both SEM/BSE and EDS.

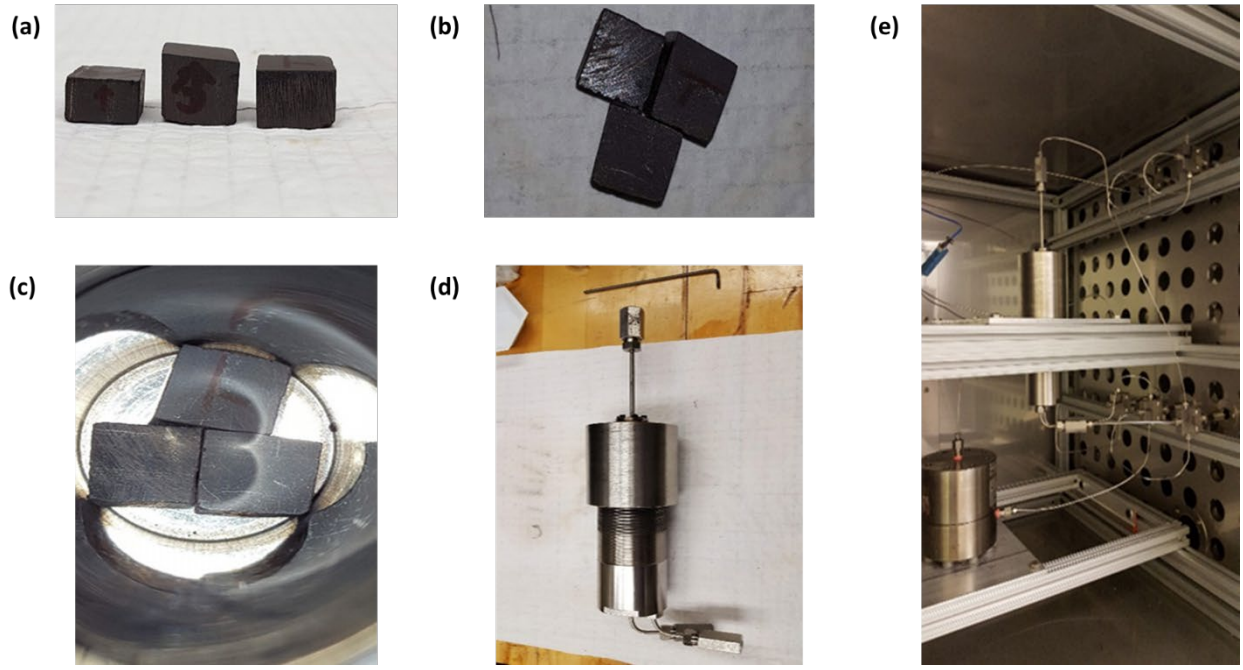

Figure 2.2: Hydrocarbon gas huff-n-puff experimental setup: (a) shows the side view of the samples with arrows to indicate which side is up, (b) shows a snapshot of the top surface of the samples exposed to gas, (c) shows the samples placed inside the huff-n-puff cell, (d) shows the huff-n-puff cell, and (e) shows the huff-n-puff cell housed inside the temperature controlled oven (Images courtesy of Dr. Tsau, TORP lab; Experiment run by Dr. Tsau, TORP lab)

Three different positions were selected for imaging on each sample. At each position, previously acquired SEM/BSE images are compared to the newly acquired SEM/BSE images after gas exposure at low magnifications using landmarks in the previous SEM/BSE images to confirm location. Subsequently, EDS analysis is carried out on the newly acquired SEM/BSE images after gas injection and the elemental compositions of the before and after are compared.

2.2.5 Focused Ion Beam-Scanning Electron Microscopy (FIB-SEM)

FIB-SEM is an imaging technique capable of resolving grains and nano-pores of organic-rich shales at ~ 5nm/ pixel by creating a series of 2D image slices on milled surfaces with thickness of ~20 nm or less. Subsequently, the series of 2D image slices are reconstructed into a 3D volume for fluid simulation and estimating rock properties under digital rock analysis. The FEI Helios NanoFab 650 at the NanoFab Lab in Utah is used to acquire the FIB-SEM images of the LEF shale samples. The acquisition process consists of a gallium (Ga) ion milling at an acceleration voltage of 30 kV and ion beam current of 0.79 nA with a working distance of 4 mm in a vacuum mode. The milling slices were then imaged at an acceleration voltage of 2kV and a beam current of 100 pA.

2.2.6 Digital Rock Analysis (DRA)

DRA involves generating pore-scale models from FIB-SEM images to carry out simulations in order to understand the effect of pore structure on flow. Pore-scale characterization enables the development of representative models for the sample; each model captures selected aspects that have the most influence on the pore-scale physical and chemical processes. DRA involves image processing eliminate artifacts, image segmentation to quantify each phase/material, pore network analysis, and simulations. This study employed the PerGeos software from Thermo Fisher Scientific for DRA.

2.2.6.1 Image Processing

The stack of 2D images from FIB-SEM imaging are mostly riddled with artifacts such as charging, bright pore edges than surrounding minerals, curtaining effect (vertical stripes), among others, which calls for image processing before pore/mineral segmentation and analysis. An

average of ~ 40 minutes is required for pre-processing the FIB-SEM stacks of each LEF sample. The pre-processing step in PerGeos involves the use of the shear module to compensate for stage tilt, cropping unwanted areas before alignment, identifying bad slices to be ignored, aligning slices to compensate for lateral shift or jittering effect during the acquisition process, and cropping once more to remove dark unwanted areas. In addition, the fast Fourier transform (FFT) filter is applied to reduce curtaining effect followed by the non-local means (NLM) filter, applied to remove noise, while preserving the pore edges. Finally, the intensity of the FIB-SEM stacks are corrected to compensate for non-uniform illumination. Figure 2.3 shows an example of both unprocessed and processed FIB-SEM image of Sample C and their corresponding gray level distributions; (a) shows the unprocessed image, where only two peaks are identified on the gray level distribution, while (b) shows the processed image with three peaks to indicate three phases on the gray level distribution. The identified three phases, otherwise, overlapped in the unprocessed image, are defined with distinct peak intensities separated into pore (0 – 50), organic matter (50 – 90), and matrix (90 – 132), respectively.

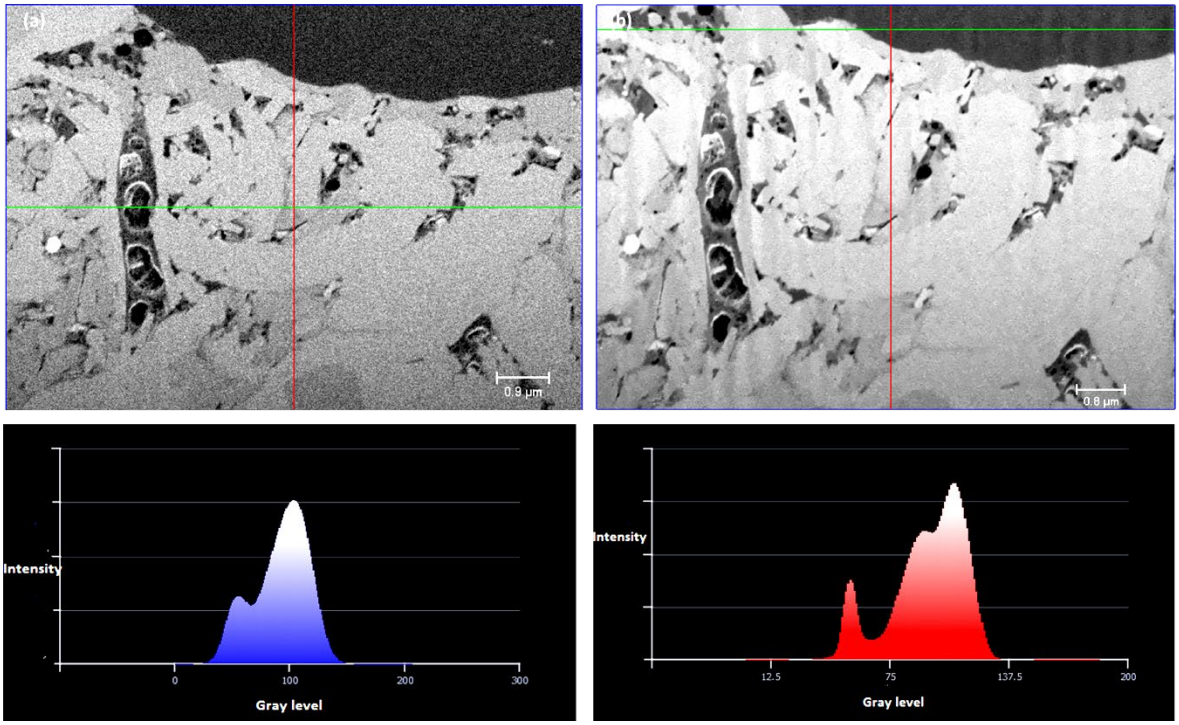

Figure 2.3: (a) FIB-SEM image of Sample C before pre-processing (top-left) and its corresponding histogram (blue-fill) showing the gray level distribution; (b) processed FIB-SEM image of Sample C (top-right) with corresponding histogram (red-fill) showing improved contrast between different phases.

2.2.6.2 Image Segmentation

The pre-processed FIB-SEM stacks are subjected to post-processing steps such as segmentation or binarization. Simple thresholding is commonly used in most image segmentation processes and it involves manually setting a threshold value for each phase within a grayscale image in order to quantify the phases. The threshold value is mostly based on the distinct peak separation obtained through pre-processing. However, in this complex three-phase or sometimes four-phase systems (presence of pyrite), simple thresholding would not be adequate for accurate labelling and reproducibility. Therefore, this study employed the used of the marker-based watershed algorithm carried out within the PerGeos software, where manual intervention is minimized. Figure 2.5 shows a marker-based watershed segmentation carried out for Sample A to quantify the organic pores. The watershed principle is based on the simulation

of the rise of water from a set of markers in a grayscale image; grayscale images are regarded as topographic reliefs with catchment basins, peaks and valleys as shown in Figure 2.4. Catchment basins are areas to be flooded with minima or maxima, while the watershed lines separate different catchment basins [46].

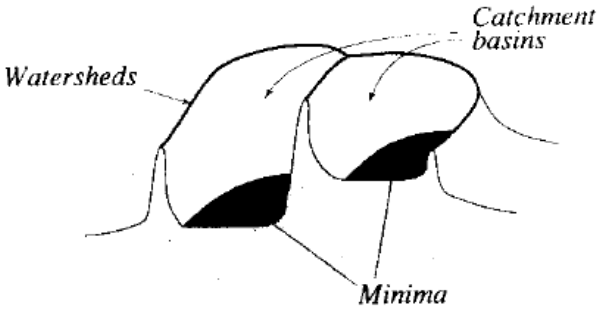

Figure 2.4: Watershed lines, minima, and catchment basins pertaining to the watershed algorithm [46]

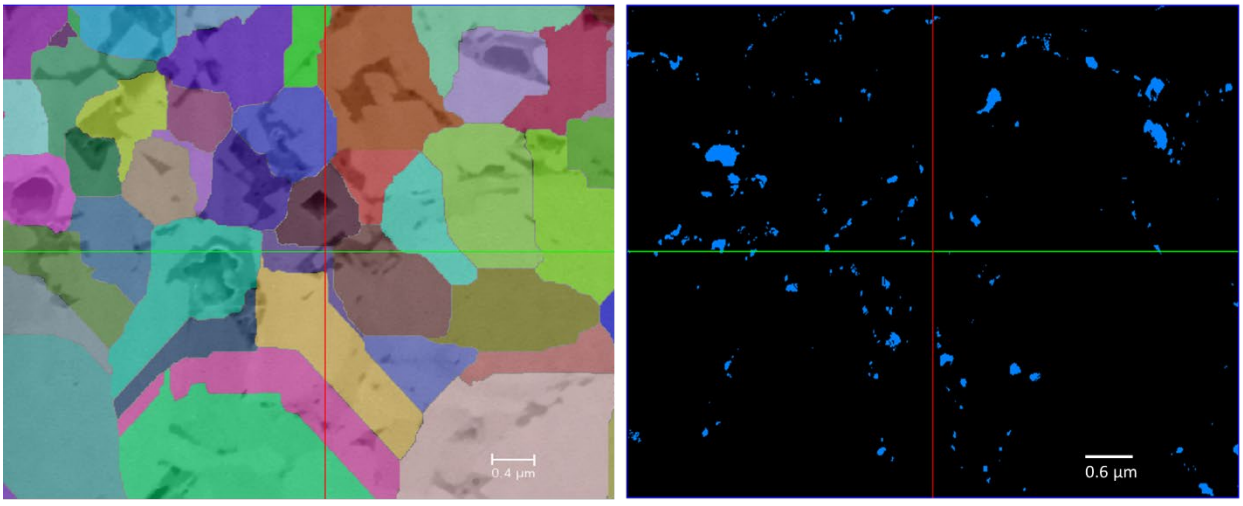

Figure 2.5: Marker-based watershed algorithm implemented on Sample A to segment the organic pores; left image shows filled up catchment basins with watershed lines and right image shows the segmented organic pores

2.2.6.3 Pore Space Analysis

Microstructural parameters such as porosity and surface area-to-volume (SAV) ratios can be quantified under pore space analysis after image segmentation. The "generate surface" tool in PerGeos is implemented for the calculation of porosity and surface area-to-volume ratios instead of voxel counting, which tends to overestimate the surface area. Thus, the surface generation tool computes a triangular approximation of the interfaces between different phases in a binary/segmented image and from the surface image porosity and other surface statistics (area, volume, polar moment of inertia, etc.) can be computed. Porosity is obtained by dividing the label volume by the total sample volume. On the other hand, pore network extraction in PerGeos is carried out using separated pore space image of each sample as input into the pore network module to output the number of nodes, number of throats, throat equivalent radius, throat channel, pore volume as well as pore equivalent radius. From the pore network model, geometric properties like tortuosity and permeability can be estimated.

2.2.6.4 Tortuosity

Tortuosity is a fundamental rock property, which characterizes the pathways of fluid diffusion and electrical conductivity. It is defined as the ratio of the actual length of the flow path to a straight line length in the direction of flow [47]. Different methods such as geometric tortuosity, hydraulic tortuosity, and centroid path tortuosity are used to calculate tortuosity through digital rock analysis in PerGeos. Geometric tortuosity relies purely on the physical microstructure and is defined as the ratio of the geodesic distance (L_G) to the Euclidean distance (L_E) between two points in the pore space. While the geodesic distance represents the shortest path possible in the presence of obstacles, the Euclidean distance defines the straight line path (distance) without any such interference [48]. The centroid path tortuosity tracks the centroid of each plane along the

vertical direction of a binary image and estimates tortuosity as the ratio of the path length through the centroids to the number of planes along the vertical direction.

The hydraulic tortuosity used in this study is based on velocities inferred from the absolute permeability computation (Darcy's law) and estimated by summing up the length of all velocities divided by the sum of the projection of the velocities along the flow direction, assuming the velocities of each throat are known. It is expressed as

$$\tau = \frac{\sum_{i=0}^{n} ||v_i||}{\sum_{i=0}^{n} ||v_{xi}||} \tag{2-1}$$

where, n is the number of throats; v_i is the velocity of fluid passing through the throat (i); and v_{xi} is the velocity along the direction of flow through throat (i).

2.2.6.5 Permeability

The permeability of the organic pore network of each sample is estimated outside of the PerGeos software using a modified form of the Kozeny-Carman (K-C) equation. The K-C equation estimates the effective permeability through a combination of hydraulic and diffusive flow phenomena by incorporating pore structure parameters such as the shape factor of the pore, tortuosity, and hydraulic radius. A modified form of the K-C equation for a FIB-SEM volume is expressed as

$$K_{total} = \sum_{i=1}^{N} \frac{\varphi^3}{\beta_i \tau^2 S^2} \tag{2-2}$$

where, φ is the porosity of the generated pore network volume; β is the shape factor that accounts for different pore shapes; τ is the tortuosity, and S is the specific surface area around the pores defined by Matyka [49].

2.3 Results and Discussion

2.3.1 Grain and Pore Types Inferred from SEM/BSE and EDS Imaging

Common grain types found in the lower Eagle Ford shale from SEM/BSE imaging include detrital quartz, clay minerals, foraminifera undifferentiated fossils, coccoliths, and depositional kerogen. Diagenetic phases include calcite cement, pyrite, clay minerals (kaolinite), quartz, and albite, and migrated OM (bitumen/solid bitumen). The organic pores within both migrated and depositional kerogen occur as either large bubble pores or small spongy pores and range from 14 nm to 500 nm in diameter, which can be classified as mesopores (> 2nm and < 50 nm) and macropores (> 50 nm) according to the International Union of Pure and Applied Chemistry (IUPAC).

2.3.1.1 BSE Images of the LEF Shale Samples

BSE images of Sample A at different magnifications are shown below (Figure 2.6) with distributions of organic matter, resolved organic pores and matrix minerals. A dark feature of interest from Figure 2.6(a) enclosed in a red box is further characterized at higher magnifications (Figure 2.6 b, c), where the organic pore sizes can be viewed and quantified. The organic pores in this particle are estimated at a volume fraction of ~ 11 vol. % through simple thresholding with equivalent pore diameter ranging from 17 nm to 4 μm.

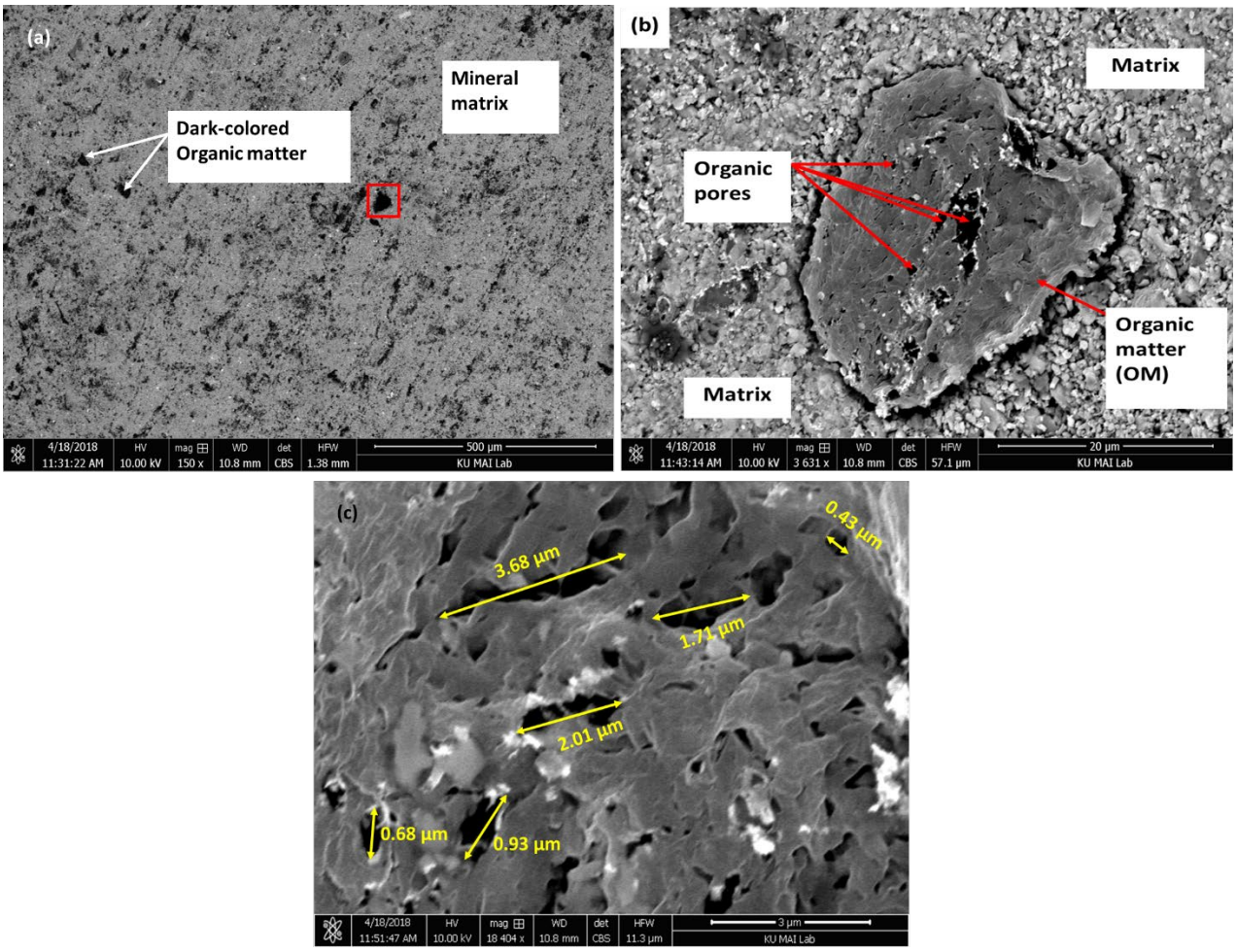

Figure 2.6: BSE images of Sample A at different magnifications; 150x, 3,631x, and 18,404x, respectively

BSE images of Sample C (mechanically polished) at different magnifications are shown below (Figure 2.7) with distributions of organic matter, matrix minerals, and carbonate microfossils. At a higher magnification (Figure 2.7-right), the selected wispy depositional kerogen of interest (enclosed in red box) shows organic bubble pores.

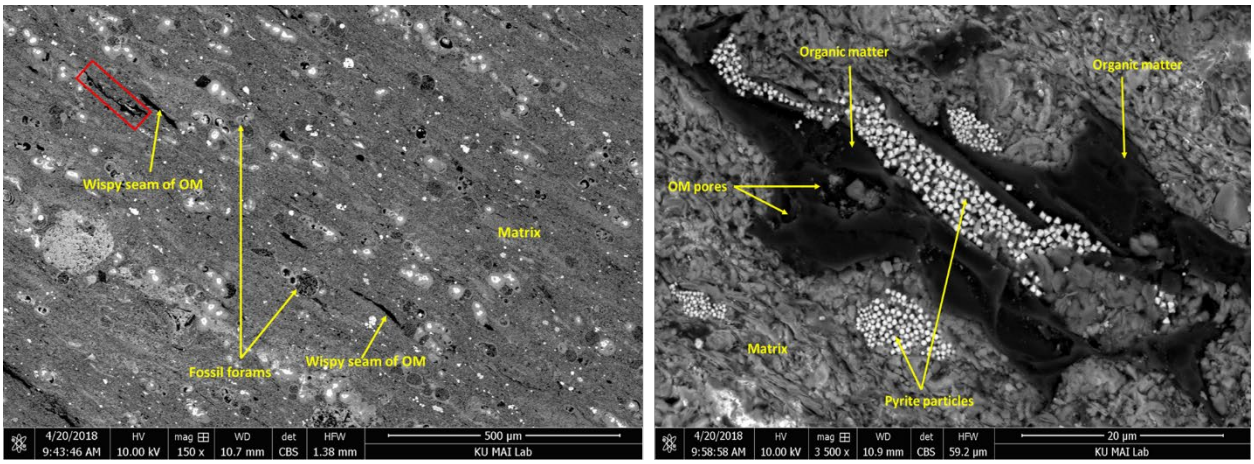

Figure 2.7: BSE images of Sample C at different magnifications to resolve organic pores in depositional kerogen

2.3.1.2 SEM Images of the LEF Shale Samples

SEM images of Samples A (Figure 2.8 - left) and B (Figure 2.8 - right) show the distribution of foraminifera fossils, which contained primary intra-particle pores. In some cases, the chambers are filled with kaolinite followed by migrated organic matter (OM). In other cases, calcite cements precipitate first, followed by pyrite. Compactional micro-fractures and micro-breccia cut across the calcite cement, and remaining pore space is filled by migrated OM. The micro-fractures are believed to serve as migration pathways for the pre-oil bitumen into the primary pores (foraminifera chambers). It is presumed that depositional kerogen evolves to produce bitumen (hydrocarbon with varying viscosity- petroleum, resins & asphaltenes) at elevated temperatures associated with burial, but likely before maximum temperature is reached. The produced pre-oil bitumen/petroleum then migrates a short distance to occupy inter-particle, intra-particle, fracture, and breccia pores, including foraminifera chambers **[50, 51]**. The migrated bitumen transforms into solid bitumen (oil window) or pyrobitumen (gas window) with time and temperature, and is capable of generating organic pores after its emplacement. The migrated OM (bitumen/solid bitumen) includes fully filled pores with solid bitumen containing common organic pores and

meniscus-type (partially-filled pores) of solid bitumen that tends to lack organic pores. It is worth noting that both porous migrated OM and the nonporous migrate OM are found side-by-side in the same sample. These may have had different compositions originally and gone through the same thermal maturation process, or they may have been emplaced at different times and experienced different thermal maturation post emplacement. In analyzing the thousands of examples imaged of particles of depositional kerogen and pores filled with migrated OM, it is estimated that only 2% of the depositional kerogen is porous, whereas 80% of the migrated OM is porous; the remaining 18% are contributions from both OM types not easily differentiated.

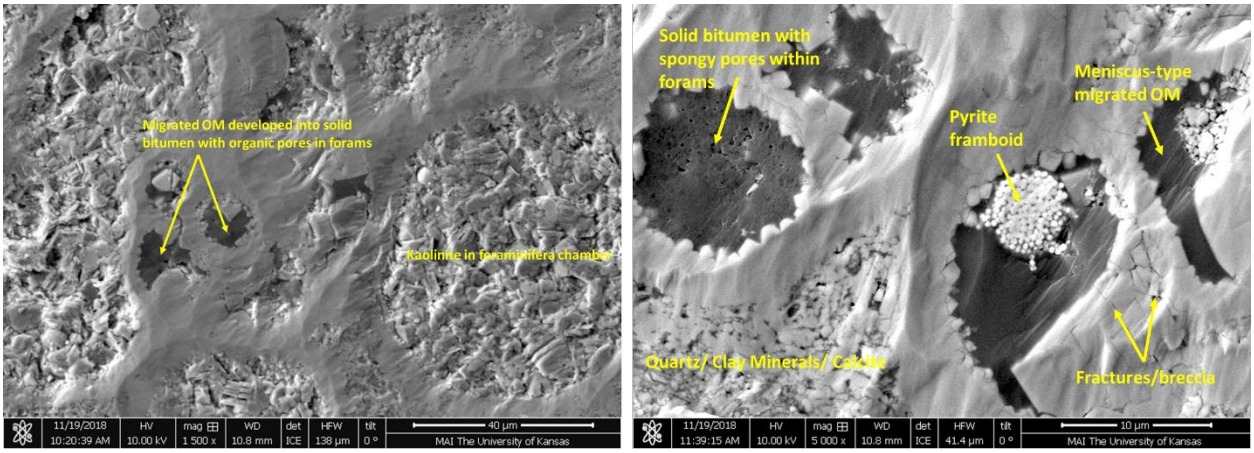

Figure 2.8: SEM images of Sample A (left) and Sample B (right) showing the distribution of diagenetic minerals

2.3.1.3 EDS Analysis on SEM Images of the LEF Shale Samples

Figure 2.9 (left) shows the elemental distribution on an SEM image of Sample A with interpreted X-ray spectrum showing the relative proportions of each element (Figure 2.9– right). Oxygen (O) has the highest weight percentage of 39.6 wt. %, followed by carbon (C) with 26.2 wt. %, and calcium (Ca) with 19.2 wt. %. The carbon (C), calcium (Ca), silicon (Si), aluminum (Al), iron (Fe), and sulphur (S) elements would be inferred as coming from organic matter/kerogen, calcite, quartz, clay minerals (kaolinite), and pyrite.

The EDS analysis on the SEM image of Sample B (Figure 2.10 - left) with interpreted X-ray spectrum showing relative proportions of each element (Figure 2.10 - right) shows higher carbon (C) and calcium (Ca) content than that of Sample A but with reduced oxygen (O) and silicon (Si) content because of the different regions of analysis. In addition to all the elements listed for Sample A, Sample B shows additional presence of sodium (Na) inferred to be albite.

Figure 2.11 shows the EDS analysis on the BSE image of Sample C with interpreted X-ray spectrum showing relative proportions of each element (Figure 2.11 – right). Carbon content (kerogen) is highest at 45.9 wt. %, followed by oxygen with 26.1 wt. %, and silicon (quartz) with 9.7 wt. %., respectively.

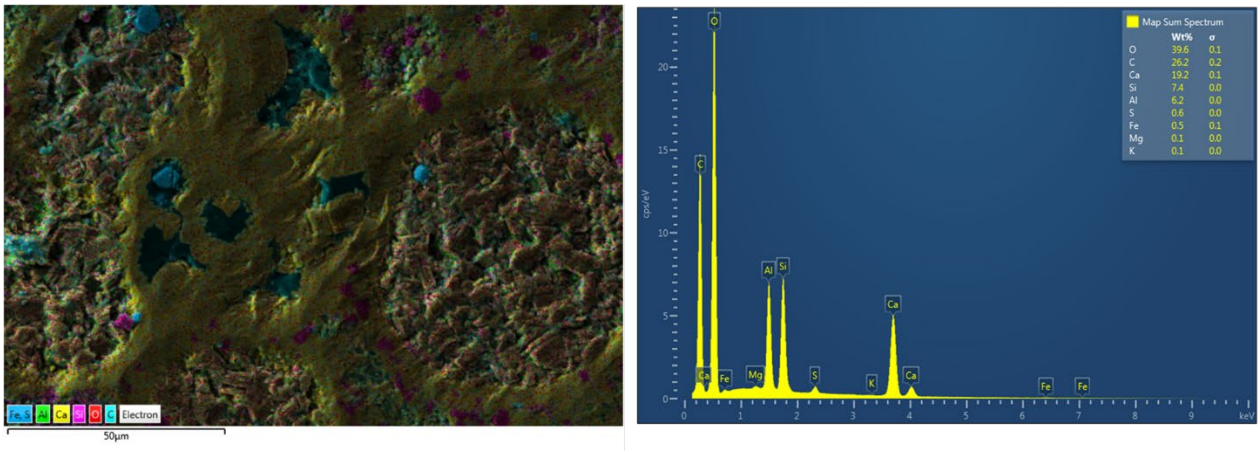

Figure 2.9: EDS analysis of the SEM image of Sample A showing different colors representing identified elements; turquoise (C), red (O), purple (Si), yellow (Ca), green (Al), and light blue (Fe & S)

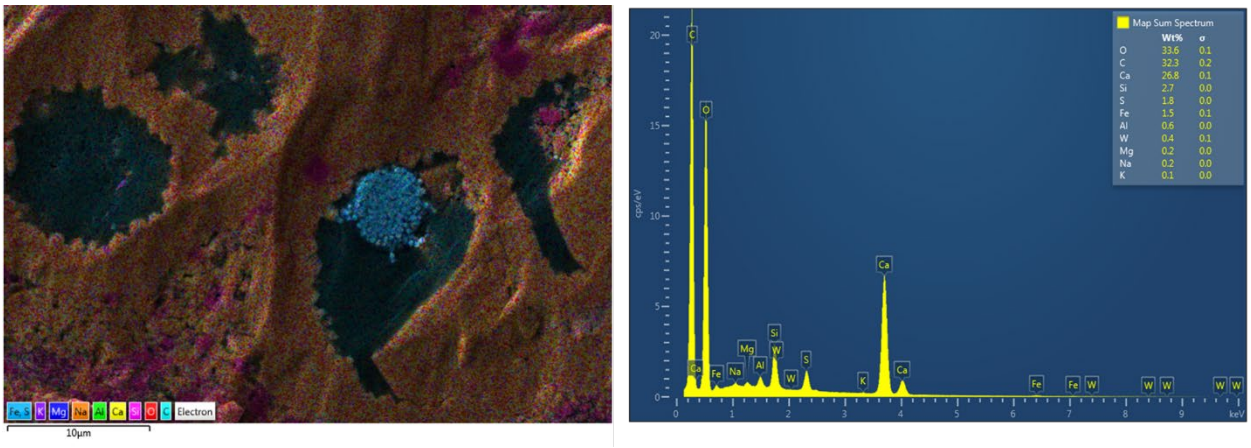

Figure 2.10: EDS analysis of the SEM image of Sample B showing different colors representing identified elements; turquoise (C), red (O), purple (Si), yellow (Ca), green (Al), and light blue (Fe & S)

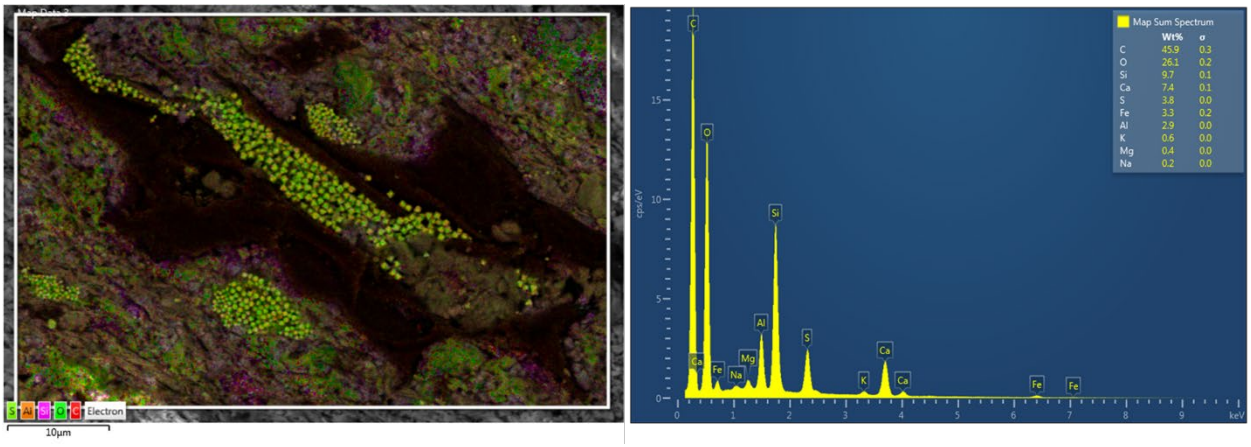

Figure 2.11: EDS analysis of the BSE image of Sample C with different colors representing identified elements; red (C), purple (Si), yellow (Ca), green (O), light blue (Fe), light green (S), and orange (Al)

2.3.2 LEF Shale Samples Before and After Hydrocarbon Gas Huff-n-Puff

In the SEM/BSE images, the displacement of some of the organic matter presumed to be migrated OM (bitumen) from its original position before the experiment was observed after the gas exposure experiment. Some of this appeared to migrate to new sites in the sample. This suggests that exposing the samples to hydrocarbon gas at such high temperature of 125°C in the experiments did have some effect on the migrated OM (bitumen). There were no examples of depositional kerogen being displaced or disappearing after the experiments and no evidence of

change in the rock microstructure or matrix minerals. EDS analysis of selected regions of interest (ROIs) on the SEM/BSE images before and after gas injection showed little or no change in the relative proportions of the elemental composition of the matrix minerals. Figure 2.12 and Figure 2.13 show some noticeable features on the BSE images of Sample B before and after gas injection at different positions; white arrows point to existing features before gas injection, while blue circles represent dark features/bitumen displaced to new sites through gas injection. Displaced organic matter/bitumen after gas injection are circled in yellow in the BSE image before gas injection and replaced with yellow question marks on the BSE image after gas injection.

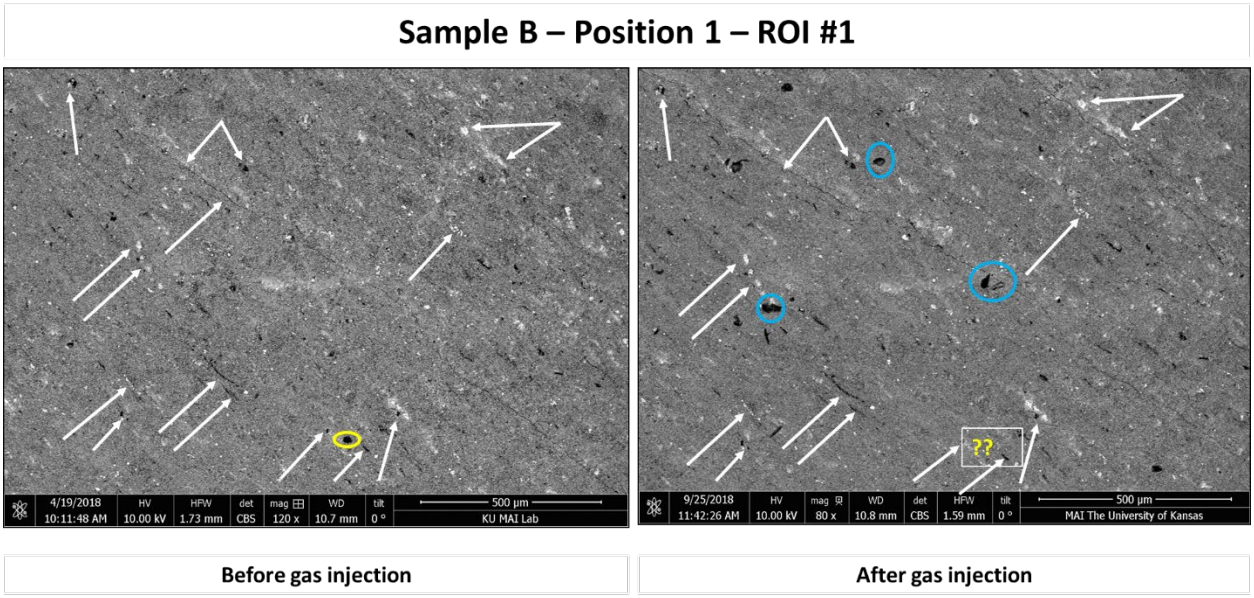

Figure 2.12: Marked features on BSE images of Sample B to confirm location; white arrows point to existing features before and after gas injection, yellow circle represents a dark feature/bitumen displaced after gas injection, and blue circles represent dark features displaced to new locations

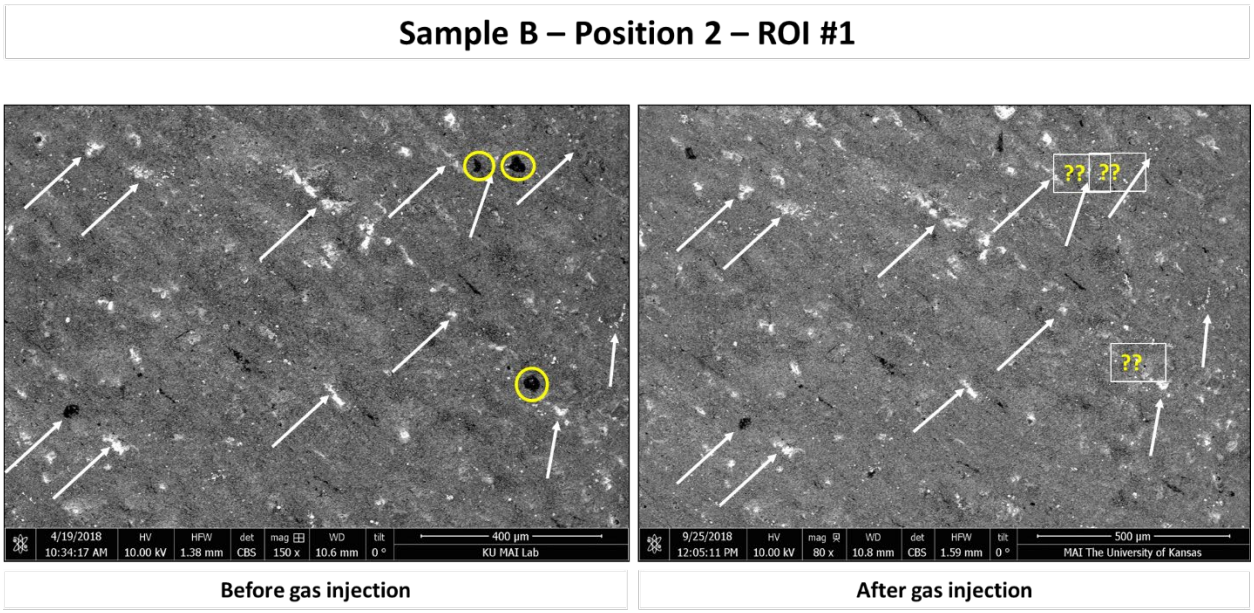

Figure 2.13: Marked features on each BSE image of Sample B to confirm location; white arrows point to existing features before and after gas injection, and yellow circle represents a dark feature(s) displaced after gas injection

The corresponding EDS analysis on a region of interest (ROI) selected at position 1 on Sample B is shown below in Figure 2.14 with the relative proportions of the elements within the region listed in Table 2-5. No significant changes occurred in the matrix mineral distribution after gas injection other than the displacement of bitumen observed earlier. Thus, hydrocarbon gas only affects the bitumen hydrocarbon and not the mineral matrix.

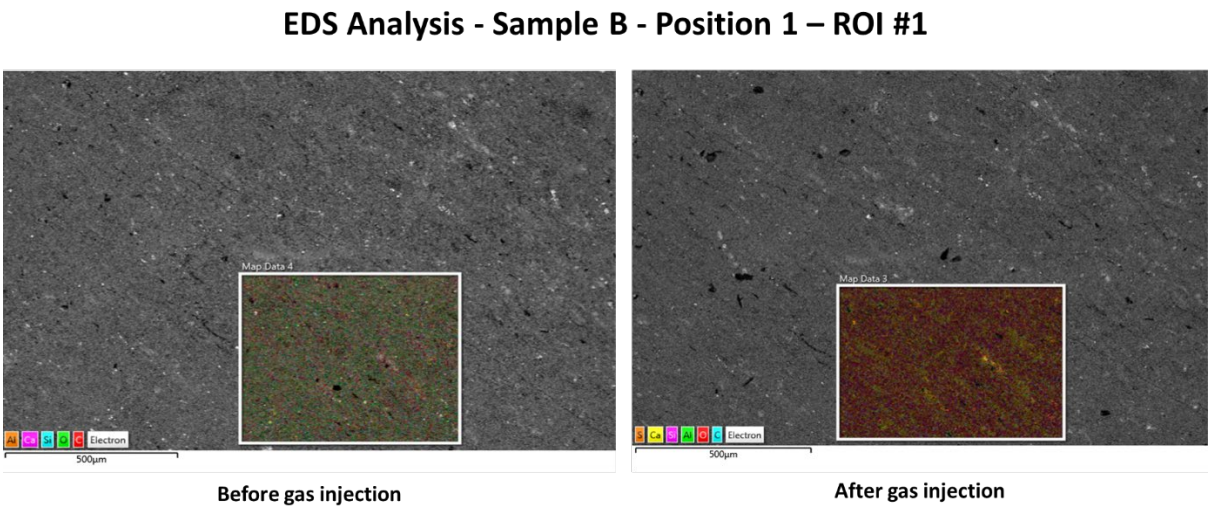

Figure 2.14: EDS analysis on selected ROI of a BSE image of Sample B before and after gas injection

Table 2-5: Relative proportions of elements within selected ROI before and after gas injection in Sample B

Elements	Before gas injection (*wt. %*)	After gas injection (*wt. %*)
Carbon (C)	18.6	17.5
Calcium (Ca)	20.5	21.2
Silicon (Si)	11.6	12.3
Aluminum (Al)	3.8	3.7
Iron (Fe)	0.8	0.9
Magnesium (Mg)	0.4	0.5
Oxygen	42.0	41.9
Sulphur (S)	0.9	0.9

In a similar manner, Figure 2.15 shows the EDS analysis of selected ROIs on BSE images of Sample B before and after gas injection at a different position; the relative proportions of the elements within the region listed in Table 2-6. No significant changes were observed within the matrix mineral distribution after gas injection.

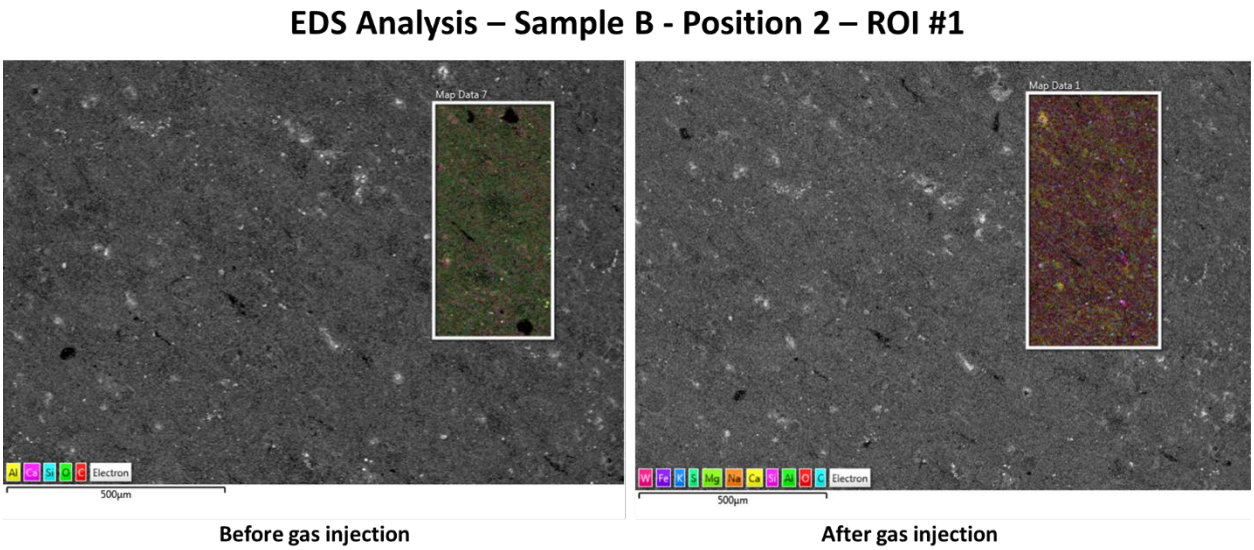

Figure 2.15: EDS analysis of Sample B within selected ROI before and after gas injection

Table 2-6: Relative proportions of elements within selected ROI before and after gas injection in Sample B

Elements	Before gas injection (*wt. %*)	After gas injection (*wt. %*)
Carbon (C)	18.6	17.5
Calcium (Ca)	20.5	21.2
Silicon (Si)	11.6	12.3
Aluminum (Al)	3.8	3.7
Iron (Fe)	0.8	0.9
Magnesium (Mg)	0.4	0.5
Oxygen	42.0	41.9
Sulphur (S)	0.9	0.9

2.3.3 3D FIB-SEM Volumes

Overall, more than 200 slices were acquired for each LEF shale sample, but 106 slices of each sample were used to compare one volume to the other. Table 2-7 lists the analyzed FIB-SEM data for the organic regions of all three (3) samples and the inorganic portion of Sample B (Inorganic); the representative elementary volumes (REV) of the LEF shale samples range from 92 μm^3 for Sample A, 211 μm^3 for Sample B, 146 μm^3 for Sample C, and 132 μm^3 for the inorganic volume of Sample B, respectively. Figure 2.16 shows the rendered 3D volumes of each sample; black represents pore/organic matter, gray represents the matrix, and white represents pyrite/dense materials.

Table 2-7: FIB-SEM processed data for each LEF organic region

LEF Shales	Image size (pixels) (x, y, z)	Image resolution (nm/pixel) (x, y, z)	Physical size (µm) (x, y ,z)
Sample A	1222 x 658 x 106	6.57 x 6.57 x 20	8.02 x 5.48 x 2.1
Sample B	1486 x 896 x 106	7.72 x 7.72 x 20	11.46 x 8.77 x 2.1
Sample C	1471 x 880 x 106	6.50 x 6.50 x 20	9.56 x 7.26 x 2.1
Sample B (Inorganic)	1430 x 882 x 106	6.50 x 6.50 x 20	9.27 x 6.77x 2.1

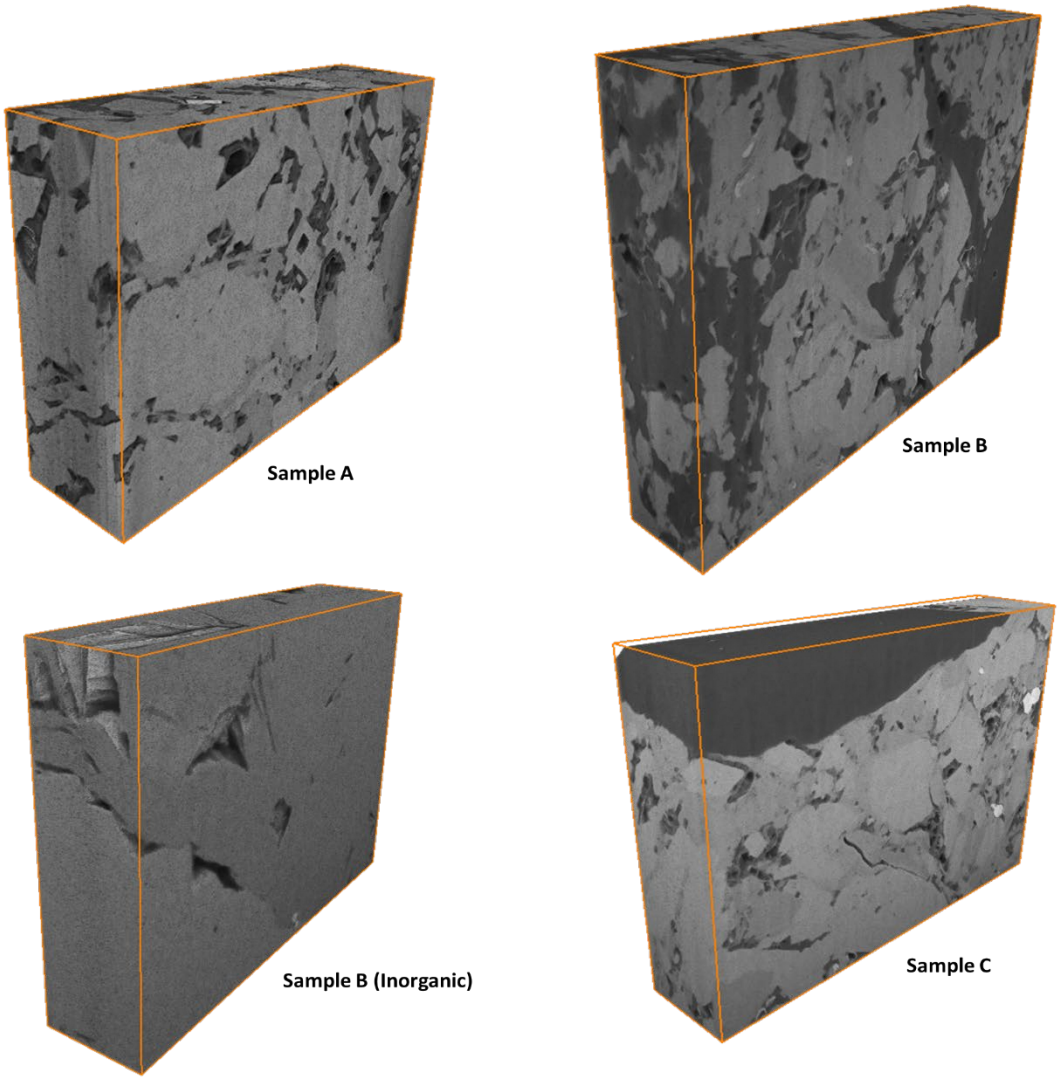

Figure 2.16: Reconstructed FIB-SEM volumes of the LEF shale samples; black/dark represents organic pores/organic matter, gray represents the matrix, and white represents pyrite

2.3.3.1 Volume Fraction Calculation

The volume fraction (*vol. %*) of each phase within the FIB-SEM volume was estimated as a fraction of the total volume through the segmentation process. Figure 2.17 shows the segmented

volumes of each sample, where different colors represent different phases within the volume. The estimated organic porosity in each LEF is believed come from contributions from both depositional kerogen and migrated organic matter, with the greatest contribution from migrated OM. The inorganic porosity is mostly from the inter- and intra-particle pores. Table 2-8 lists the calculated volume fractions of each phase within the LEF shale samples. At the pore-scale, Sample B has the highest volume fraction of organic matter, followed by Sample C but both samples have organic porosities less than that of Sample A with the lowest volume fraction of organic matter. The volume fraction of OM in each REV is converted to weight fraction equivalent of total organic carbon (TOC) by assuming OM density of 1.3 g/cc together with the bulk density value of each sample (Table 2-1). The TOC equivalent of each sample except the inorganic sample (Table 2-8) is found to be higher than the measured core analysis (Leco TOC).

Table 2-8: Volume fraction of each component within the FIB-SEM volume of the LEF shale samples

Material/Phases	**Sample A**	**Sample B**	**Sample C**	**Sample B (Inorganic)**
Pores	2.11	1.65	0.87	1.46*
Organic matter	13.2	27.2	17.8	-
Matrix	84.69	71.15	80.95	98.54
Pyrite	-	-	0.38	-
TOC-equivalent (*wt. %*)	7.4	15.1	9.8	-

* Volume fraction of inorganic porosity

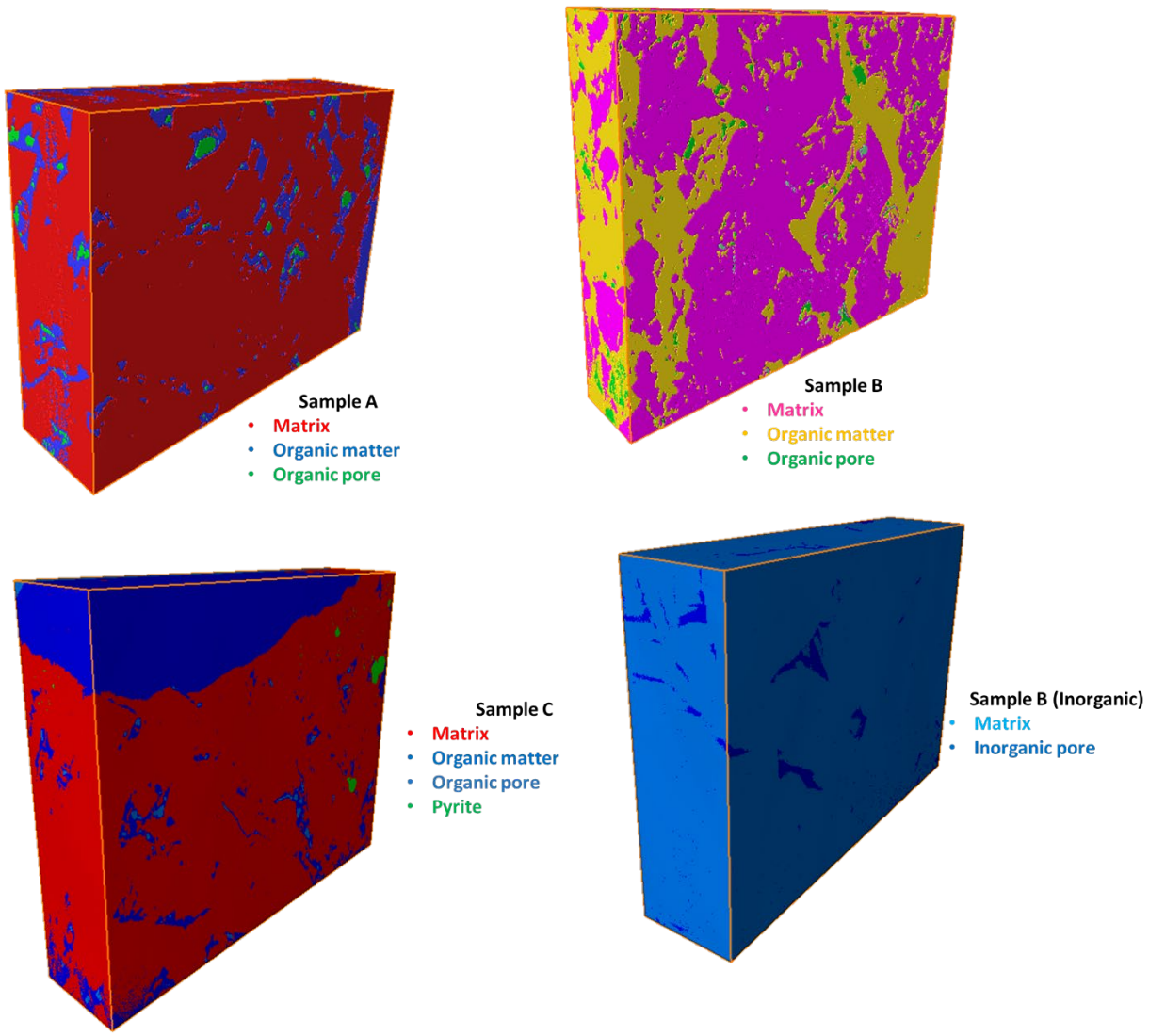

Figure 2.17: Segmented FIB-SEM volumes of a LEF shale sample, where different colors represent different phases within the grayscale image

2.3.3.2 Surface Mesh

From the segmented volume, a network of triangles or mesh can be created within PerGeos to represent each phase with a 3D surface; the triangles are grouped into patches describing the boundary between the inner and outer regions. The area of individual patches of a surface are calculated in addition to the volume. Table 2-9 lists some calculated pore parameters including surface area and volume of each surface-generated 3D volume. It can be observed than the organic

pores have relatively higher surface area-to-volume ratios than the inorganic pores (Sample B-Inorganic). It is expected that the high surface area-to-volume ratios contribute significantly to the adsorption of gas molecules during gas injection or permeability measurement. Furthermore, the higher surface area-to-volume ratio would have a significant contribution in diffusion of gas molecules into organic pores during the huff-n-puff process.

Table 2-9: Microstructure parameters of LEF shale samples from surface and pore space analysis

Parameters	Sample A	Sample B	Sample C	Sample B (Inorganic)
Surface area (μm²)	102.4	164.5	64.9	78.3
Volume (μm³)	1.69	2.9	0.98	1.77

2.3.4 Pore Network Models (PNM) of LEF Shale Samples

A pore network model details an approximation of the pore structure and its transport properties. It consists of a series of pores represented with spheres of similar volume and connected to one another through throats (represented as rods) with varying lengths as shown in

Figure 2.18; the pore network models are overlapped with the grayscale volumes. The degree of pore connectivity within a pore network model is essential for determining bulk transport properties and is defined as the ratio of the number of throats to the number of pores. Sample C has the least degree of connectivity between the pores, while Sample A has the highest degree of connectivity within the pores as listed in Table 2-10. In addition, the average distance that can be traveled between branching pores within the pore network is evaluated as the mean topological length, calculated as the sum of the channel length of each throat divided by the number of pores. The average topological length is longest for Sample B (Inorganic) as a result of its larger pores/fractures with fewer branching points.

Table 2-10: Generated pores and throats in the PNM of each LEF shale sample

LEF Samples	Pores	Throats	Degree of connectivity	Topological length (µm)
A	12,449	3,212	0.258	0.022
B	31,718	7,563	0.238	0.026
C	6,842	1,054	0.154	0.012
B (Inorganic)	14,064	3,125	0.222	0.030

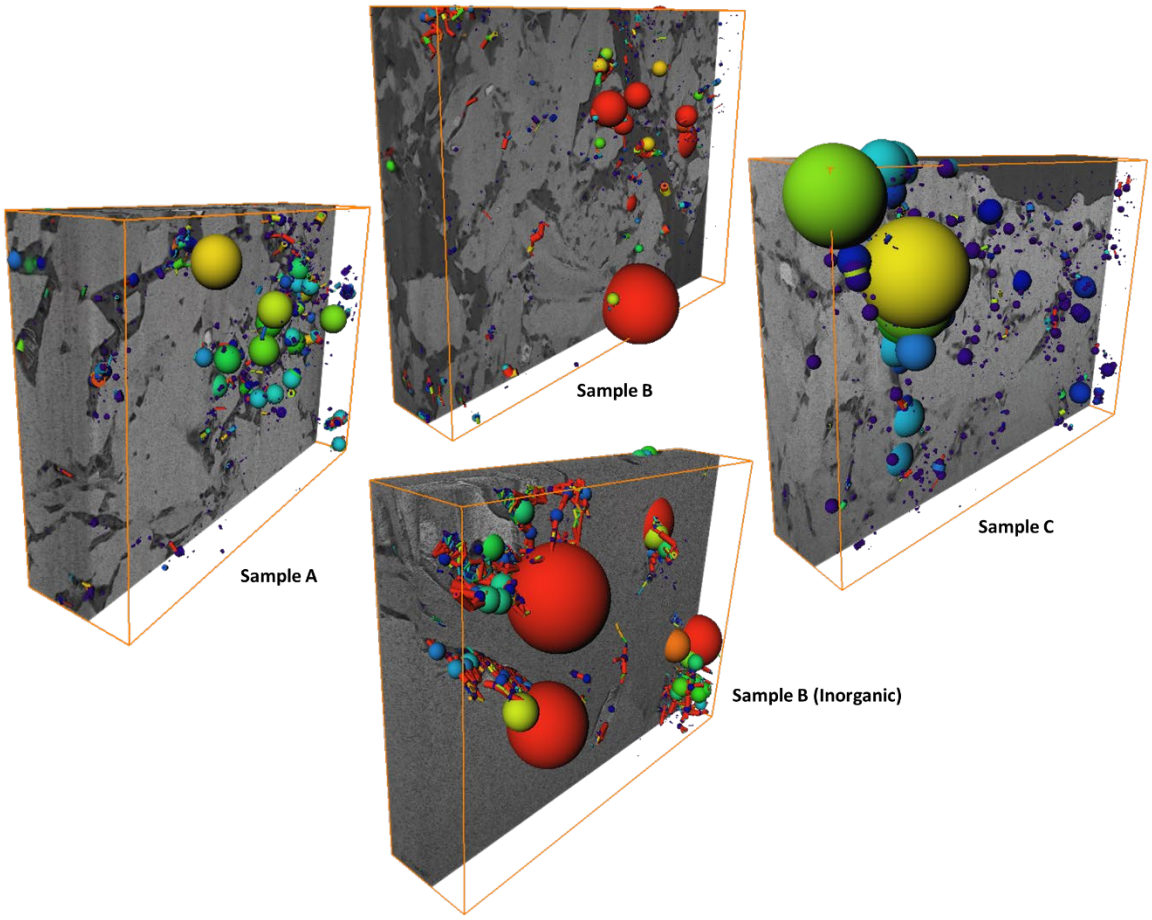

Figure 2.18: Generated pore network models of the LEF shale samples; pore sizes are scaled according to the volume, while the coloring of the pore is according to the equivalent radius. Throats are colored based on the channel length and scale is according to the equivalent radius.

2.3.4.1 Shape Factor of Extracted Pores

For a perfect sphere, the shape factor (β) equals 1; the higher the shape factor, the more the shape of the pores deviate from a sphere. It is observed that approximately 1.5% of the organic pores in Sample A have shape factors greater than 10 (large pores), whereas 98% of the organic pores have shape factors ≤ 5 (relatively spherical). Most of the organic pores observed in SEM/BSE and FIB-SEM images show relatively spherical pores in migrated organic matter and large pores in depositional kerogen. Only 0.5 % of the pores in Sample A have shape factors between 5 and 10 attributed to contributions from both types of organic matter (depositional and migrated). On the other hand, 100% of the organic pores in Sample B have shape factors between 0 - 50, alluding to relatively large pores. Sample C has 99.5% of its organic pores with shape factors ≤ 5 (relatively spherical pores) and only 0.5% with contributions from both types of organic matter (5 – 10).

Furthermore, the inorganic pores of Sample B (inorganic) show ~97.5% with shape factors ≤ 5 and only 2% with shape factors ≥ 10; the remaining 0.5% is assigned to shape factors between 5 and 10. Table 2-11 lists the average shape factors of each LEF pore network model.

Table 2-11: Average shape factor of the LEF shale samples

LEF samples	Average shape factor (β)
A	1.35
B	1.14
C	0.78
B- Inorganic	0.98

2.3.4.2 Pore and Throat Size Distribution

The equivalent pore diameter estimation within PerGeos is defined as the diameter of a sphere of the same volume as the pore. Figure 2.19 shows the pore size distribution of the organic

pores the LEF samples and Table 2-12 list the range of equivalent diameter (EqD) of pores and throats in addition to the average pore volume (PV). More than 80% of the equivalent pore diameters are ≤ 50 nm are observed, which make up micro- and meso-pores according to IUPAC, while the percentage of macro-pores (> 50nm) vary. The organic Samples (A and B) and the inorganic Sample B –Inorganic show a 10 – 16% range of macro-pores; Sample C shows the least percentage (5%). The micro- and meso-pores are often observed to be dispersed and isolated, and may participate in hydrocarbon transport when connected to a generated complex fracture network.

On the other hand, the throat sizes show a significant contribution (32%) presumed to be micro-fractures (≥100 nm) within the inorganic sample (B-Inorganic); a range of 14 – 26% of throats ≥100nm are observed in the organic samples (A, B, and C).

Table 2-12: Equivalent diameter of pores and throats within the pore network model of the LEF samples

LEF shales	**EqD-pores (nm)**	**EqD – throats (nm)**	**Average PV (nm^3)**
Sample A	13 – 415	5 - 368	1.58×10^5
Sample B	14 - 576	5 - 348	1.41×10^5
Sample C	13 - 320	6 - 261	0.47×10^5
Sample B - Inorganic	13 - 443	5 - 333	1.37×10^5

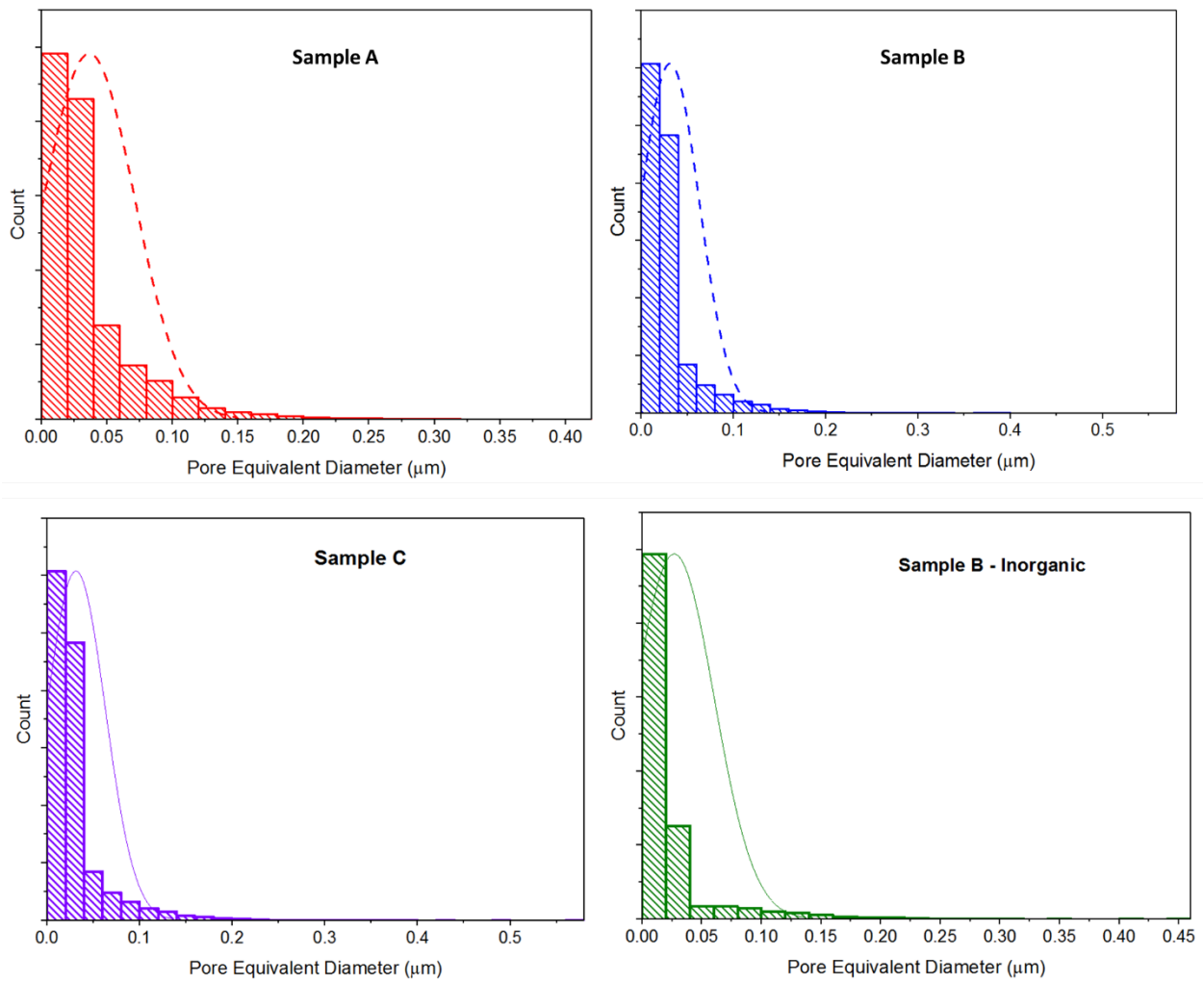

Figure 2.19: Equivalent organic pore size distribution of LEF shale samples

2.3.4.3 Tortuosity

In estimating the hydraulic tortuosity (HT), we simulated single phase methane (CH_4) at an inlet pressure of 3,500 psi and outlet pressure of 3,000 psi with dynamic viscosity of 19.4×10^{-6} Pa·s in the *x*-, *y*-, and *z*- directions. The *x*-, *y*-, and *z*- directions are based on the allocated directions through image processing in PerGeos and not necessarily the vertical and horizontal directions of the core. In the organic pores, the hydraulic tortuosity (HT) points to Sample B in the *x*-direction

and Sample C in the *y*- and *z*- directions, as the porous media with significantly tortuous pathways (Table 2-13).

Table 2-13: Calculated hydraulic tortuosity of the pore network models of the LEF shale samples

LEF Samples	**HT - *x***	**HT - *y***	**HT - *z***
A	1.84	1.27	1.63
B	2.34	1.59	1.95
C	1.33	1.61	2.43
B - Inorganic	1.57	1.44	1.81

2.3.4.4 Permeability

The Kozeny-Carman (K-C) permeability is geometrically averaged and listed in Table 2-14 for each LEF shale sample. The geometric average of permeability components is expressed in Eq. (2-3) below. Sample C shows the lowest permeability, while all the other samples have the same order of magnitude as the measured core permeability.

$$k = \sqrt[3]{k_x k_y k_z} \tag{2-3}$$

Table 2-14: Geometric average permeability of the LEF shale samples

LEF Samples	Geometric average of permeability (*k*), mD
A	0.00480
B	0.00479
C	0.000633
B - Inorganic	0.00433

2.4 Conclusions

The current body of literature is missing a comprehensive study utilizing advanced imaging and analysis to investigate organic vs. inorganic tortuosity. The work presented here helps clarify the processes in the pore structure during huff-n-puff. The scope and applicability has also been

expanded for the use of imaging technology for unconventional reservoirs and IOR/EOR in this work. These results can be used in numerical simulations and rock characterization to aid in optimizing recoveries/economics of different scenarios for huff-n-puff. This work detailed the organic-rich, ultra-tight shale oil reservoirs and what is happening in the pore structure as well as providing a way to model the complexity in the pore structures.

Both SEM/BSE/EDS and FIB-SEM imaging techniques at different resolutions revealed the rock fabric of the LEF shale samples to be dominated by carbonate, quartz, and clay minerals. Diagenetic phases include calcite, kaolinite, and pyrite. These mineral phases occupy more than 70% of the volume, with organic matter and pores occupying the rest. Two types of organic matter were observed: depositional kerogen embedded in the matrix and migrated organic matter as infillings of foraminifer tests and other open pores. Although both types of organic matter contribute to organic porosity, the dominant pores are in the migrated organic matter. More than 80% of the organic pores are associated with migrated organic matter and were determined to be relatively spherical, and most large organic pores are observed in depositional kerogen, but they contribute only 3% of the organic porosity; the remaining percentage is allocated to contributions from both types of OM, which are difficult to differentiate.

SEM/BSE/EDS analysis of experiments simulating hydrocarbon gas huff-n-puff recovery showed no significant effect on the rock microstructure and mineral matrix, but did cause displacement of migrated organic matter (bitumen) from original locations. The injected gas is predominantly methane, which makes it capable of penetrating more than 80% of the organic pores with sizes $\leq$ 13 nm. These pores are often observed to be dispersed and isolated, and may participate in hydrocarbon transport when connected to a generated complex fracture network.

Pore network models extracted from FIB-SEM imaging captured relevant pore structure of the LEF shale samples with practical REV within 100 μm^3. Pore connectivity is observed to be limited especially in Sample C. The geometric rock properties estimated from the pore network models show permeability to vary in a close range with the tight rock analysis (TRA) permeability measurements except for Sample C, whose organic pore volume fraction was estimated 0.87 % with the least degree of connectivity.

Publication:

S. Cudjoe, R. Barati, R. Goldstein, J. Tsau, B. Nicoud, K. Bradford, A. Baldwin and D. Mohrbacher, "An Integrated Pore-Scale Characterization Workflow for Hydrocarbon Gas Huff-n-Puff Injection into the Lower Eagle Ford Shale," in *Unconventional Resources Technology Conference (URTeC)*, Denver, 2019.

3 CHAPTER 3: APPLICATION OF RAMAN SPECTROSCOPY

Microscopic analysis including transmitted light, UV epifluorescence, BSE, and FIB-SEM carried out on Lower Eagle Ford (LEF) shale samples, selected from similar depths, show complex depositional fabrics, kerogen, migrated organic matter, and diagenetic history. It is well known that LEF samples contain depositional kerogen and migrated organic matter. Much of the migrated organic matter occupies diagenetically reduced primary porosity. Some of this organic matter is not porous, while some contains large pores and other contains a fine network of nanopores. Where thermal maturity is one control on porosity in organic matter, there is also a control of composition and origin.

This chapter investigates the chemistry of organic matter *in situ* using Raman spectroscopy, to begin to understand what, other than thermal maturation, leads to porosity in both depositional kerogen and migrated organic matter. This is used to evaluate the nature of the pores in LEF, and to assess the impact of hydrocarbon gas injection on organic porosity.

3.1 Introduction

Organic-rich shales are deposited with organic matter (kerogen) and primary porosity, both of which evolve at greater depths of burial, and result in thermal maturity including oil, condensate and/or gas, and evolving the pore system. Both vitrinite reflectance ($\%R_o$) and T_{max} from Rock-Eval have their shortcomings in determining the thermal maturity of shales, one being dependent on extricating a certain maceral that is not always common in marine rocks or rocks of a particular age; the other being a bulk technique, and both becoming less reliable in the presence of free hydrocarbons like bitumen in shale samples or oil-based drilling mud contamination.

Raman spectroscopy is a form of vibrational spectroscopy used in the structural characterization of a wide range of materials, including carbonaceous/graphitic materials [52]. Monochromatic radiation with a known wavelength impinging on a sample causes most of the radiation to be transmitted without change, while some of it is scattered. The scattered radiation when analyzed is observed to have spectral shifts providing information on the molecular structure of the sample. The shift in the frequency of the scattered radiation is referred to as Raman scattering, which is dependent on the masses of the atoms involved and the strength of the bond between them [53].

Graphite provides the basis for interpreting Raman analysis of sp^2 carbons like organic matter/kerogen [52, 54] and is made up of 3D multilayer graphene sheets stacked in an AB Bernal arrangement [55]. Graphite is characterized by hybridized sp^2 hexagonal networks of carbon (C) atoms with covalent bonding between C-atoms within a plane, and weak van der Waals interaction between planes. Basic structural properties of graphite are the in-plane crystallite size and out-of-plane stacking order [56, 57]. Raman spectroscopy is sensitive to the structural changes that occur in the symmetry of carbonaceous/graphitic materials, thereby providing unique vibrational and crystallographic information in addition to physical properties pertaining to electrons and phonons [58]. The Raman spectrum of carbonaceous materials is divided into first-and second-order regions based on the degree of crystallinity [59]. Most structural information of carbonaceous/graphitic materials is contained in the first-order Raman spectrum between 1000 and 1800 cm^{-1}, while the second order Raman spectrum (2000 – 3500 cm^{-1}) corresponds to overtone of the *D*-band and is sensitive to the process of graphitization [55, 52]. The Raman spectrum of graphite in the first order consists of an intense *G*-band occurring around ~1580 cm^{-1}, associated with E_g phonon arising from the **Γ** point [55].

Moreover, a disordered induced *D*-band appears at ~1350 cm^{-1} in the first-order Raman spectrum due to defects and strained lattice regions [56, 52]. This band is assigned to an A_1' non-degerate mode arising from the high symmetry **K** point of the Brillouin zone (BZ). Structural defects persist in all carbonaceous/graphitic materials but differ depending on the material, giving rise to unique applications such as composition-dependent thermal maturity indicators. Defects in organic matter (kerogen) pertaining to thermal maturity are observed in the alteration of the chemical structure of kerogen during catagenesis (onset of aromatic rings) and metagenesis stages (graphitization) to produce thermogenic petroleum. The onset of aromatization due to maturity leads to the removal of C-H bonds and cyclane groups, which is often reflected as organic porosity in thermally mature shale formations [60]. The *G*-band is observed in defect-free samples (metagenesis and/ or less mature kerogen) and its intensity appears uniform over a feature of interest, while the D-band intensity is localized at defective crystalline structures, mostly at the edges [57, 54]. Therefore, the relative intensity of *D* to *G* provides a good indicator for determining in-plane crystallite size or amount of disorder of the sample [56, 61].

The application of Raman spectroscopy as an analytical tool for structural characterization of carbonaceous/graphitic materials in addition to evaluating thermal maturity in organic-rich shales has gained widespread recognition over the years. Kelemen and Fang [54] first explored the maturity-related information derived from coals and kerogen at the catagenesis stage using Raman spectroscopy. While, Ferrari and Robertson [59] have shown that the Raman spectrum depends mainly on the ordering of sp^2 sites and indirectly on the fraction of sp^3 (diamond-like) sites. Other researchers have used Raman spectroscopy for the evaluation of thermal maturity in organic-rich shales including ([62, 63, 64, 65, 66], and references therein). None of these studies have been

focused on the structural changes associated with both depositional kerogen and migrated organic matter as part of diagenesis, thermal alteration, and porosity evolution in shales.

As part of the initial stages of implementation of a gas huff-n-puff operation in the Eagle Ford unconventional reservoir, the objective of this work includes: 1) determine structural changes associated with the maturation of depositional kerogen using Raman spectroscopy; 2) compare that to Raman-determined structural characterization of organic matter that migrated into pores at a later stage; 3) assess compositional controls on Raman characterization of thermal maturity and 4) investigate the effect of hydrocarbon gas huff-n-puff on selected organic matter types *in-situ* with Raman spectroscopy.

3.1.1 Predicted Structural Evolution of Kerogen during Thermal Maturation

Biopolymers from preserved organic matter (OM) in fine-grained sediments are transformed into consolidated and insoluble kerogen through microbial activity, and the resulting kerogen undergoes thermal evolution to produce thermogenic petroleum and a residue [67, 68]. The diagenesis stage of thermal evolution is characterized by a decrease in oxygen content, while the catagenesis stage is described by a decrease in hydrogen content [69]. Three (3) types of kerogen are classified based on the origin of the organic matter and the evolution stage: (1) Type I, (2) Type II, and (3) Type III, respectively. Figure 3.1 shows chemical models built on analytical data to describe changes in chemical composition of kerogen at each stage of evolution, modified after the work of Behar and Vandenbroucke [60].

Kerogen-Type I is commonly found in lacustrine deposits with high H/C and low O/C ratios. At the beginning of diagenesis, this type of kerogen is rich in long C-H bonds but poor in aromatic rings (Figure 3.1). Breaking of C-H bond chains during thermal maturation, yields significant amounts of paraffinic hydrocarbons (oil & gas) [60, 68].

Kerogen-Type II – commonly found in marine deposits with lower H/C and higher O/C ratios. Beginning of catagenesis is characterized by high cyclic structures with significant aromatic content (Figure 3.1). Naphthenoaromatic compounds with high sulfur content are formed after greater amounts of hydrocarbon are produced from catagenesis and residual polyaromatic structures undergo structural reorganization [70, 60].

Kerogen-Type III forms in continental deposits (humic coals) with low H/C and high O/C ratios; rich in aromatics and phenols (Figure 3.1). It is characterized by polyaromatic structures with low oil potential, which form a micro-porous solid partly filled with hydrocarbons from the catagenesis stage [71, 60]. The trapped hydrocarbons are expelled when cracked into gas [72]. Eventually, the micro-porous solid is transformed into triperiodic graphite with larger and more ordered aromatic structures in later stages of metagenesis [52, 73].

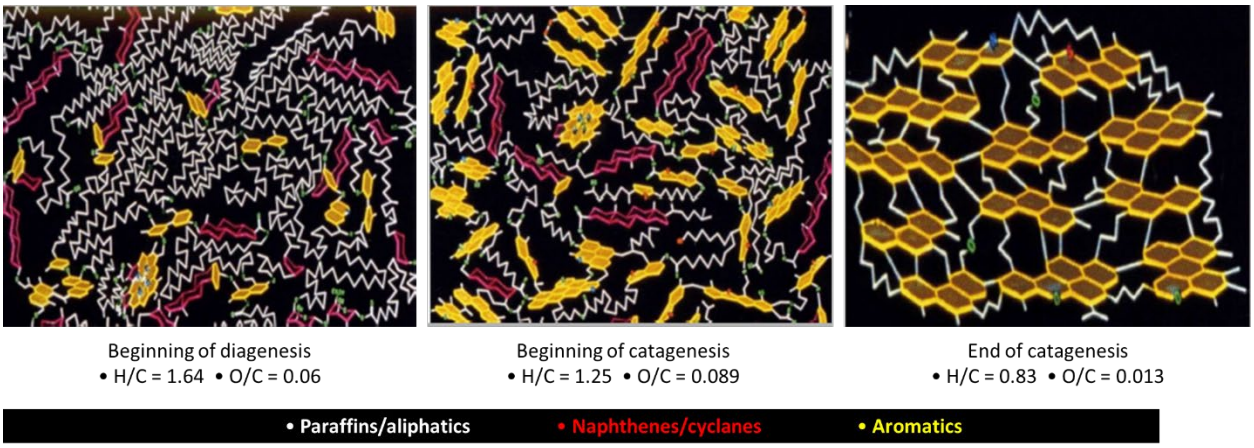

Figure 3.1: Chemical models of kerogen during thermal maturation (modified after [60])

3.1.2 Predicted Evolution of Bitumen during Thermal Maturation

Bitumen is described as a type of organic matter, soluble in organic solvents [74]. Its composition and appearance resembles that of petroleum and can be separated into paraffin-naphthenes and aromatic hydrocarbons, organic compounds containing nitrogen, sulfur or oxygen and asphaltenes [75]. Kerogen decomposes as part of the thermal evolution process to produce bitumen and thermogenic gas during primary cracking between temperatures of 80°C and 180°C [45]. Subsequently, the produced bitumen undergoes decomposition to produce oil and thermogenic gas. Under secondary cracking (>150°C), bitumen decomposes to form solid bitumen/pyrobitumen (carbon-rich coke) with developed organic pores.

3.1.3 Raman Parameters Related to the Thermal Maturity of Kerogen

The first-order Raman spectrum of a mature kerogen produces two main bands namely, the G-band (~ 1600 cm-1) and the D-band (~ 1350 cm-1) as shown in Figure 3.2 for a LEF sample in this study. While the G-band is consistent with the ordered and stacked aromatic clusters (graphite-like), the D-band corresponds to the disordered and poorly organized medium due to the removal of C-H bonds and cyclanes as thermal maturity increases. Therefore, changes observed to be associated with these two Raman bands in terms of the width and intensity can be used to interpret the Raman spectrum. Additional band shoulders (D2, D3, D4, etc.) are resolved by fitting with the Gaussian-Lorentzian algorithm [73, 76].

The Raman parameters include, the D-G band separation, the full width at half maximum (FWHM) of the G-band, and the intensity ratio of the D-band (ID) to that of the G-band (IG). These Raman parameters depend on the organization of defects in samples [76]. A good correlation can be developed between the thermal maturity (%Ro) and some of the Raman parameters from the spectrum (e.g., [64, 65], and references alike).

The width of the G-band is determined to be proportional to the bond-angle disorder at sp^2 sites [59]. As such, the narrowing of the G-band with a corresponding increase in the G-band intensity relative to the D-band is interpreted as increasing thermal maturity. The D-band is observed to shift towards lower relative wavenumbers due to increase in aromatic clusters to form more ordered materials [63]. Coupling the D band shift to the decreased FWHM of the G-band, an increase in the D - G separation is observed as thermal maturity increases. The D and G band separation is one of the best parameters to correlate against vitrinite reflectance [54]. The intensity ratio between D and G bands, either band height or band area, is found to be inversely proportional to the in-plane crystallite size in disordered graphite [56]. Therefore, the ID/IG ratio will increase with increasing disorder according the TK relationship [59].

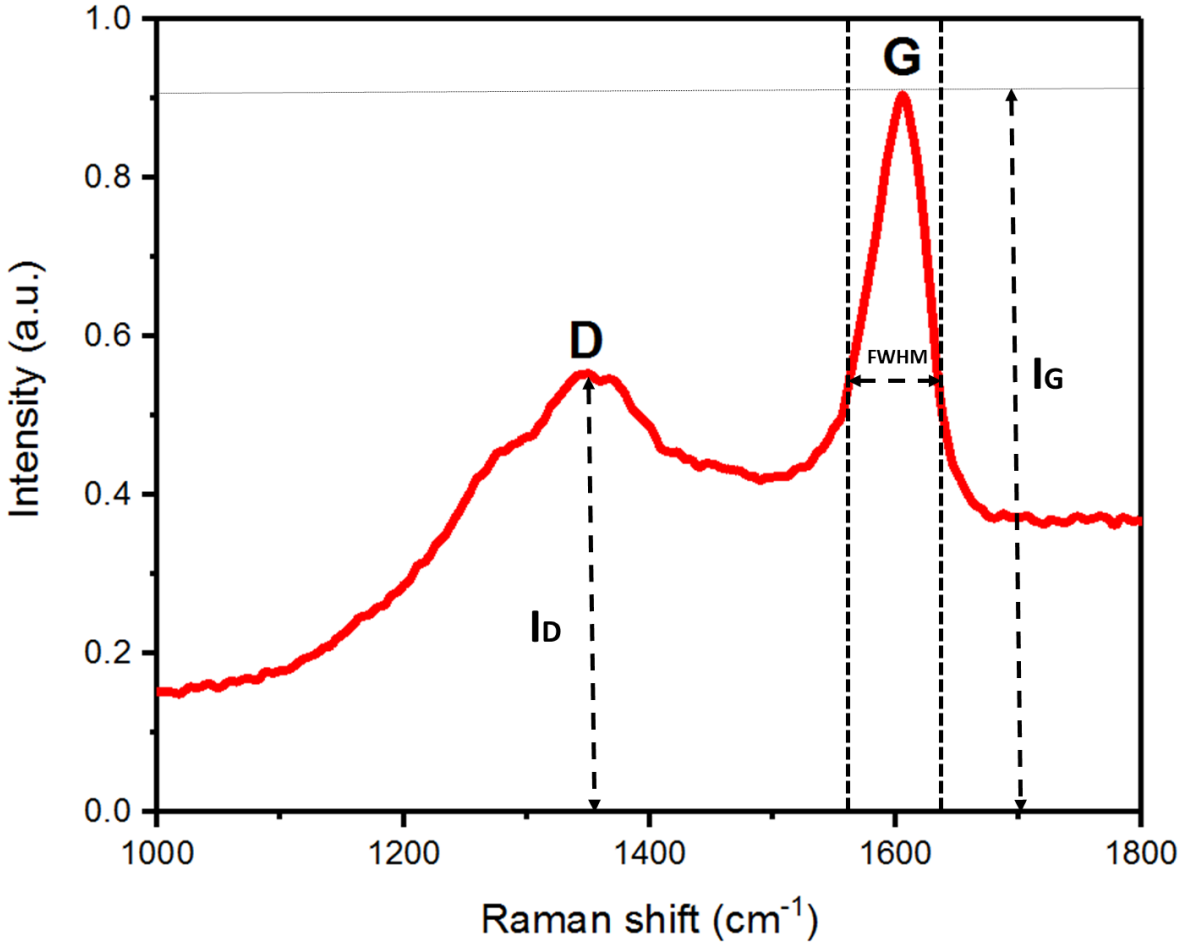

Figure 3.2: First-order Raman spectrum of a thermally mature lower Eagle Ford shale sample (Sample C) with labeled Raman parameters; the intensity of the G-band (I_G) is drawn outside of the G-band area due to lack of space.

3.2 Methods

3.2.1 Samples

The shale samples under study are from the LEF and are characterized to be in the oil window (kerogen type I-II) with thermal maturities in the range of 0.98 $\%R_o$ - 1.03 $\%R_o$ and measured TOC between 5.06 - 5.75 *wt. %* as listed in Table 3-1.

Table 3-1: Leco TOC and Rock-Eval pyrolysis measurements of the LEF samples [77]

LEF Samples	TOC (*wt. %*)	Vitrinite reflectance (%R_o)	S_1 (mg HC/g)	S_2 (mg HC/g)	T_{max} (°C)
A	5.75	0.98	8.58	11.81	452
B	5.06	1.01	8.88	11.77	454
C	5.29	1.03	6.81	11.10	455

3.2.2 Microscopic Analysis & Raman Measurements

Methodology employed initial sampling and preparation of doubly polished thin sections with alcohol for transmitted light and UV microscopy, and Raman spectroscopy. FIB-SEM and BSE studies were completed in a different phase of the study [77]. Raman analyses were completed with a Renishaw *inVia* Reflex spectrometer at the University of Kansas. Emission at 514.5 nm was used as the source with an adjusted laser power of 1 - 10 mW and a 2400 l/mm grating. The Raman backscattering was recorded at an exposure time of 30 s for 5 accumulation scans on all samples; this helped in reducing the fluorescence background to a minimum. Raman measurements were taken using the 100x objective and more than two measurements were taken of each type of organic matter for each sample.

3.2.3 Hydrocarbon Gas Huff-n-Puff

After Raman analysis, thin sections and rock chips of the LEF shale samples were placed in a huff-n-puff cell contained in an oven set at 125°C and the hydrocarbon gas was injected at a pressure of 3500 psi; the injected gas was allowed to soak for three (3) days as described in our other work on pore-scale characterization [77].

3.3 Results & Discussion

3.3.1 Microscopy of Depositional Kerogen & Migrated Organic Matter

Pore-scale characterization using BSE/SEM and FIB-SEM reveal two major types of organic matter, depositional kerogen and migrated organic matter (MOM) as observed in Figure 3.3. Depositional kerogen is identified as particles embedded in the mineral matrix as discrete grains, while MOM (bitumen) is easily identified as infills in chambers in foraminifer tests (intra-particle pores) and other open pores, such as inter-particle, fracture, breccia, and inter-crystalline. Figure 3.3 (left) shows the presence of globigerinid and other planktonic foraminifer tests for Sample B [77]. Organic matter, finely disseminated in the fine mineral matrix is likely a combination of both depositional kerogen and MOM, and cannot be easily segregated [78, 79].

While mostly filling cement-reduced primary pores, the MOM emplacement postdates precipitation of calcite, pyrite, quartz, and kaolinite cements, and micro-fracturing of calcite. Thus, the initial migration of OM into these pores is a space filler that is relatively late in the paragenesis [42]. FIB-SEM analysis of these samples show that ~98% of the extant pore space developed within the migrated OM, whereas only 1.5% developed in or was preserved from depositional kerogen; the remaining 0.5% is likely a contribution from both types of OM, which is not easily differentiated [77]. Thus, the MOM matured thermally to become porous after migration into Eagle Ford pores, and that rejuvenation of porosity in pores that had been previously occluded by MOM, is responsible for most of the porosity in the samples.

As the MOM filled pores relatively late in the paragenesis compared to the deposition of kerogen, it could be predicted that the two types of organic matter would show different Raman-derived structural indicators of thermal maturity, because of the their differing time-temperature histories. The kerogen should show evidence for higher maturity than the MOM, because of the MOM's late emplacement. On the other hand, it might be possible that since depositional kerogen

and MOM are fundamentally different chemically, that predictable structural indicators of thermal maturity are not seen, indicating that Raman spectroscopic indicators of thermal maturity are maceral dependent.

It was observed that, even in the mature oil window of the LEF shale samples, the depositional kerogen could either be without pores as seen in the SEM image (Figure 3.3 - left) or contained a low percentage of isolated pores (Figure 3.3 - right). In contrast, most of the MOM in the same samples contains spongy and bubble pores (Figure 3.3). A small proportion of the MOM is seen without pores, some having a meniscus configuration. These differences could be attributed to multiple compositions and multiple events of migration of organic matter, including both early migration events that had a long history at high temperature, and late migration events that were at high temperature for only a short amount of time. Moreover, the lack of pores in most depositional kerogen in the LEF shale samples could be attributed to thermogenic oil obscuring the developed pores or that the source/maceral is not prone to preserving or creating pores. It is therefore plausible that hidden pores within the depositional kerogen will be revealed once the oil cracks into gas.

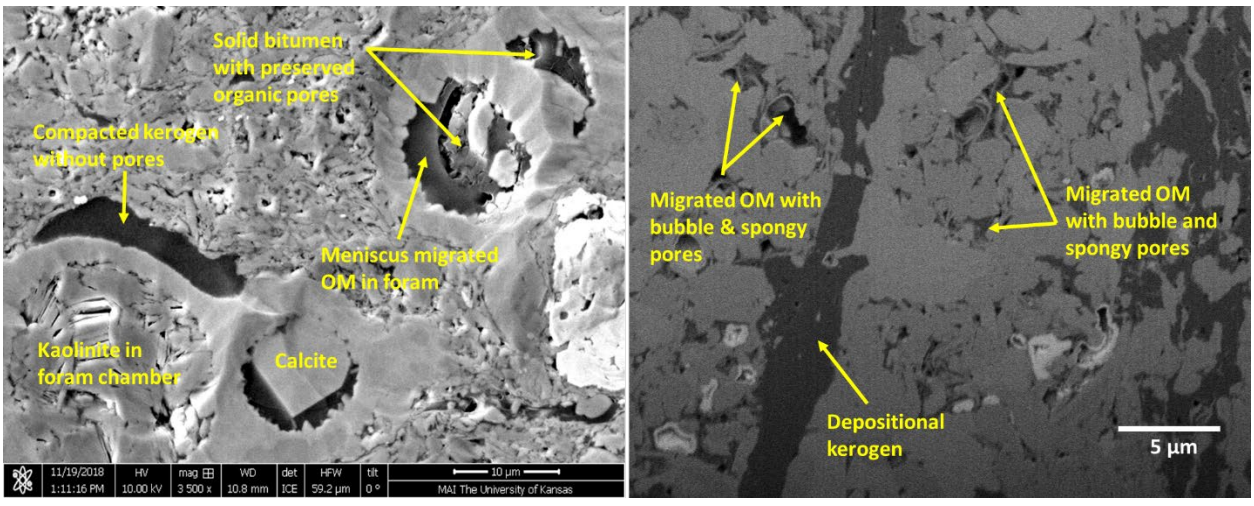

Figure 3.3: Depositional and migrated organic matter (bitumen) identified in SEM (left) and FIB-SEM (right) images, respectively, for Sample B at a thermal maturity of 1.01% [77]

Figure 3.4, 3.5, and 3.6 show transmitted light and UV epifluorescence photomicrographs for each of the LEF shale samples. Each shows globigerinid and other foraminifer tests filled with MOM, and depositional kerogen embedded in the matrix as particles. While, most depositional kerogen and MOM appear to be non-fluorescent in the UV images, some particles/spores show blue and yellowish fluorescence, whereas for the most part, the migrated OM appears to be non-fluorescent with the exception of a few red-orange fluorescent spots (Figure 3.4 - right).

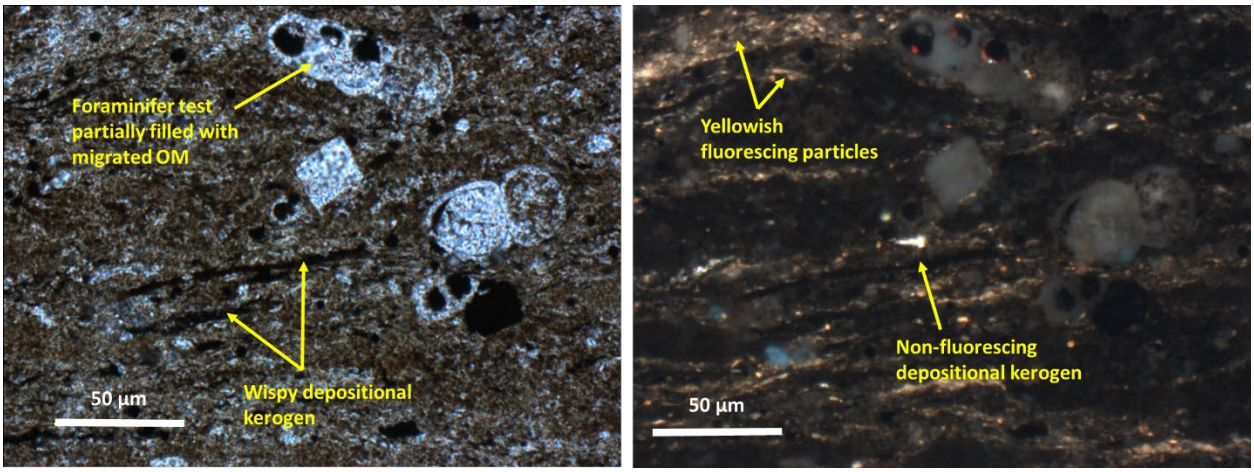

Figure 3.4: Transmitted light (left) and UV image (right) of Sample A at a thermal maturity of 0.98% with distributions of migrated OM and depositional kerogen

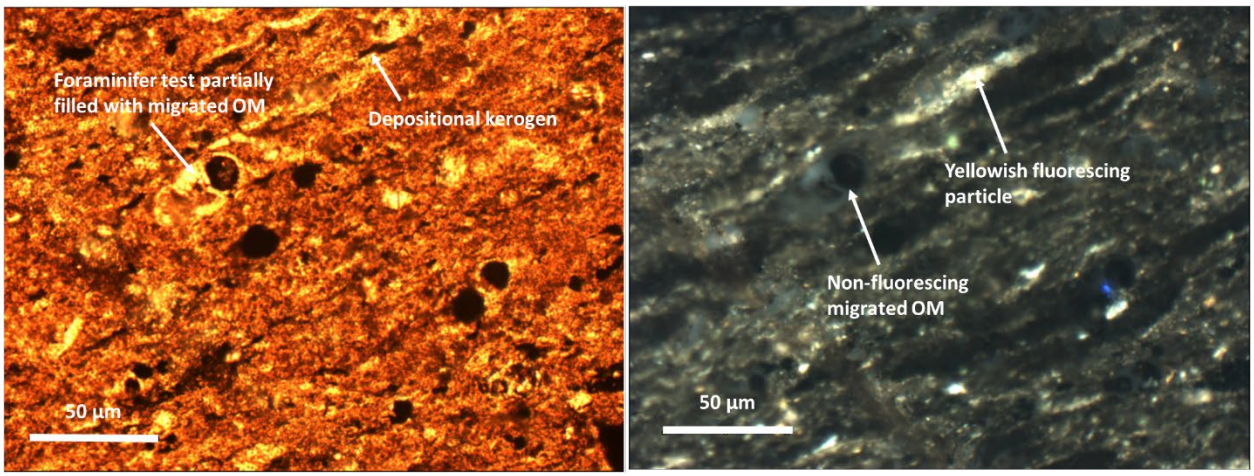

Figure 3.5: Transmitted light (left) and UV image (right) of Sample B at a thermal maturity of 1.01 % with distributions of migrated OM and depositional kerogen

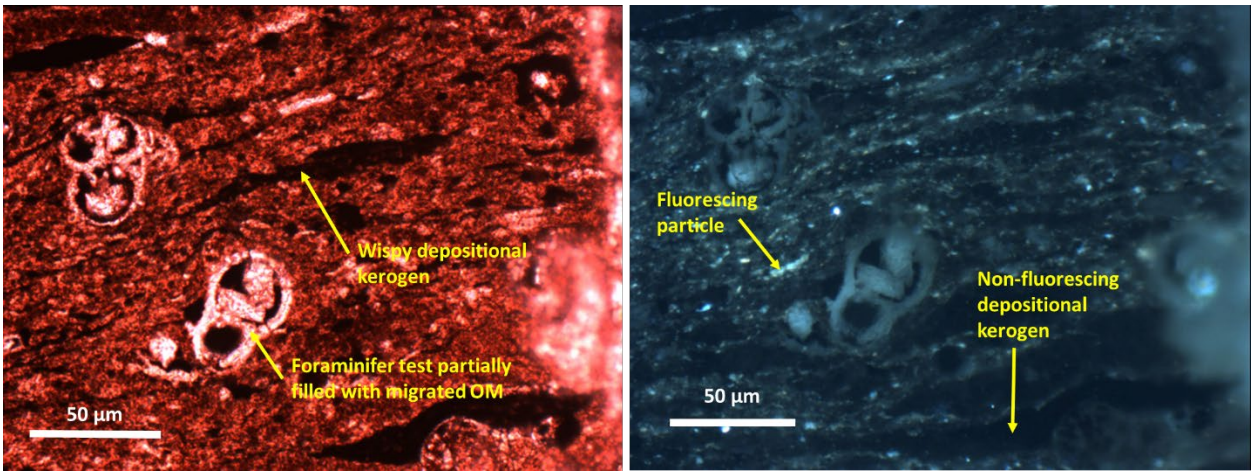

Figure 3.6: Transmitted light (left) and UV image (right) of Sample C at a thermal maturity of 1.03 % with distributions of migrated OM and depositional kerogen

The petrographic distinctions between depositional kerogen and MOM are consistent with observations by other studies of organic-rich shales, and are fit into a paragenesis of fabric evolution by Cudjoe et al [77]. Thermogenic petroleum produced from depositional kerogen is said to migrate into both inter-particle and intra-particle mineral pores (foraminifer tests) alike. A migrated bitumen phase solidifies into solid bitumen/pyrobitumen and preserves or generates pores; large bubble pores within the MOM are perceived to form when oil contained in the pores is cracked into gas. The depositional kerogen also can develop organic pores from solid bitumen/pyrobitumen contained within the kerogen during thermal maturation. However, not all observed organic pores can be said to have formed from thermal maturation as there is a possibility that some of these nanopores were already preserved in the macerals at the time of deposition [80]. The chambers of foraminifer tests survive compaction due to infills with authigenic minerals such as kaolinite, quartz, calcite, and pyrite. The migrated organic matter (bitumen) from late diagenesis fills up the remaining primary porosity left between the clay minerals and coccolith fragments [81, 43] .

3.3.2 Raman Measurements before Gas Exposure

The resulting spectra for both depositional kerogen and MOM before exposing the samples to hydrocarbon gas were in the first-order region from 1000 – 1800 cm^{-1} consisting of *D* and *G* bands. Figure 3.7 shows the Raman spectra of some selected depositional kerogen features from Sample A. The laser was focused in the center of the enclosed red box on selected features. The Raman spectra of two wispy depositional kerogen features (Figure 3.7) show very similar variation in the width and intensity of the *D*- and *G*-band bands. To compare, Figure 3.8 shows the Raman spectra of some selected MOM features of Sample A. Figure 3.9 shows the Raman spectra of selected depositional kerogen and migrated organic matter for Sample B. Table 3-2 lists the changes in the width of the *D*- and *G*- bands of the selected depositional kerogen and MOM in Samples A and B. The migrated OM show narrower *D* and *G* band widths compared to the depositional kerogen. As previously mentioned, the width of the *G*-band is found to be proportional to the bond-angle disorder at sp^2 sites and a narrow width indicates less degree of disorder. On the other hand, the narrowing of the *D* band is attributed to increase in aromatic clusters to form more ordered materials [63]. Thus, the migrated organic matter would be interpreted as close to the metagenesis stage, where a micro-porous solid is presumed to have formed by Behar [60].

Table 3-2: Raman parameters indicative of the degree of maturity of the two types of organic matter in Samples A and B, respectively

Types of OM	G-band (cm^{-1})	D-band (cm^{-1})	FWHM of G-band (cm^{-1})	FWHM of D-band (cm^{-1})
Depositional kerogen – 1 (Sample A)	1607	1348	55	157
Depositional kerogen – 2 (Sample A)	1606	1349	55	168
Depositional kerogen – 1 (Sample B)	1604	Not discernable	55	-
MOM – 1 (Sample A)	1600	1347	40	43
MOM – 3 (Sample A)	1608	1337	53	152
MOM – 1 (Sample B)	1605	1340	55	150

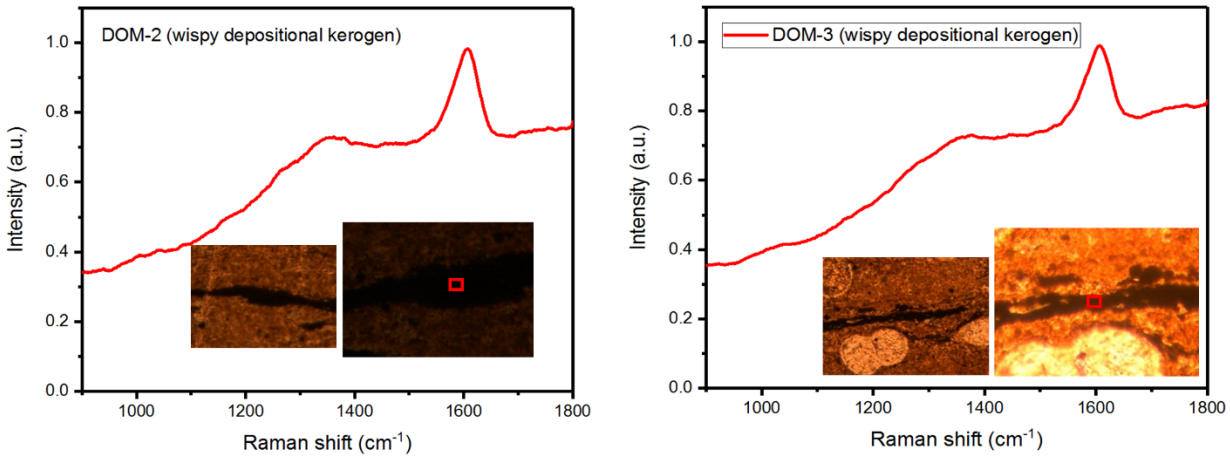

Figure 3.7: Selected depositional kerogen (DOM) for Sample A before gas exposure. Images of the kerogen use 50x & 100x, respectively; laser is focused in the center of red box on 100x images. Images are with reflected light. Horizontal width of red box is ~10 microns

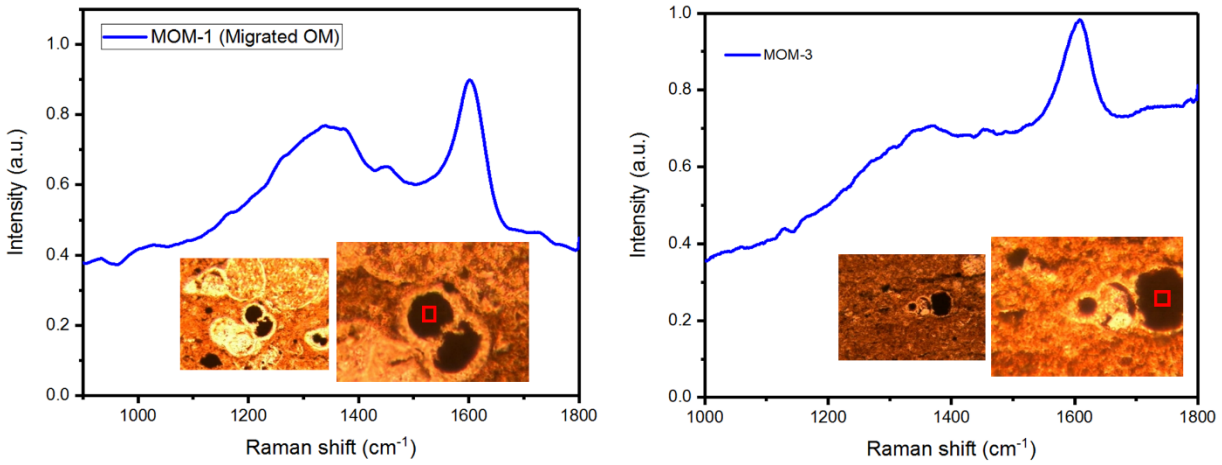

Figure 3.8: Selected migrated organic matter (MOM) in foram chambers for Sample A. Images of the migrated OM are taken with 50x and 100x objectives; Images are with reflected light. Laser is focused in the center of red box on 100x images. Width of red box is ~10 microns.

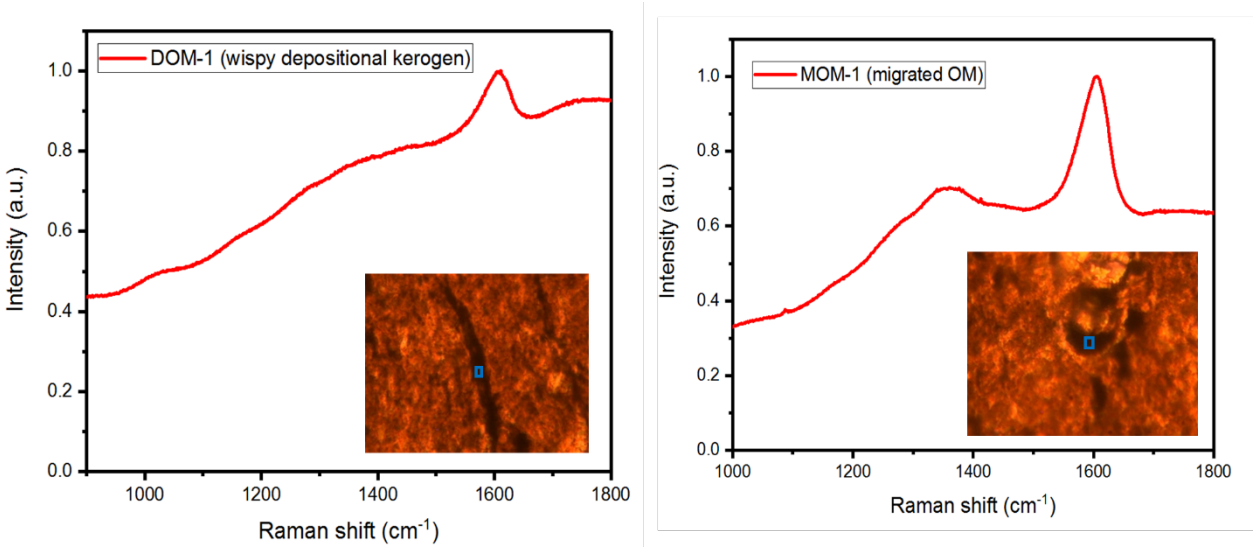

Figure 3.9: Selected depositional kerogen (DOM) and migrated OM (MOM) for Sample B. Images of the DOM are with 100x objective; Images are with reflected light; laser is focused in the center of blue box. Width of box is ~10 microns.

3.3.3 Gilsonite Raman Measurements

Gilsonite is a form of migrated solid bitumen believed to be sourced from the Green River Formation in the Uinta Basin, Utah. It is found, injected into vein systems well above the Green River and in areas where the Green River is thermally immature. It could have been generated in

more thermally mature areas and then migrated into shallow areas, or it could have been generated in immature areas of the Green River [82]. Either way, the Gilsonite is a good model for MOM that has not experienced a significant period of thermal maturation after its injection into pore space. As shown in Figure 3.10, the Raman measurements acquired for the Gilsonite sample showed no discernable Raman bands, due to the fluorescence of C-H bonds. The *D* and *G* bands apparent in the Eagle Ford MOM are not apparent in the Gilsonite.

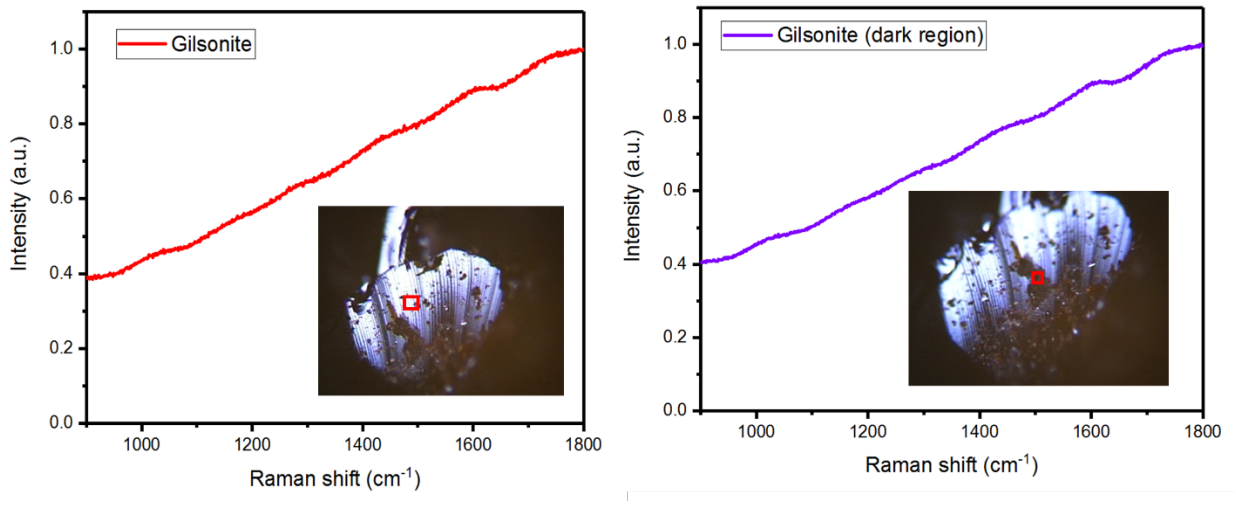

Figure 3.10: Raman spectra of Gilsonite from the Uinta Basin, Utah; width of red box ~10 microns

3.3.4 Discussion of Eagle Ford and Gilsonite Raman Data

In the Eagle Ford samples, depositional organic matter is expected to show signatures of thermal maturity consistent with the measured R_o of about 1%. Indeed the depositional kerogen in the samples show a *G* -band width of 55 cm^{-1} and *D*-band width as high as 168 cm^{-1}. Only the width of the *D* and *G* bands were considered as maturity-related measures due to less pronounced *D*-band intensities associated with some of the selected features in the LEF shale samples.

In comparison, it would be expected that the MOM would show signs of less thermal maturity. That is because the MOM filled pore space at a late stage in the diagenetic history of the rock, filling pore space after precipitation of calcite, pyrite, quartz, and kaolinite, and after formation of compactional micro-fractures. Thus, after emplacement, MOM would have spent less time at depth than depositional kerogen and should show signs of less maturity.

It is also reasonable to consider that it is possible that the Eagle Ford MOM originally had the *D* and *G* bands when it was emplaced, before it continued to be heated at depth. This can be disproven, however, if the Gilsonite is a model for what a Raman signature could look like in migrated solid OM before it is heated and altered. Clearly, the Gilsonite lacks the *D* and *G* bands apparent in the Eagle Ford OM. This suggests that the Eagle Ford migrated OM did not have the structure that would yield *D* and *G* bands when it was emplaced, and that it developed the *D* and *G* bands after emplacement through continued thermal maturation of the bitumen from heating after emplacement.

So, considering that the Eagle Ford organic matter *D* and *G* band response developed during thermal maturation of both depositional kerogen and MOM, one would still expect the MOM to show less thermal maturity than the depositional kerogen, because of its late emplacement. *G* band width as low as 40 cm^{-1} is observed in some selected MOM features with a narrower *D*-band width in the range of 43 – 152 cm^{-1} in all the selected MOM features. This Raman data would normally lead to an interpretation that the MOM has been subjected to a greater time at temperature than the depositional kerogen. As it is known that this is not the case based on the petrography, this observation clearly shows that the chemistry of the organic matter makes a difference in development of Raman spectroscopic thermal maturity indicators.

3.3.5 Raman Measurements after Gas Exposure

In addition, this study contributes to an understanding of mobility of hydrocarbons during a hydrocarbon gas huff-n-puff project. Huff-n-puff is implemented in shale oil reservoirs to improve recovery from horizontal wells with multi-stage hydraulic fracturing. It involves the injection of hydrocarbon gas and allowing enough time (soaking) to permeate through the fracture network and eventually the matrix in order to interact with the oil. The gas-oil interaction causes a reduction in the oil viscosity and interfacial tension (IFT) with increased oil volume due to swelling. In this study, we observe the hydrocarbon gas interaction with both the depositional kerogen and the migrated OM and detect changes with Raman.

Both first- and second-order regions were considered in the Raman measurements after exposing the sample to hydrocarbon gas composed mainly of methane (CH_4). This was carried out in an attempt to capture methane-related bands at ~ 2960 cm^{-1} and to evaluate changes in the depositional kerogen and MOM. Efforts were made to select the same spot as in the previous measurement (before gas exposure). Figure 3.11 shows the first-order Raman spectra of the depositional kerogen of Sample A after gas exposure. No significant changes were observed in the Raman spectra of both wispy depositional kerogen features from the gas exposure. On the other hand, Figure 3.12 shows the Raman spectra and corresponding images of selected MOM of Sample A after gas exposure. Unlike the depositional kerogen, almost all the MOM features were affected by gas exposure revealing pyrite framboids, otherwise covered by MOM within the forams. The presence of pyrite bands were observed to occur between 380 and 400 cm^{-1}. It is interpreted that the hydrocarbon gas allowed for displacement of a portion of the MOM/bitumen (loosely bound C-H bonds) to reveal minerals once obscured by bitumen/solid bitumen. The exposed samples showed no signs of the presence of methane in the Raman spectra.

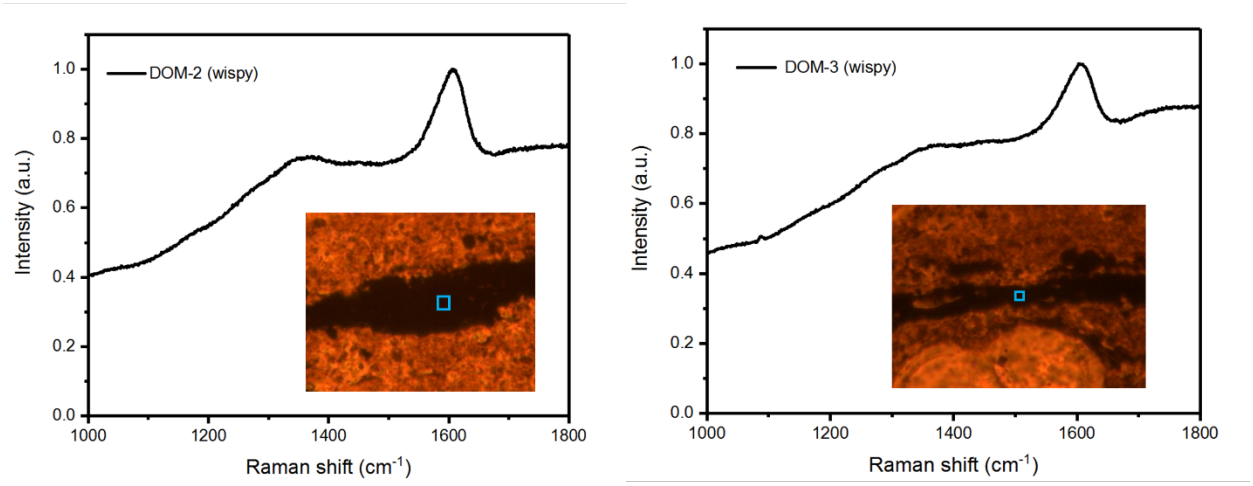

Figure 3.11: Selected depositional kerogen (DOM) of Sample A after gas exposure. Images are with reflected light; width of blue box is ~10 microns

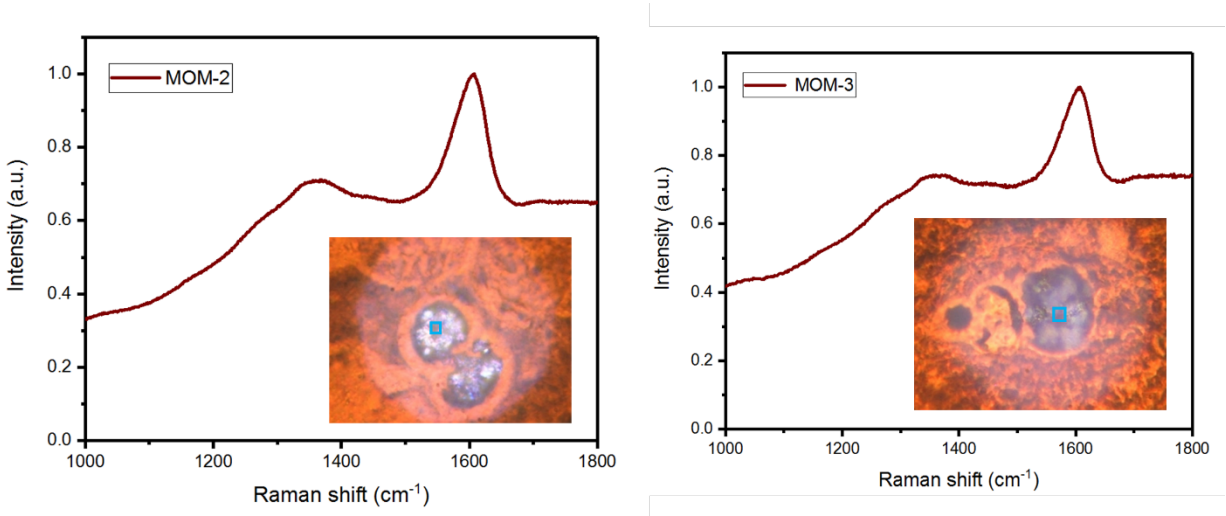

Figure 3.12: Selected MOM of Sample A after gas exposure. Images are with reflected light; width of blue box is ~10 microns

3.4 Conclusions

- This work improves understanding of compositional controls in sp^2 carbons like kerogen and the use of Raman spectroscopy for thermal maturity measurements. It was found that the original maceral composition plays a significant role in development of indicators of thermal maturity.

- The MOM filled pore space late in the paragenesis of the rock, well after burial and precipitation of diagenetic minerals, yet its Raman signature would incorrectly be interpreted as yielding higher maturity than the depositional kerogen, that was known to have had a longer time at high temperature.
- The fact that MOM shows Raman signatures indicating higher maturity can only be explained by Raman thermal maturity measures being dependent on original maceral chemistry. Apparently, the migrated OM was more prone to the development of the *D*-*G* band maturity signatures than the depositional kerogen.
- Raman analysis of Gilsonite shows that when the MOM was first emplaced, it had no Raman signature of maturity. The characteristic *D* and *G* Raman bands, indicative of thermal maturity were developed after the organic matter migrated into pores. This indicates that MOM developed thermal maturity after emplacement, and this is consistent with the high porosity developed in the MOM. It is a signature of thermal maturation of bitumen after its emplacement.
- The FWHM was used as a measure of thermal maturity among the LEF shale samples due to the low intensity of the *D*-band in some selected features. Raman parameters such as the *D*-*G* separation and the intensity ratio are more effective when the intensities of the *D* and *G* bands are very well defined.
- Hydrocarbon gas huff-n-puff experiments are observed to displace a portion of the MOM (bitumen) to reveal once obscured pyrite framboids, which pre-date the MOM.

Publication:

Cudjoe, S., Barati, R., Marshall, C., Goldstein, R., Tsau, J.-S., Nicoud, B., . . . Mohrbacher, D. (2019). Application of Raman Spectroscopy in Investigating the Effect of Source and Temperature on the Maturity of the Organic Matter Exposed to Hydrocarbon Gas Injection. *Unconventional Resources Technology Conference.* Denver.

4 CHAPTER 4: NUCLEAR MAGNETIC RESONANCE MEASUREMENTS (NMR)

Shale oil formations are distinguished by the presence of kerogen and generated hydrocarbons (light oil & bitumen) occupying the organic and inorganic pores. This makes petrophysical measurements using conventional techniques very challenging. Moreover, implementing hydrocarbon gas huff-n-puff in shale oil formations as an improved oil recovery (IOR) method, although effective, creates a more complex system, where the underlying in-situ interactions are not fully understood. NMR measurements can predict fluid types occupying different pore sizes in a formation. As such, performing gas huff-n-puff in the laboratory on core plugs and at the pilot scale in the formations can benefit from a non-destructive saturation measurement. This can be used for the estimation of incremental oil recovery based on the initial-oil-in-place (OIP).

This chapter utilizes low field nuclear magnetic resonance (NMR) relaxation measurements correlated with core analysis to estimate porosity, permeability and oil saturation properties of the Lower Eagle Ford (LEF) shale samples in the black-oil window and outlines the in-situ rock-fluid interactions during the IOR process.

4.1 Introduction

The rock fabric of the LEF shale samples within the oil window is found through pore-scale analysis to be dominated by carbonate and detrital clay with a mix of quartz, kaolinite, and pyrite, as well as isolated patches of organic matter (OM), which contribute to organic porosity [77]. A significant portion of oil is found in the nanopores of the isolated patches of organic matter, in addition to the micro-fractures and micro-pores within the rock matrix. Primary recovery from shale oil reservoirs involves multi-stage hydraulic fractures along horizontally placed wells to

create additional conduits within the ultra-tight matrix for flow. An ideal fracture network within a stimulated reservoir volume (SRV) would be expected to communicate with the organic porosity, which is not often the case since the fracture network is only contacting a small percentage of the pores. In so doing, increased oil production is observed at the initial production followed by a sharp decline due to drainage of all easily accessible oil within the fracture system and some micro-pores within the matrix leaving a greater portion of oil within the inaccessible organic (intraparticle) pores and interparticle pores.

Gas huff-n-puff is implemented as an improved recovery method to target the inaccessible oil within the organic pores as well as micro-pores within the matrix. An injected gas is observed to first move rapidly into the fractures and diffuses into a section of the matrix including both organic and inorganic pores at the fracture/ matrix interface. As the injected gas permeates the rock through a pressure gradient and diffusion, the interaction of gas with oil causes oil swelling, reduced oil viscosity and interfacial tension (IFT). Other controlling factors aid in extracting some components of the oil out of the pores and into the gas saturated fractures for production via diffusion [83, 84]. Evaluating the huff-n-puff recovery process in shales require *in-situ* knowledge of the types of pores (organic and/ or inorganic) invaded by gas, the extent of invasion, in addition to the composition and amount of remaining fluids at each injection and production cycle.

NMR refers to the response of the nucleus of the hydrogen atom to magnetic fields; hydrogen is abundant in both water, hydrocarbons, bitumen and organic matter (kerogen). Magnetic interactions between hydrogen protons result in longitudinal (T_1) and transverse (T_2) relaxations. T_1 relaxation occurs when protons have a precession around a static magnetic field ($\mathbf{B_0}$) resulting in the transfer of energy to its surroundings in a lower-energy state. Whereas, T_2 relaxation occurs by applying an oscillating magnetic field ($\mathbf{B_1}$) to the polarized protons, which eventually results in

dephasing of the protons without a transfer of energy. The T_2 relaxation is faster than T_1 relaxation and the application of NMR in reservoir rocks is dependent on the bulk fluid processes (affects both T_1 & T_2), surface relaxation (fluid-pore wall interface), and diffusion (affects only T_2) in the presence of a magnetic gradient [85]. Applying this technique, petrophysical properties such as porosity, pore-size distribution, saturation, and permeability can be extracted from NMR relaxation measurements.

Notwithstanding, NMR application in shales is more challenging than in conventional reservoir rocks as it presents different signals for organic and inorganic pores in addition to fluid types in either organic or inorganic pores. Daigle et *al*. [86] applied NMR relaxation measurements ($T_1 - T_2$ maps) to differentiate between organic and inorganic porosity in shales. It was assumed that bulk relaxations are contributions from inter-molecular and intra-molecular dipolar coupling, while surface relaxation is attributed to the interaction with paramagnetic ions on pore walls; diffusion relaxation is due to internal field gradients. Some recent NMR works focus on distinguishing and separating reservoir fluids in either organic or inorganic pores in addition to estimating hydrocarbon saturation based on 2D $T_1 - T_2$ NMR maps including, Fluery [87], Nicot [88] and Kausik et *al*. [89]. Furthermore, Rylander et *al*. [90] and Veselinovic et *al*. [91] applied T_2 - NMR measurements to determine the distribution of pores and natural fracture porosity in shales, respectively. Valori et *al*. [92] applied 2D $T_1 - T_2$ NMR maps to measure permeability and porosity of shales by continuously measuring NMR signals of fully saturated shale cores with methane.

NMR application in improved gas recovery in organic-rich shales is very limited and recent work made use of synthetic oil and crushed shale samples [93], which may not be representative of the rock-fluid interactions in shales. This work makes use of three LEF reservoir cores from

different lithofacies in addition to an Eagle Ford Outcrop core to (1) evaluate hydrocarbon gas huff-n-puff recovery; (2) determine fluid typing in heterogeneous pores after recovery; and (3) to estimate petrophysical properties such as porosity, pore size distribution, permeability, and hydrocarbon saturation in the process.

4.2 Methods

4.2.1 Samples

Three LEF shale reservoir cores from different lithofacies and one Eagle Ford Outcrop sample were used in this study. The dimension of the core plugs measured 3 inches in length and 1 inch in diameter. The mineral composition of each sample from X-ray diffraction (XRD) analysis in weight percent (*wt. %*) is listed in previous work by Cudjoe et al. [77]. Sample A is observed to be rich in calcite, while the lithology of Sample B is found to be slightly argillaceous siliceous marlstone, and Sample C has high content of clay minerals. The presence of micro-fractures (~ 4μm) and organic pores ranging from 14 nm to 500 nm have been observed in all three (3) LEF shale samples using scanning electron microscopy (SEM) and focused ion beam – scanning electron microscopy (FIB-SEM) imaging techniques [94].

Table 4-1 shows tight rock analysis (TRA), Leco TOC measurements, and Rock-Eval pyrolysis data of the three samples. All three samples are within the oil window (0.98 – 1.03 VR_o %) with substantial TOC content between 5.06 – 5.75 *wt. %*. Sample B has the highest porosity (7.2 % BV) but the least permeability (0.001332 mD) from pulse-decay (PD) measurements. Sample C has the highest water saturation of about 5 times that of Samples A and B (Table 4-1). Additional Rock-Eval pyrolysis data reported in our previous work show both S_1 and S_2 data for Sample A and Sample B to be greater than that of Sample C, indicating higher quantity of free hydrocarbons and potential hydrocarbon to be generated during pyrolysis. The Eagle Ford Outcrop

has a porosity of 6% based on pulse decay measurement and pore volume of 2.21 cc. NMR measurements were performed on the as-received states of both the reservoir cores and the Outcrop core. Presence of hydrocarbons and bound fluids are expected in the "as-received" reservoir cores.

Table 4-1.Tight rock analysis (TRA), Leco TOC, and Rock-Eval pyrolysis data for the LEF samples

LEF Samples	TOC (*wt. %*)	VR_o (%)	PD permeability (mD)	PD porosity (% of BV)	Water saturation (% of PV)
A	5.75	0.98	0.001752	6.9	1.2
B	5.06	1.01	0.001332	7.2	1.2
C	5.29	1.03	0.001978	6.5	6.4

4.2.2 Saturating Samples with Oil and Hexadecane

Prior to saturating with fluids, the core samples were first weighed and dried at a temperature of 90°C until a constant weight was reached. Both reservoir core plugs and Outcrop core were placed one at a time in a cell with an annulus space between the inside of the cell and each cylindrical core. This annulus is representative of the fracture surrounding a core matrix. Crude oil samples were obtained from the Eagle Ford formation with a density of 0.797 g/cm^3 described as light oil with lower amounts of resins and asphaltenes, which makes it favorable for huff-n-puff improved recovery. The density of hexadecane is 0.772 g/cm^3 at room temperature. Figure 4.1 shows the experimental set-up for saturating the cores (both reservoir cores and Outcrop) at different pressures (3000 or 3500) psi and different temperatures (40°C and 125°C). An Isco pump is used to pressurize the cell with either oil or hexadecane (HD) for reservoir cores and Outcrop core, respectively, after the core plug was vacuumed. When the set temperature is reached at equilibrium, the cell is kept under the applied pressure and temperature for 3 days. The cell is then

depressurized to ambient pressure and room temperature to remove the core for NMR measurements. Samples are weighed after each saturation stage for mass balance estimations.

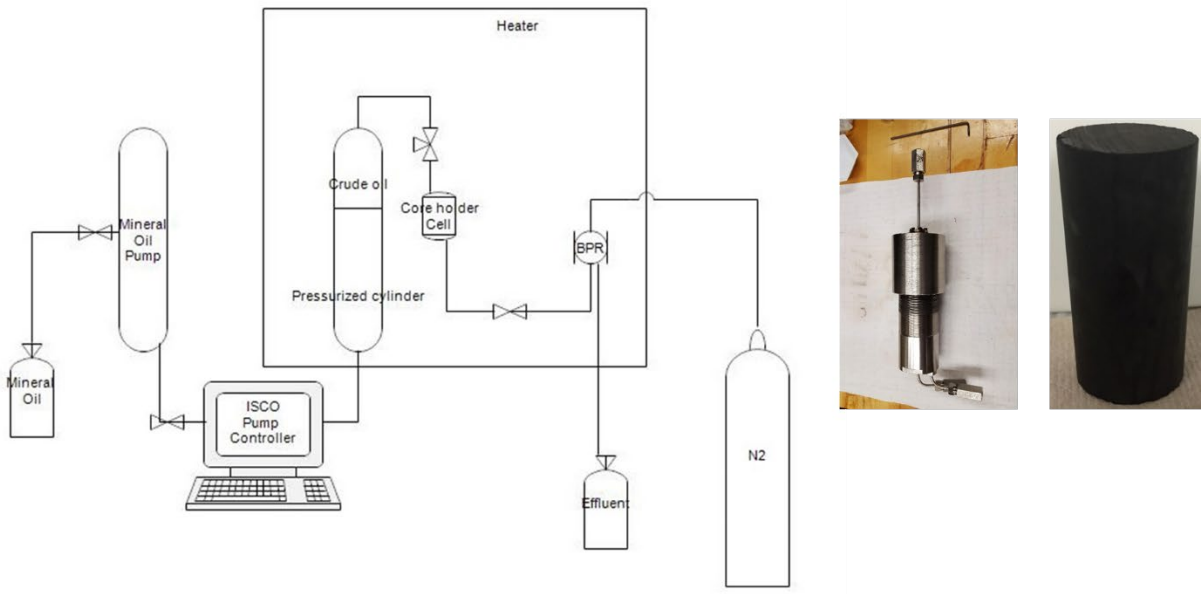

Figure 4.1: Schematic diagram of the saturation process; both the core holder cell and a reservoir core plug are presented on the right

4.2.3 Hydrocarbon Gas Huff-n-Puff

The "saturated" core plug placed in the cell was saturated with oil again for another 24 hours at reservoir condition prior to the huff-n-puff experiment. During the test, each cycle of huff-n-puff consists of hydrocarbon gas injection at 3500 psi, soaking for 24 hours, then producing with the pressure reduced to 1000 psi in a linear manner over a period of time. Three cycles of huff-n-puff were performed on the Eagle Ford Outcrop, while the reservoir cores underwent 6 cycles of huff-n-puff. The extracted oil phase and gas phase from the core matrix in each cycle were collected and analyzed with the gas chromatography. At the end of each test, the cell was depressurized to ambient pressure and room temperature to remove the core for NMR

measurements; once again the core samples were weighed after the huff-n-puff recovery for mass balance estimation.

4.2.4 NMR Relaxation Measurements

NMR relaxation measurements were acquired using a benchtop Magritek NMR Core Analyzer with operating frequency of 2.0 MHz set at room temperature. Longitudinal (T_1) and transverse (T_2) relaxation time distributions were measured with inversion recovery free induction decay (IRFID) [95] and Carr, Purcell, Meiboom and Gill (CMPG) [96] pulse sequences, respectively. In addition, 2D T_1-T_2 maps were acquired using magnetic resonance imaging techniques. NMR measurements were conducted on bulk Eagle Ford oil and hexadecane samples at 3 cc, 2 cc, and 1 cc, for calibration purposes. NMR T_2 distributions were measured using 100 µs echo spacing (TE), 2000 – 15000 ms polarization time, 300 signal to noise ratio (SNR), and 2000 number of echoes. The T_1 distributions were measured with logarithmically spaced delay time from 1 to 5000 ms. Both IRFID and CMPG raw data were inverted with Laplace non-negative least square fitting [97] to produce the T_1 and T_2 distributions, respectively and the smoothing parameter is determined according to Dunn's methodology [98]. Figure 4.2 shows a flowchart of the NMR measurements from as-received cores to after huff-n-puff recovery.

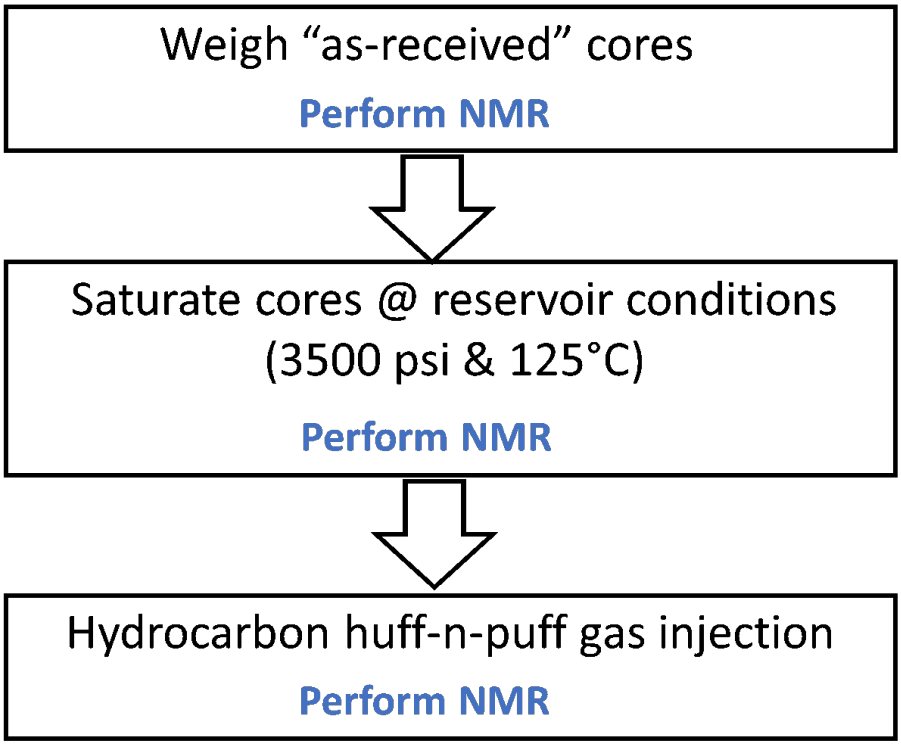

Figure 4.2: Flowchart of NMR measurements on the LEF reservoir cores and the Eagle Ford Outcrop core, respectively.

4.3 Results & Discussion

4.3.1 NMR Measurements of As-Received & Saturated Conditions

In the as-received state, the reservoir core samples are presumed to have bound fluids (water and bitumen) with some amount of mobile hydrocarbons within the organic pores and some mixed-wet inorganic pores and/fractures. Prior knowledge of the LEF reservoir cores show substantial organic content as seen in Table 4-1 with organic porosity varying from 2.1% for Sample A, 1.7% for Sample B, and 0.87% for Samples C, through FIB-SEM analysis. Moreover, the segmented pores of Sample B possess a higher surface area of 164.5 μm^2 than Sample A and Sample C with surface area of 102.4 μm^2 and 64.9 μm^2, respectively. A high surface area contributes significantly to adsorption of gas molecules and diffusion for improved recovery [94]. It is also worth pointing

out that pore-scale analysis shows Sample B to have ~30% of its organic pores to be relatively large and interconnected compared to relatively spherical and isolated organic pores in Sample A and Sample C, respectively [77].

The T_2 NMR distribution in Figure 4.3 shows different peaks at different conditions for the reservoir cores and the Outcrop core, which is indicative of oil and hexadecane in different pores. Previous work by Kausik et *al*. [89] and Mehana [99] reported T_2 cutoff values at different saturation conditions in a LEF shale sample performed at 2 MHz, which was adapted to interpret the NMR results in this work. The T_2 cutoff of oil in the organic pores is reported in the range of 1 – 10 ms, while the T_2 cutoff for oil in inorganic pores is > 10 ms. The bound fluids (bitumen and clay bound water) are reported to be < 1.5 ms listed in Table 4-2. In our adaptations, the cutoff values were picked at the valleys or inflection points of the T_2 distributions as listed in Table 4-2 ; the bound fluids region is set at T_2 < 1 ms, the organic pores saturated with oil are set at T_2 = 1 – 16 ms, and the inorganic pores with oil/hexadecane are set at T_2 > 16 ms.

Table 4-2: T_2 cutoff values at the inflection points of the T_2 distributions for the LEF samples and other works [89, 99]

	Bound region (BR)	**Organic pores (OP)**	**Inorganic pores (IP)**
T_2 (ms)	<1	1 – 16	> 16
T_2 (ms) [89, 99]	<1.5	1 – 10	> 10

Two separate intense signals in the bound region (BR) and organic pores (OP) are observed in the NMR T_2 distribution of Sample A in the as-received state with a minor signal in the inorganic pores (IP). This is indicative of significant bound fluids (water and bitumen) and movable hydrocarbons in the organic pores before saturation. However, after saturating with reservoir oil,

the amplitude of the T_2 peak in the OP increases to indicate its affinity to imbibe the injected oil relative to the IP at both pressures and temperatures. The T_2 peak representing the BR decreases in amplitude with a slight shift to the right at saturation temperatures when compared to the as-received state to indicate some bound fluids (mainly bitumen) were rendered mobile with temperature. In addition, some inorganic pores within the matrix are also seen to slightly increase in amplitude. Minor amplitude peaks at longer T_2 (> 100 ms) is interpreted as micro-fractures; micro-fractures were indeed observed in the SEM/BSE images of the reservoir samples [77].

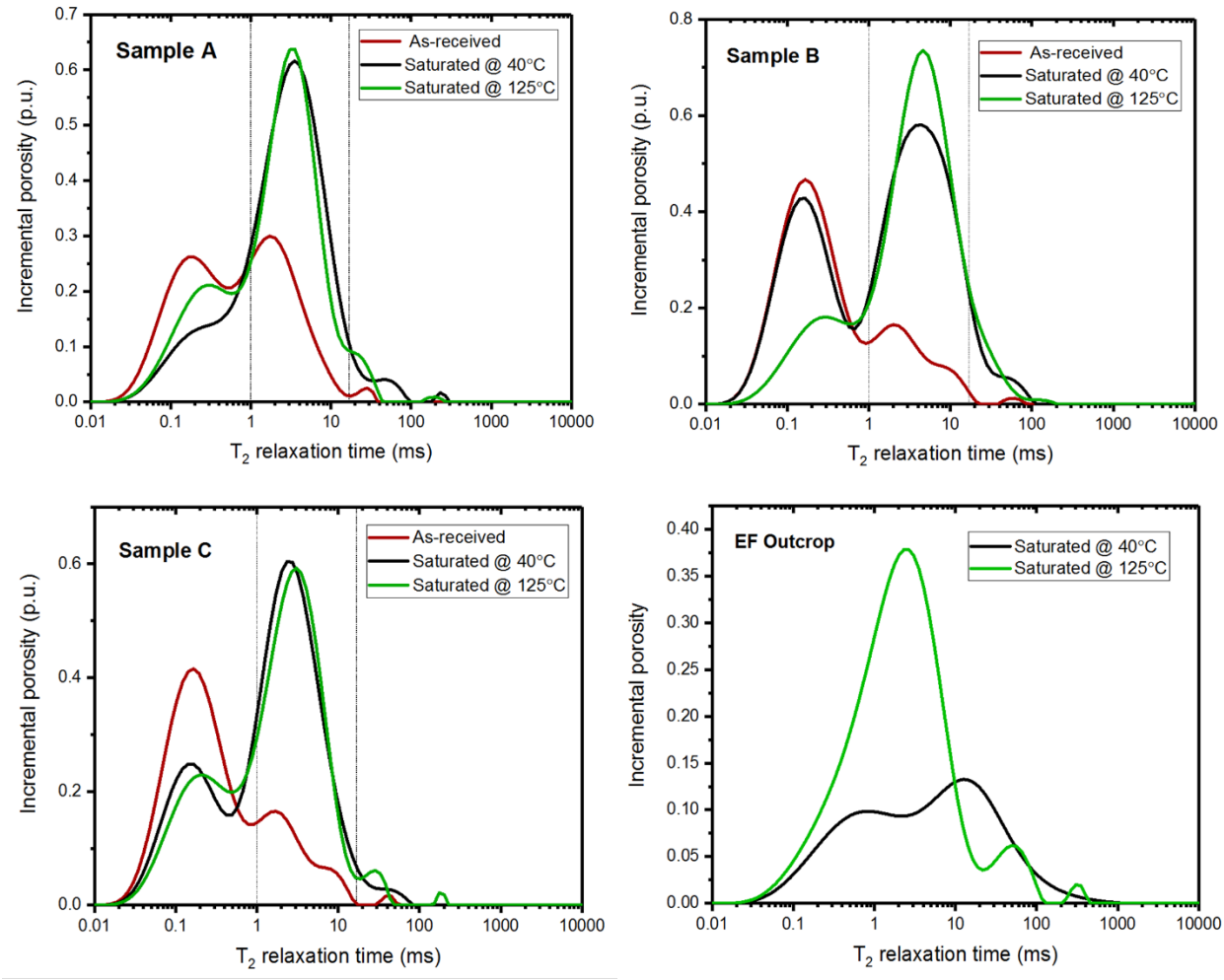

Figure 4.3: T_2 NMR relaxation measurements of the LEF reservoir cores and the EF Outcrop in the "as-received" and "saturated" conditions

Both Sample B and Sample C show similar T_2 distributions in the as-received state but with different peak amplitudes (Figure 4.3– top right and bottom left, respectively). The as-received states of Samples B and C, respectively, show an intense signal related to the BR with other accompanying minor peaks assigned to the OP and IP or fractures. Once again, introducing oil resulted in an increase in amplitude of the signal within the organic pore region (oil-wetting) with substantial decrease of T_2 amplitude in the bound fluid region at the different saturating temperatures and pressures.

On the other hand, the Eagle Ford (EF) Outcrop clearly shows a bi-modal peak at 3000 psi and 40°C saturation with hexadecane (Figure 4.3– bottom right). The adapted T_2 cutoff values are adjusted for the EF Outcrop since the organic pore region is not as distinct as observed in the reservoir cores. The bi-modal peak at 3000 psi and 40°C saturation shows the bound fluid region to be $T_2 < 2.5$ ms and the overlapped region of both organic and inorganic pores to be $T_2 = 2.5 –$ 1000 ms. Though, the Outcrop core might not be as organic-rich as the reservoir cores, it shows signals pertaining to an organic pore region. Figure 4.4 shows the presence of migrated organic matter (MOM) in the chambers of foraminifer fossils for an EF Outcrop core. Organic pores are not as developed in the MOM of the Outcrop core as observed in the reservoir cores but are present nonetheless. Upon saturating at reservoir conditions of 3500 psi and 125°C, an intense peak is observed at $T_2 < 23$ ms with accompanying minor peaks at $T_2 = 23 – 150$ ms, and $T_2 > 150$ ms, respectively. It can be observed that the temperature effect did not cause the peak pertaining to the bound fluids to decrease as it did in the reservoir cores; saturating at reservoir conditions caused an increase in amplitude within the overlapped bound and organic pore regions. The mere confinement of hexadecane in the smaller pores of the Outcrop could also be the reason for the increased amplitude.

The presence of bound fluids like bitumen is corroborated by our pore-scale analysis, where most bitumen features were observed on SEM/BSE images infilling primary porosity of foraminifera chambers and within inter-particle pores of the matrix for the LEF reservoir cores. Moreover, exposing the rock chips to hydrocarbon gas saw the displacement of some of these bitumen features within the matrix [94, 100].

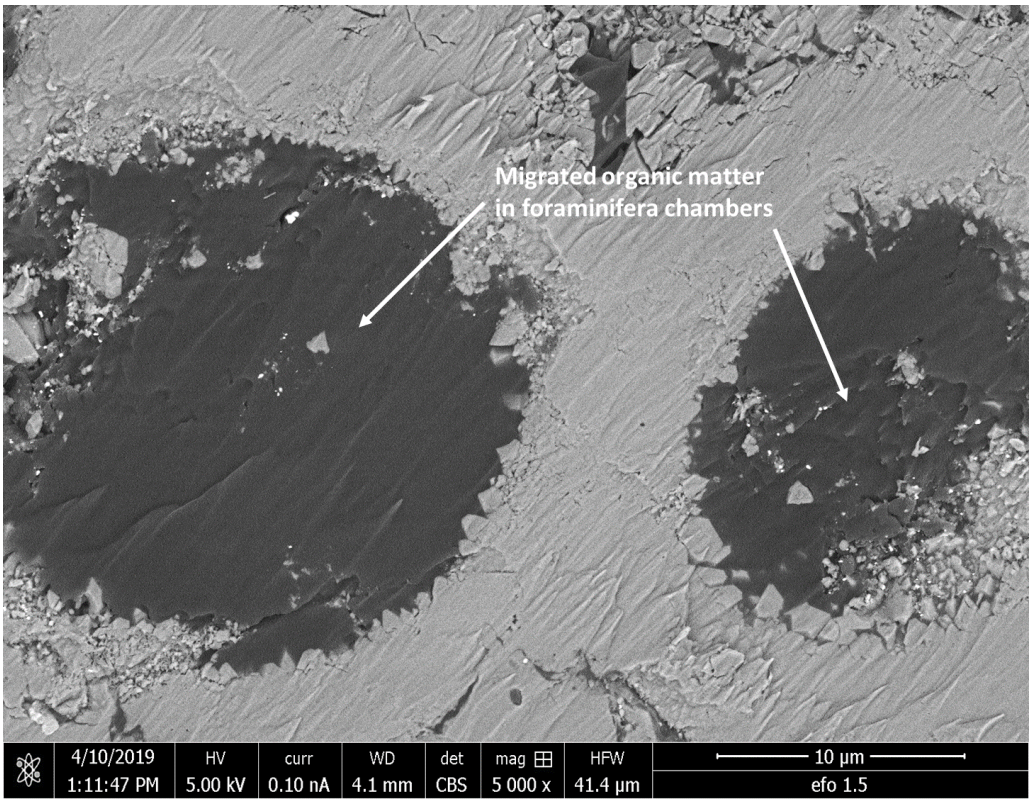

Figure 4.4: BSE image of an Eagle Ford Outcrop showing the presences of MOM in carbonate microfossils

4.3.2 NMR Measurements after Huff-n-Puff Recovery

Light hydrocarbons are recovered together with gas components after each cycle of huff-n-puff as observed in our gas chromatography analysis of the produced hydrocarbon/affluent [101]. Figure 4.5 shows the T_2 distributions of saturated and huff-n-puff processes at reservoir conditions. The reservoir cores were subjected to six (6) cycles of huff-n-puff, while the Outcrop core was

subjected to three (3) cycles of huff-n-puff. A reduction in the T_2 amplitude is observed for all the samples when compared to the saturated amplitude at reservoir conditions (Figure 4.5), which signifies the recovery of mobile oil or hexadecane (HD) from the Eagle Ford samples.

Another observation is the shift of the $T_{2\ log\ mean}$ (T_{2LM}) values to the left as listed in Table 4-3 below. The T_{2LM} shift to the left is reported to be indicative of remaining heavier components as light - medium components are recovered after each cycle [93]. However, the remaining heavier components is not the only factor to cause the shift to the left with shorter T_2 relaxation time, since the Outcrop core is saturated with hexadecane (HD), a single component, which does not have any heavier components. Therefore, we hypothesize that some of the injected gas (methane) and/ or fluid percolated pores otherwise inaccessible (micro- and nano-pores) to the saturating oil to be confined and/ or adsorbed. The intra-particle pores observed in clay minerals in the SEM/BSE images of the LEF shale samples are mostly filled with migrated organic matter, which would explain the gas (methane) in the bound region ($T_2 < 1$ ms) of the samples. In addition, the organic matter (kerogen) and clay minerals present additional surface for fluid relaxation.

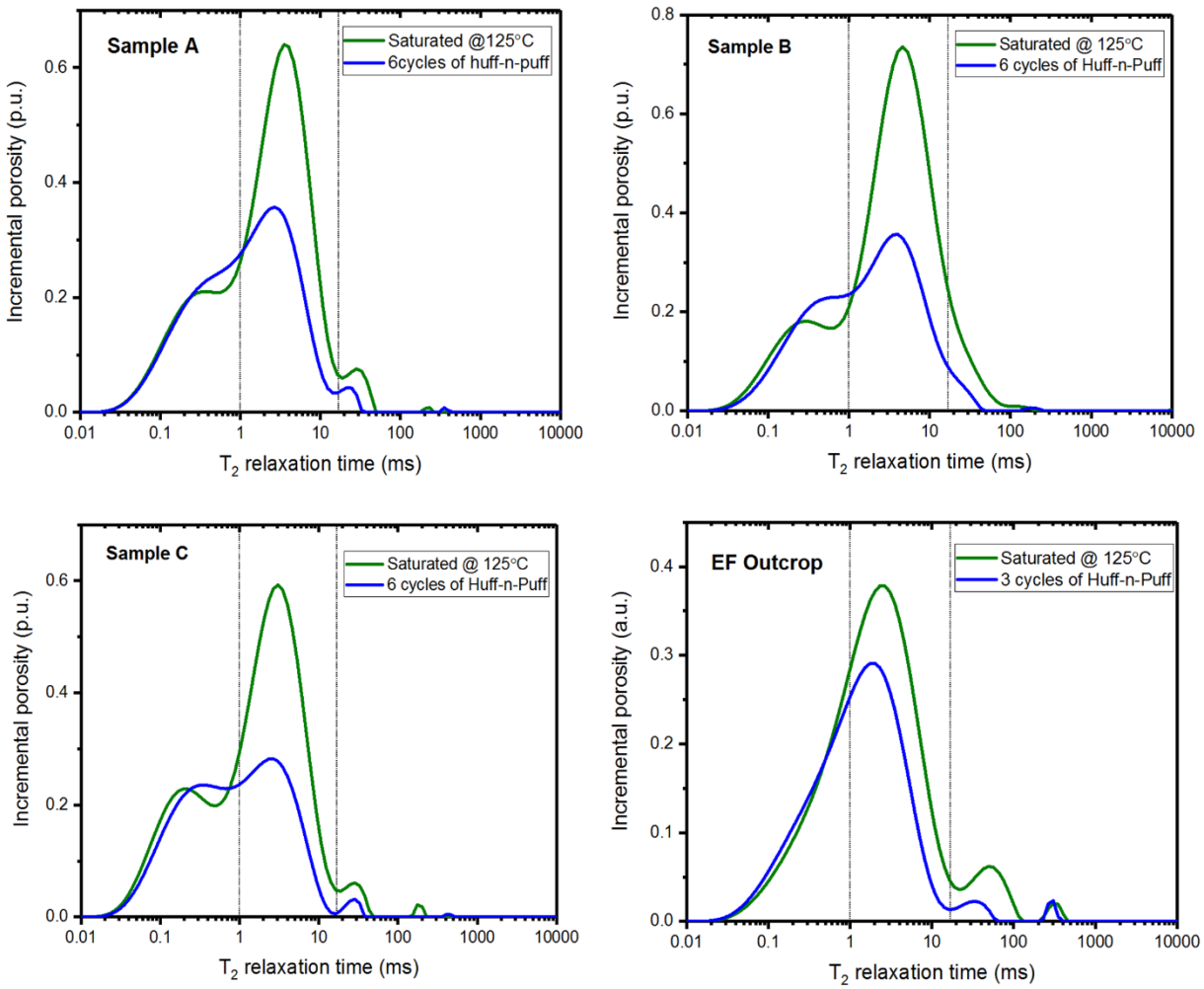

Figure 4.5: T_2 NMR distributions for LEF reservoir cores and Outcrop core after different cycles of gas huff-n-puff

Table 4-3: T_2 log mean shift to the left after hydrocarbon recovery through huff-n-puff gas injection

LEF Samples	T_{2LM} – saturated @ 125°C	T_{2LM} – after huff-n-puff
A	1.89	1.52
B	2.73	1.57
C	1.38	0.85
EF Outcrop	2.06	1.25

Table 4-4 enumerates the pore volume of each sample determined as a product of the bulk volume and the Tight Rock Analysis (TRA) porosity provided in Table 4-1. The volume imbibed is expressed below as the ratio of the mass change to the density of the saturating oil.

$$Vol_{imbibed} = \frac{(M_{saturated} - M_{as-received})}{\rho_{oil/HD}} \quad (4\text{-}1)$$

where, $Vol_{imbibed}$ is the volume of liquid (oil/HD) imbibed; $M_{saturated}$ is the mass of the saturated core; $M_{as-received}$ is the mass of the core in its dry or as-received state and $\rho_{oil/HD}$ is the density of oil/hexadecane

The remaining volume of liquid and the corresponding recovery percentage are also added to Table 4-4. Of the reservoir cores, Samples A and B show a close range of recovery (~57%) through mass balance estimation (MBE), while the Outcrop core shows a recovery of ~50%. Sample C presents a relatively lower recovery comparing to the other two reservoir samples.

Table 4-4: Mass balance estimation of oil/hexadecane recovered after huff-n-puff (courtesy of Dr. Tsau)

LEF Samples	Pore vol. (cc)	Vol. imbibed (cc)	Remaining vol. (cc)	Recovery (%) - MBE
A (oil)	2.62	2.18	0.93	57.52
B (oil)	2.73	2.46	1.06	56.71
C (oil)	2.45	2.09	1.01	51.74
Outcrop (HD)	2.21	1.86	0.93	49.90

4.3.3 NMR Saturation Estimation

Mass estimation of oil saturation as previously mentioned is unreliable for such small volumes or mass changes. Furthermore, laboratory handling of the cores before weight measurements may cause errors. The NMR T_2 distribution helps to estimate the amount of hydrocarbon recovered by integrating NMR signals attributed to oil and/or hexadecane in the

reservoir cores and/ or Outcrop, respectively. The difference between the integrated area under saturation at reservoir conditions and that of the remaining hydrocarbon after huff-n-puff, gives an estimation of the amount of oil/HD recovered (Area-Based). Table 4-5 shows the percentage of recovered oil and hexadecane in the reservoir cores and Outcrop, respectively. Sample B is observed to have the highest recovery of ~56 % from NMR saturation estimation; Sample B recorded a higher porosity than the other samples through pulse decay measurements as listed in Table 4-1. Moreover, pore-scale analysis shows that ~83% of the organic pores in Sample B are relatively larger in size than the other reservoir core samples with pore diameter ranging from 14 nm – 576 nm [77]. The results of the "Area-Based" NMR oil recovery are in close agreement with the "Mass-Balance" calculations reported in Table 4-4.

Table 4-5: NMR estimation of oil/HD recovered from the LEF reservoir cores and EF Outcrop, respectively

LEF Samples	Area under T_2 (saturation)	Area under T_2 (huff-n-puff)	NMR Recovery (%) (Area-Based)
A	5.34	2.55	52.30
B	11.70	5.19	55.61
C	4.49	2.28	49.21
Outcrop	7.36	3.81	48.17

4.3.4 NMR Pore Size Distribution

As previously mentioned, the rock fabric (matrix) of the LEF shale reservoir cores are dominated by calcite with a mix of quartz, clay minerals, and pyrite embedded with isolated patches of organic matter [77]. The matrix grains have different pore sizes with mixed-wet wettability, while the nanopores developed in the organic matter (kerogen) are considered oil-wet with adsorption capabilities. In conventional reservoirs, the NMR T_2 distribution of a fluid in a pore can be used to determine the pore size by assuming the main relaxation mechanism is surface

relaxation [85]. However, in shales the relaxation interaction scale is comparable to the scale of pores investigated through our FIB-SEM and SEM/BSE studies [77] and the heterogeneous pore spaces with different relaxivity measurements make NMR estimation of pore size using the relaxation governing equations in shales challenging.

Therefore, we simply determined the different pore systems by identifying inflection points between two adjacent T_2 peaks as carried out by Veselinovic [91]. From the T_2 distribution of the LEF reservoir cores and EF Outcrop saturated at reservoir conditions of 3500 psi and 125°C (Figure 4.3 & Figure 4.5), we identified micro-pores at $T_2 < 1$ ms, meso-pores at $T_2 \sim 1 – 16$ ms and macro-pores at $T_2 > 16$ ms. Pore systems with longer T_2 relaxation time ($T_2 > 100$ ms) are perceived to be likely fractures. FIB-SEM studies on the LEF shale reservoir cores showed the distribution of the organic and inorganic pores to range from 13 nm – 5 µm [77].

4.3.5 NMR Porosity

NMR cumulative porosity is determined by integrating the T_2 distributions of fluids for each reservoir/Outcrop core. Table 4-6 shows the NMR cumulative porosity before and after hydrocarbon gas huff-n-puff recovery for the LEF reservoir cores.

Table 4-6: NMR cumulative porosity for the LEF reservoir core samples before and after huff-n-puff

Samples	NMR porosity (%) (Saturated cores)	NMR porosity (%) (After huff-n-puff)
A	12.47	9.73
B	14.57	9.11
C	12.38	8.05

4.3.6 2D T_1-T_2 Maps for Fluid Typing in Different Pore Systems

Figure 4.6 shows the corresponding 2D T_1-T_2 maps of the LEF reservoir cores and the EF Outcrop core after hydrocarbon gas huff-n-puff. These maps are essential to determine the fluid type contained in the different pore systems after the huff-n-puff recovery process and to differentiate between moveable and non-movable fluids in the samples.

We observe T_1/T_2 ratio to be in the range of ~ 3.7 – 5 with T_2 distribution in the OP region for remaining oil and hexadecane (HD) in the reservoir cores and the EF Outcrop, at 2 MHz NMR measurements. Oil/HD presumed to be in the mixed-wet pore space show a T_1/T_2 ratio ~2 and occurs in the IP region, which matches the findings of Kausik et *al*. [89]. A significant portion of the oil/HD in these pores are diminished after the huff-n-puff process as they make up movable or producible hydrocarbon. In addition, the BR represents bound fluids (mostly bitumen and clay bound water) with T_1/T_2 ratio > 7. Hydroxyls from clay minerals are observed to overlap with the bitumen and kerogen signals in most NMR shale measurements [99]. Hydroxyls from clay are reported to occur between $0.01 < T_2 < 0.1$ ms T_2 distribution and $10 < T_1/T_2$ ratio < 100 with kerogen identified at $10 < T_1/T_2$ ratio < 100. Large T_1/T_2 ratios of 100 and above are reportedly attributed to more viscous fluids such as bitumen [62]. On the other hand, methane is reported to be separated at a T_1/T_2 ratio of ~ 10 [87] and Valori [92] observed methane gas stored in the bound region of Poseidonia shale samples (United Kingdom) at short T_2 relaxation time with high T_1/T_2 ratio.

With the above deductions and interpretations in mind, Sample A is observed to have a dominant peak in the OP region with a T_1/T_2 ratio of 3.8, inferred to be residual oil contained in the hydrocarbon-wetting pores. A secondary peak at a T_1/T_2 ratio of 9.5 in the BR is interpreted as methane confined/adsorbed in the bound region and organic pores after the huff-n-puff process.

The organic pore distribution from FIB-SEM analysis of the LEF shale samples vary from ~ 13 nm to 500 nm, which can easily be invaded by methane gas with a diameter of ~ 0.38 nm. As previously mentioned, the intraparticle pores within the clay minerals mostly kaolinite (hydrocarbon-wet) are filled with migrated organic matter, which would explain the possibility of gas adsorption in the bound region. Furthermore, adsorbed fluid signal is regarded to be controlled mainly by interactions with surface molecules, where a relatively faster relaxation will be recorded compared to the remaining fluids in the pores [99, 85]. The mixed-wet IPs with T_1/T_2 ratio of ~2 have the least dominant peak, which we interpret as produced oil due to the hydrocarbon recovery; this is observed in all the samples.

In a similar manner, Sample B has a dominant peak in the OP region with a T_1/T_2 ratio of 3.8, also inferred to be residual oil in the organic pores. A secondary peak at T_1/T_2 ratio ~15 in the BR is interpreted as methane confined/adsorbed in organic nanopores after the huff-n-puff recovery. Smudges of signals are observed at much higher T_1/T_2 ratio (> 100) at T_2 distribution < 0.1 ms, which could be attributed to hydroxyls from clay minerals or due to the inversion method used for the T_1-T_2 map. Moreover, Nicot [88] interpreted high T_1/T_2 ratio as simply the confinement of light oil in the organic pores.

On the other hand, Sample C shows two dominant peaks with T_2 distributions from 0.15 – 1 ms and in the OP region, respectively, in addition to a secondary peak at T_2 < 0.15 ms. The T_1/T_2 ratio of the first dominant peak (T_2 ~ 0.15 – 1 ms) is at ~8.6 interpreted as methane confined/adsorbed in the bound and organic pore region, while the T_1/T_2 ratio of the second dominant peak is at 4.5 inferred to be residual oil in the organic pores. A significant and clear signal observed at much higher T_1/T_2 ratio ~ 60 at T_2 distribution < 0.1 ms, is attributed to either

hydroxyls from clay minerals or contributions from absorbed fluids within the interlayers of the clay minerals.

The clay mineral content of the LEF shale samples from XRD analysis is observed to increase with greater depth as such Sample C has the highest clay mineral content (kaolinite = 5.3 wt. %, illite + mica + smectite = 13.9 wt. %) compared to the other reservoir samples and also has a higher structural clay bound water of 3.5 % of BV [77]. Illite (water-wet), kaolinite (hydrocarbon-wet), and smectite clay minerals present in the LEF shale samples affect the wettability of the pores leading to the absorption or adsorption of different fluids; smectite may absorb hydrocarbons under different conditions [102, 103].

The EF Outcrop shows a dominant peak at T_1/T_2 ratio of ~ 3.7 with T_2 distribution in the OP region inferred to be residual hexadecane in hydrocarbon-wetting pores. Hydroxyls from clay minerals or fluid confined in intra-particle pores of clay minerals show a secondary peak at T_1/T_2 ratio ~ 35 with $T_2 < 1$ ms.

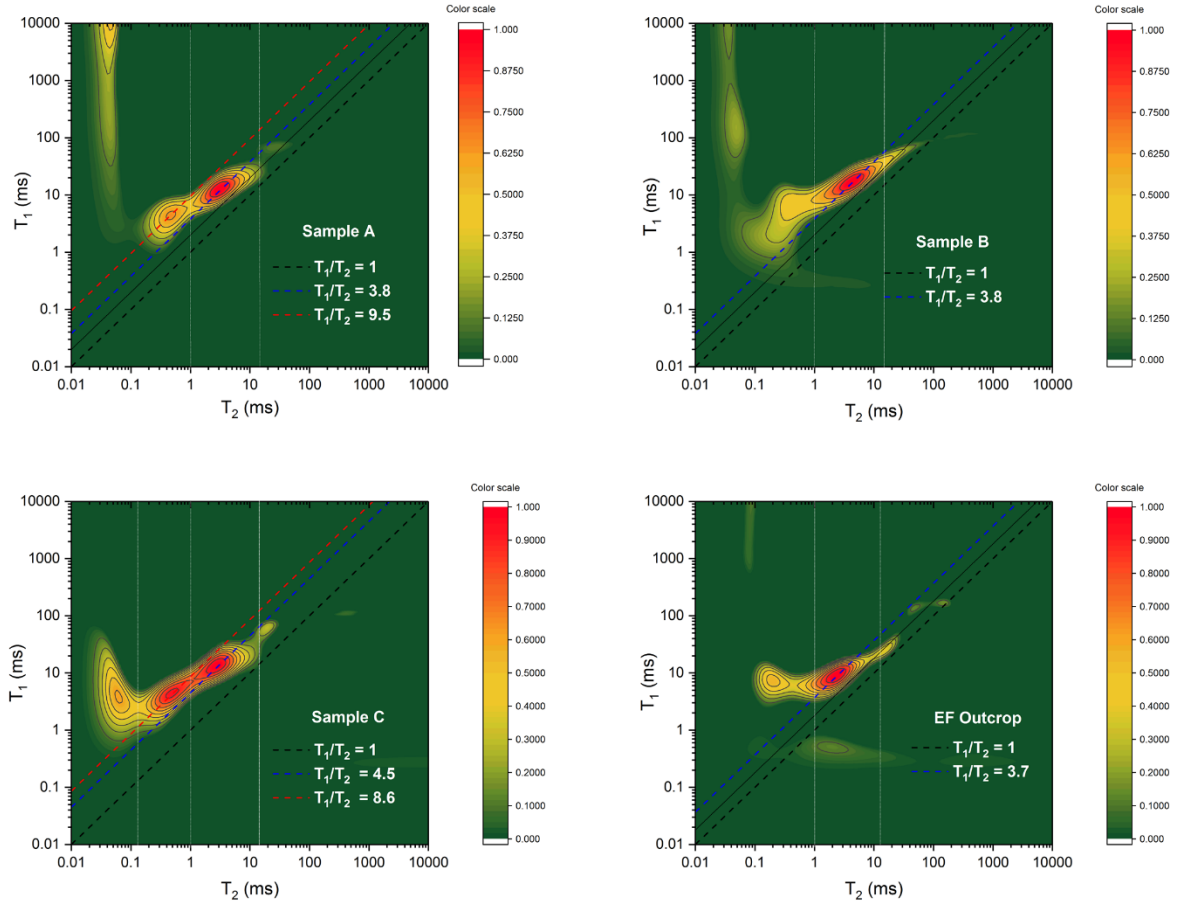

Figure 4.6: 2D T_1-T_2 maps of the LEF reservoir cores and EF Outcrop, respectively, after huff-n-puff recovery.

4.3.7 NMR Permeability

NMR permeability is based on theoretical models, which show permeability to increase with both increasing porosity and increasing pore size [85]. The Timur-Coates [104, 105] and the Schlumberger-Doll Research (SDR) [106] theoretical models are best suited for conventional reservoirs unlike shale reservoirs with multi-component grains and heterogeneous pore space. The SDR equation is expressed as

$$k = A\varphi^4 T_{2LM}^2 \tag{4-2}$$

where, k is permeability (m^2); A is an empirical coefficient (m^2/s^2); φ is porosity (fraction) and T_{2LM} is the geometric mean of the transverse (T_2) relaxation time (s).

However, an improved version of the Schlumberger-Doll Research (SDR) equation is presented where the porosity, grain size, specific surface, and intrinsic property of the varying mineral grains are incorporated for a more accurate permeability estimation in shale reservoir [107]. This was carried out by comparing the SDR model to a modified form of Kozeny-Carman permeability model [108, 109] since both models relate permeability to pore geometry and surface area of the porous medium. As a result, the empirical coefficient (A) is expressed as [107]

$$A = \frac{\rho_2^2}{\varphi^3 \beta \tau^2} \tag{4-3}$$

where, ρ_2 is the transverse surface relaxivity (m/s); β is the shape factor of the pores and τ is the tortuosity of the pore system. The surface relaxivity of the Eagle Ford shale is reported as 4.4 nm/ms based on NMR calibration with SEM pore size distribution [110].

The shape factor (β) and tortuosity (τ) values are provided through digital rock analysis of the generated pore network models of the LEF shale samples, detailed in another phase of the study [77]. The geometric mean (T_{2LM}) term represents as an equivalent porous medium of the pore system with a single transverse (T_2) relaxation time value of T_{2LM} [107].

The NMR estimated permeability is listed in Table 4-7 and compared to the pulse decay permeability on cleaned mesh with CO_2 and toluene by Core laboratories. The NMR permeability of both Samples A and B have the same order of magnitude as the pulse decay permeability, while Sample C deviates. This could be attributed to the pore-scale values of the shape factor (β) and tortuosity (τ), which are not representative of a core scale. Moreover, the pulse decay measurements are also susceptible to errors.

Table 4-7: Comparing Pulse decay (PD) and NMR permeability estimation of the LEF samples

LEF samples	Average β	Average τ	PD permeability (mD)	NMR permeability(mD)
A	1.35	1.58	0.001752	0.001435
B	1.14	1.96	0.001332	0.002404
C	0.78	1.79	0.001978	0.000972

4.4 Conclusions

- The huff-n-puff process was evaluated with NMR T_2 distribution, where reduced amplitude gives an indication of oil/hexadecane recovery and a shift to the left is interpreted as remaining heavier fractions. Injected methane gas during hydrocarbon gas huff-n-puff was observed to invade smaller pores within the bound and organic pore spaces to be confined and/ or adsorbed.
- 2D $T_1 - T_2$ maps were used to better differentiate the remaining fluid type after the huff-n-puff recovery process in respective pore systems. Oil/hexadecane in organic pores has a T_1/T_2 ratio ~3.8 with T_2 distribution of 1 – 16 ms. Methane gas from the hydrocarbon gas injection was observed to be confined/adsorbed in the bound and organic pore region with T_1/T_2 ratio > 10. Methane confinement or adsorption in the bound region is plausible due to the observed migrated organic matter with developed organic pores infilling the intra-particle pores of mostly kaolinite in forams as determined on SEM/BSE images of the LEF shale samples. Hydroxyls from clay minerals in addition to fluids confined/adsorbed in the intra-particle clay pores exhibited very high T_1/T_2 ratio > 60 in Sample C with the highest clay mineral content. Furthermore, the increase in amplitude of the NMR T_2 distribution to indicate fully saturated cores justifies the efficiency of our saturation method for the LEF reservoir cores and EF Outcrop.

- NMR estimated saturation before and after huff-n-puff refers to a decreases (~20%) in the hydrocarbon content after huff-n-puff, which is reflected in reduced cumulative porosity values. Sample C, at the bottom of the core, shows lower recovery compared to the other two samples from the upper part of LEF.
- Three (3) main pore systems were identified when samples were saturated with oil/ hexadecane, namely, micro-pores (T_2 < 1 ms), meso-pores (1< T_2 < 16 ms), and macro-pores (T_2 > 16 ms) including fractures (T_2 > 100 ms).
- NMR permeability from SDR for each LEF shale sample compares the pulse decay permeability in the same order of magnitude for Samples A and B, while Sample C slightly deviates from the order.

Publication:

Cudjoe, S., Oraki, I., Barati, R., Tsau, J.-S., Zhang, C., Nicoud, B., . . . Mohrbacher, D. (2019). Nuclear Magnetic Resonance Estimation of Petrophysical Properties and Evaluation of Hydrocarbon Huff-n-Puff Gas Injection in Lower Eagle Ford Shale Oil Samples. *Unconventional Resources Technology Conference* (pp. 1-15). Denver: URTeC.

5 CHAPTER 5: LATTICE BOLTZMANN SIMULATION

Simulating fluid flow and estimating bulk transport properties such as permeability in organic-nanopores of shales is challenging due to the pore diameter being comparable to the mean free path of gas molecules. This leads to predominant pore wall effects such as adsorption/desorption, Knudsen diffusion, and surface diffusion, in addition to fluid-fluid interactions. In so doing, the conventional Darcy's equation becomes unreliable.

The lattice Boltzmann model (LBM) offers a molecular means of capturing the pore-wall effects based on the kinetic theory. In the kinetic theory, a gas molecule is assumed to be composed of interacting particles, which undergo both streaming and collision to conserve mass and momentum. From the collective behavior of the microscopic particles, macroscopic properties like velocity, density, and pressure can resolved accordingly.

Therefore, this chapter covers the use of the LBM to simulate gas molecules in micro-channels of varying sizes at the nano-pore scale emphasizing on the effect of the pore wall interactions on permeability; an important bulk transport property often estimated incorrectly.

5.1 Lattice Boltzmann Model (LBM)

The lattice Boltzmann model (LBM) considers the trajectory of a group of particles instead of individual particles in molecular dynamics (MD), making it less computationally extensive. Thus, LBM bridges the gap between micro-scale (MD) and macro-scale (Navier-Stokes equation) [111]. The lattice Boltzmann models (LBMs) originate from the lattice gas cellular automata (LGCA) models developed to replicate the complexities of real fluid flow on triangular or hexagonal lattices. In the LGCA models, fluid is represented by Boolean variables (0 or 1) [112, 113]. Based on a set of rules, initial and boundary conditions, a cellular automaton (an algorithmic entity), at a

given position on a lattice in space interacts with neighboring entities and evolves with time. The interaction at a given time consists of streaming in which the particles propagate to new sites and collision, where they collide based on the set of collision rules [114, 115]. However, the LGCA models were riddled with statistical noise due to the discrete Boolean variables [116].

Subsequently, the LBMs were developed by replacing the Boolean variables with distribution functions ($f(x,t)$) assigned to a group of particles confined to a lattice in space and time [117] . The LBM solves the Boltzmann equation (BE) derived from the kinetic theory, where a gas is assumed to be composed of interacting particles, which undergo both streaming and collision to conserve mass and momentum [113]. It simplifies Boltzmann's concept by reducing the number of particle spatial positions and microscopic momenta from a continuum [116, 114]. Figure 5.1 shows a 2D Cartesian model with nine (9) velocities including the particle at rest (e_0) in eight directions assuming a single/uniform mass particle with equivalent microscopic velocities and momenta [114, 118]. The velocity indexing below is very common, although other forms exist. Lattice unit (lu) is the measure of the length in LBMs, while time is measured in time steps (ts). Therefore, the velocity magnitude of e_1 to e_2 (particles along the *x*- and *y*-axes) is one (1) lattice unit per time step (lu/ts) and that between e_6 and e_7 (particles along diagonal axes) is $\sqrt{2}$ lu/ts. Other commonly used LBMs are listed below in Table 5-1 together with their corresponding lattice velocities and associated weighting factors; the speed of sound is dependent on the models. It is also observed that all the *x*- and *y*- components are either 0 or ±1 [116, 118].

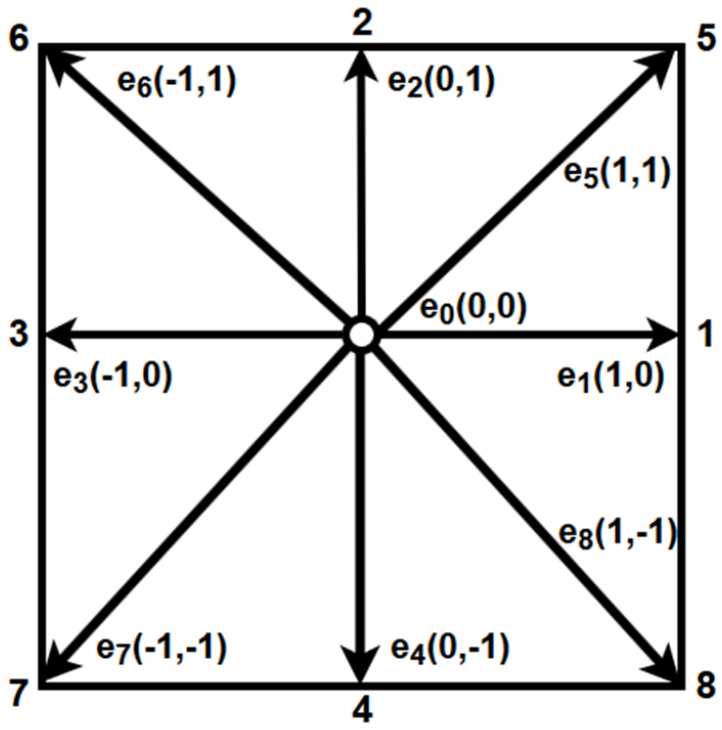

Figure 5.1: D2Q9 lattice and velocities (modified after [119])

The distribution function ($f(x,e,t)$) represents the number of molecules at a time (t) located at positions between x and $x+\Delta x$ within a range of velocities between e and $e+\Delta e$. Particles in a fluid medium reside on lattice nodes and move to their nearest neighbors along the lattice links. Applying an external force will cause a change in the velocity and position of a unit mass gas molecule and upon collision, a net difference occurs between the number of molecules before and after collision leading to a rate change referred to as the collision operator, Ω [111, 120]. Bhatnagar-Gross-Krook (BGK) [121] introduced a simple linearized collision model to solve the Boltzmann equation and it assumes the distribution is close to local equilibrium state [122]. The LBM-BGK equation is therefore expressed in Eq.(5-1) [113], where the left-hand side (LHS) represents the streaming (advection) term and the right-hand side (RHS) represents the collision process

Table 5-1: Some LBMs and their corresponding parameters (modified after [119])

Model	Lattice velocity (e_i)	Weight (w_i)	Speed of sound (c_s^2)
D1Q3	$0,$	$2/3,$	1/3
	± 1	$1/6$	
D1Q5	0	$6/12,$	1
	$\pm 1,$	$2/12,$	
	± 2	$1/12$	
D2Q7	$(0,0)$	$1/2$	1/4
	$\left(\pm 1/2, \pm\sqrt{3}/2\right)$	$1/12$	
D2Q9	$(0,0)$	$4/9$	1/3
	$(\pm 1,0),(0,\pm 1),$	$1/9$	
	$(\pm 1,\pm 1)$	$1/36$	
D3Q15	$(0,0,0),$	$2/9,$	1/3
	$(\pm 1,0,0),(0,\pm 1,0),(0,0,\pm 1),$	$1/9,$	
	$(\pm 1,\pm 1,\pm 1)$	$1/72$	
D3Q19	$(0,0,0)$	$1/3$	1/3
	$(\pm 1,0,0),(0,\pm 1,0),(0,0,\pm 1)$	$1/18$	
	$(\pm 1,\pm 1,0),(\pm 1,0,\pm 1),(0,\pm 1,\pm 1)$	$1/36$	

$$f_i(x + e_i\Delta t, t + \Delta t) - f_i(x,t) = -\frac{1}{\tau}\left[\left(f_i(x,t)\right) - f_i^{eq}(x,t)\right] \tag{5-1}$$

where, τ is the single relaxation factor, which controls the rate to attain equilibrium, and f^{eq} is the local equilibrium distribution function (EDF) dependent on the LBM in use. The relaxation time (τ) is related to the kinematic viscosity and expressed as

$$v = c_s^2(\tau - 0.5)\Delta t \tag{5-2}$$

where, v is the kinematic viscosity and c_s is the speed of sound; the unit of the kinematic viscosity is lu^2/ts.

The relaxation time (τ) varies for different simulations and some stable values proposed in literature are 0.6 and 1. Although, the single relaxation time (SRT) is commonly used, other relaxation times are reported including the two-relaxation-time (TRT) [123] and the multi-relaxation time (MRT) [124, 125]; the MRT is proposed to have higher numerical stability and accuracy than both SRT and TRT.

Subsequently, the macroscopic fluid properties like density (ρ) and velocity (u) can be resolved through the collective behavior (statistical mechanics) of the microscopic particles described by the Navier-Stokes equation and expressed as

$$\rho = \sum_{i=0}^{8} f_i \tag{5-3}$$

$$u = \frac{1}{\rho}\sum_{i=0}^{8} f_i e_i \tag{5-4}$$

The EDF of the D2Q9 model is defined as

$$f_i^{eq}(x,t) = w_i \rho \left(1 + \frac{e_i.u}{c_s^2} + \frac{(e_i.u)^2}{2c_s^2} - \frac{u^2}{2c_s^2}\right) \tag{5-5}$$

where, w_i is the weighting factor of each lattice link; c_s is the speed of sound and u is the fluid velocity. External forcing terms are incorporated into the adjusted fluid velocity term (u^{eq}) in the EDF equation. An example of incorporating gravity starts by considering the equation for Newton's second law of motion, expressing the acceleration term as the rate change of velocity with time (du/dt) and with density being proportional to the mass, the resulting expression is given as

$$u^{eq} = u + \Delta u = u + \frac{\tau F}{\rho} \tag{5-6}$$

where, Δu is the change in velocity, F is the forcing term, and ρ is the fluid density.

The LBM can be applied in complex geometries [126, 127, 128] by implementing different boundary conditions LBM can also be used to simulate both single and multiphase fluids incorporating particle-particle interactions and particle-surface interactions to understand phase separation and study contact angles [129, 130, 131, 120]. It is also applicable to thermal and reactive flows and can be used to estimate the apparent permeability [132, 133].

5.1.1 Implementing LBM in Organic Nanopores

Fluid transport in organic-nanopores is determined by permeability, the ability of a medium to transmit fluids, among other factors. Conventionally, permeability in sedimentary rocks is estimated from Darcy's law. However, due to the transition flow regime associated with organic nano-pores, pore wall effects including rarefied gas flow, adsorption, surface and Knudsen diffusions are encountered, which render Darcy's equation inadequate. Figure 5.2 illustrates the pore-wall effects; a) shows the viscous flow and Knudsen diffusion, while b) shows surface diffusion. Viscous flow is encountered in macro-pores (> 50 nm), where the collision between the gas molecules is dominant, while Knudsen diffusion occurs as a result of the frequent gas-solid surface interactions when the free mean path is comparable to the thickness/diameter of the domain. On the other hand, surface diffusion occurs in micro-pores (< 2 nm) and serves as the dominant transfer mechanism of strongly adsorbed gas on the pore walls driven by the concentration gradient [134, 135].

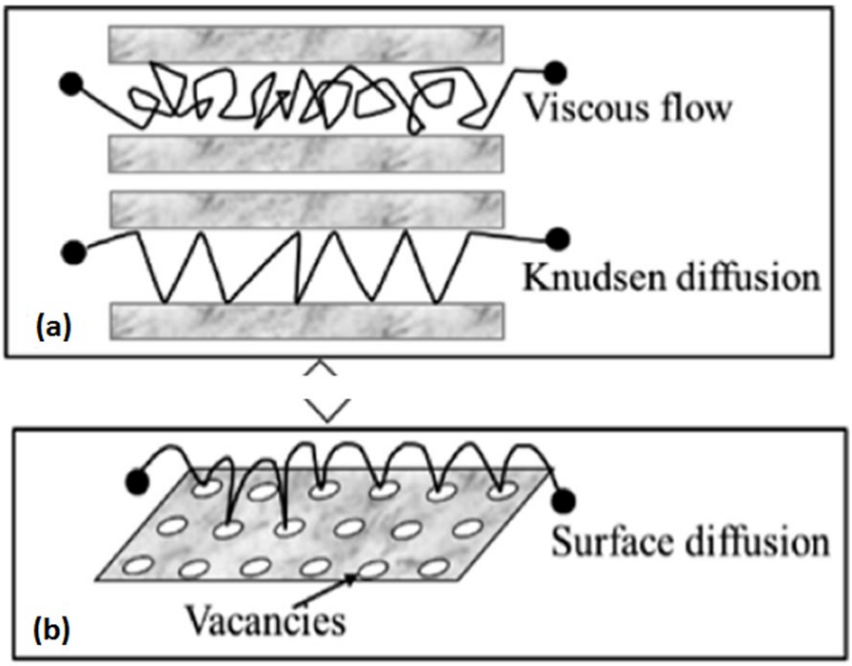

Figure 5.2: Pore wall effects encountered in organic nanopores; (a) viscous flow and Knudsen diffusion (b) surface diffusion after [135]

The various flow regimes are classified by the Knudsen number (Kn), which is a dimensionless parameter defined as the ratio of the gas mean free path to the characteristic length of the medium [136]. Fluid flow behaves differently at various Knudsen numbers as such values are assigned to determine respective flow regimes. Continuum flow regime occurs at $Kn < 0.01$, slip flow regime is in the range of $0.01 < Kn < 0.1$, transition flow is considered as $0.1 < Kn < 10$, and free-molecular flow regime is observed at $Kn > 10$. The main fluid transport regime within the nanopores of shales is determined to be the slip flow and transition regimes [137], as a result, both viscous flow and Knudsen diffusion impart fluid transport in shales.

Analytical models for continuum flow estimates the mass flux to be dependent on the absolute permeability (mD) of the rock and is expressed as [138, 139]

$$J_a = -\frac{\rho_{avg} r^2}{8\mu} \frac{\nabla p}{L} \tag{5-7}$$

where, J_a is the mass flux due to pressure difference, r is the pore radius, μ is the viscosity, L is the pore length, and ρ_{avg} is the average density. The corresponding absolute permeability is expressed below as

$$K = \frac{r^2}{8} \tag{5-8}$$

In the slip flow regime, gas slippage is observed to occur where the mean free path of the gas molecules are comparable to the characteristic length of the medium, which leads to the Klinkenberg effect [140]. The Klinkenberg effect causes the measured apparent permeability of a gas to be higher than the liquid permeability or intrinsic permeability. In effect, the Kn increases with an increase in the ratio of the fluid-wall interactions to fluid-fluid interactions; the corresponding mass flux and permeability are expressed as

$$J_{a\_s} = -F\frac{\rho_{avg} r^2}{8\mu}\frac{\nabla p}{L} \tag{5-9}$$

$$K = F\ \frac{r^2}{8} \tag{5-10}$$

where, F is a theoretical dimensionless coefficient defined by Javadpour [139] in terms of the gas constant and the tangential momentum accommodation coefficient.

Gas flow due to Knudsen diffusion in the transition regime in a nano-pore is expressed below; the resulting permeability is found to be dependent on pressure as flow is dominated by Knudsen diffusion and slip flow

$$J_D = \frac{MD_K}{10^3 RT}\nabla P \tag{5-11}$$

where, M is molar mass, D_K is the Knudsen diffusion constant, R is the gas constant, and T is absolute temperature.

The pore wall effects are incorporated into the LBM simulation by modifying the relaxation time according to the prevailing Knudsen number and this is given as [127, 137]

$$\psi(Kn) = \frac{2}{\pi} arctan\left(\sqrt{2} Kn^{-3/4}\right) \tag{5-12}$$

$$\tau_e = \tau\psi(Kn) \tag{5-13}$$

where, Kn is the Knudsen number and τ_e is the effective relaxation time capable of capturing the gas-wall interactions. As a result, the relaxation time is observed to decrease with a corresponding increase in theKn [138]. Thus, when pore wall interactions becomes dominant, gas molecules undergo collision at short relaxation times.

5.1.2 Boundary Conditions

Several boundary conditions can be implemented through the LBM to capture the complexities of the geometry as well as the fluid-solid interactions at the pore walls. These include, the bounce-back boundary condition (no-slip) [141], the hydrodynamic boundary conditions (Dirichlet & Von Neumann) [142, 143], temperature jump & velocity slip [144, 145] as well as Langmuir slip conditions [146, 147, 148].

The no-slip boundary condition is commonly implemented in LBM as the bounce-back condition (BB), where a particle reaching the pore wall (boundary node) bounces back to the fluid column (fluid node) without adsorption. However, for complex medium like the nanopores of shales, where adsorption of gas molecules onto the kerogen nanopores prevails, the Langmuir slip model (LSM) is utilized at the boundary.

Adsorption/desorption, surface diffusion, among other organic nano-pore flow behaviors are realized with the LSM and can be implemented by either the bounce-back/specular-reflection (BSR) [149] or the non-equilibrium extrapolation scheme [146]. The Langmuir slip model (LSM) is developed based on the Langmuir theory of adsorption and is proven to be more effective than the use of the accommodation coefficient (σ), which does not capture the real fluid-solid interactions [136]. Thus, in the LSM, gas molecules are assumed to adsorb to the pore walls for some amount of time before desorbing into the fluid [148]. This causes a macroscopic slip velocity to develop, which is captured in the LSM in the expression below [146]

$$u_{slip} = (1-\alpha)u_g + \alpha u_w \tag{5-14}$$

where, u_{slip} is the slip velocity, u_g is the gas velocity at one mean free path away from the wall, u_w is the local wall velocity due to the adsorbed-phase transport (surface diffusion), and α is the amount of adsorbed gas. The adsorbed gas is expressed as a function of the Kn for monatomic gases below [147, 148]

$$\alpha = \frac{1}{1+4\omega Kn/p} \tag{5-15}$$

where, ω is determined through experimental data or theoretical consideration of intermolecular force and the gas-surface interaction and p is the pressure.

As the amount of adsorbed gas approaches a maximum (*e.g.* $\alpha = 1$), the Kn approaches zero, and this results in only the adsorbed-gas velocity (surface diffusion) contributing to the slip velocity from Eq.$\mathrm{u_{slip}} = (1\text{-}\alpha)\mathrm{u_g} + \alpha\mathrm{u_w}$

(5-14). The adsorbed-gas velocity (surface diffusion) is expressed as [149]

$$u_w = -D_s \frac{\rho_s M}{\rho_{ads} V_{std}} \frac{V_L p_L}{(p_L+p)^2} \frac{\partial p}{\partial x} \tag{5-16}$$

where, u_w is the adsorbed gas velocity (surface diffusion), D_s is the surface diffusion coefficient, ρ_s is the organic solid density, M is the gas molecular weight, V_{std} is the gas volume per mole at standard temperature and pressure (STP), V_L is the Langmuir volume, p_L is the Langmuir pressure, and p is the prevailing gas pressure.

5.1.3 Interaction Forces between Fluid Molecules and Pore Walls

Shan and Chen [150] introduced the attractive short-range (cohesive) force between neighboring fluid particles in addition to the local collisions expressed as

$$F(x,t) = -G\psi\big(\rho(x,t)\big)\sum_{i=1}^{8} w_i \psi\big(\rho(x+e_i\Delta t,t)\big)e_i \tag{5-17}$$

where, $F(x,t)$ is the cohesive force between fluid-fluid particles, G is the interaction strength, and $\psi\big(\rho(x,t)\big)$ is the interaction potential expressed as a function of the fluid density.

The adhesive forces between the fluid and solid phases is expressed as [151]

$$F_{ads} = -G_{ads}\psi(x,t)\sum_{i=1}^{8} w_i\, s(x+e_i\Delta t)e_i \tag{5-18}$$

where, $s = 0$ for fluid nodes and $s = 1$ for solid nodes, respectively. G_{ads} is the particle interaction strength between fluid and solid walls.

5.2 LBM Micro-Channel Application

The effects of gas slippage and surface diffusion on the permeability are considered in varying sizes of micro-channel inferred from FIB-SEM imaging of the LEF samples. The channel length of the pore throats are observed to vary from 8 nm - 700 nm. The specific values of surface diffusion coefficient and Langmuir property of the shale samples are not easily available and

require future experiments. As such the model parameter values of adsorbed gas and surface diffusivity were carefully chosen from reported findings on methane flow in organic shales [152]. The surface diffusivity (D_s) varies from 0 – 1 x 10^{-6} m^2/s, the Langmuir constant (P_L) is in the range of 0.125 – 1 MPa^{-1}, and the Langmuir volume (V_L) is between 1000 to 8000 mol/m^3.

A pressure driven methane flow through 400 nm long micro-channels with width varying from 5 nm – 50 nm are considered at a high pressure of 24 MPa & 398 K and at a low pressure of 5MPa & 300 K, respectively. While the high pressure (24 MPa) accounts for reservoir conditions, the low pressure (5MPa) represent common pressure for permeability measurement using transient pulse decay.

The effects of adsorbed layers of methane, gas slippage, and surface diffusion at the pore walls on the flow behavior in the micro-channels are analyzed. The adsorbed layer is represented by relating the size of the micro-channels to the pressure through the Kn. In so doing, the effects of adsorption and slip are observed to be dependent on pressure and the width of the micro-channels. The only effect of pressure is the change in the Kn to indicate a degree of slip. Intrinsic permeability (K_{in}) with no-slip is computed to serve as reference value and is expressed as

$$K_{in} = \frac{H^2}{12} \tag{5-19}$$

where, H^2 is the width of the micro-channel

The apparent permeability due to gas slippage (K_{app_s}) and surface diffusion (K_{app_surf}), respectively, are also expressed below as [152, 140]

$$K_{app\_s} = K_{in}(1 + \alpha Kn) \tag{5-20}$$

$$K_{app\_surf} = \frac{N_{total} M \mu}{(\rho \Delta p)} \tag{5-21}$$

where, N_{total} is the molar flux contributions from the surface diffusion and the free gas (non-adsorbed gas), M is the molar mass of methane gas, and Δp is the pressure gradient of flow

5.2.1 Varying Characteristic Length of the Micro-Channels

The effect of the channel width on the apparent permeability is studied by varying the width (5 nm, 10 nm, 30 nm, and 50 nm) at the two specified pressures with different Langmuir parameters but with a constant surface diffusivity at 10^{-5} m^2/s. At such a high surface diffusivity, the increase in the width of the micro-channel resulted in an increase in the apparent permeability at both high and low pressures, observed in Table 5-2 and Table 5-3, respectively. This can be attributed to the dominant viscous flow in larger pores, where the pore wall effects of gas slip and surface diffusion are negligible and the apparent permeability is close to the intrinsic permeability. In addition the apparent permeability due to slip at the low pressure of 5 MPa is more pronounced than that at high pressure (24 MPa) as the channel width increases (Table 5-3).

Because the adsorbed gas layer dominate at high pressure, the apparent permeability due surface diffusion as a result of the adsorbed layer is more pronounced at the high pressure of 24 MPa than the low pressure with increasing channel width (Table 5-2).

Table 5-2: The influence of channel width on gas permeability under different pore wall interactions at 24 MPa and 398 K

P = 24 MPa; T = 398 K				
	H = 5 nm	**H = 10 nm**	**H = 30 nm**	**H = 50 nm**
	***Kn* = 0.11**	***Kn* = 0.055**	***Kn* = 0.0184**	***Kn* = 0.011**
Kin (mD)	0.002111	0.00844	0.07599	0.211
Kapp_s (mD)	0.00328	0.01077	0.0830	0.233
Kapp_surf (mD)	0.0594	0.11754	0.3506	0.585

Table 5-3: The influence of channel width on gas permeability under different pore wall interactions at 5 MPa and 300 K

P = 5 MPa; T = 300 K				
	H = 5 nm	**H = 10 nm**	**H = 30 nm**	**H = 50 nm**
	***Kn* = 0.24**	***Kn* = 0.121**	***Kn* = 0.0402**	***Kn* = 0.024**
Kin (mD)	0.002111	0.00844	0.07599	0.211
Kapp_s (mD)	0.0466	0.0135	0.0912	0.237
Kapp_surf (mD)	0.0384	0.075	0.222	0.369

Figure 5.3 shows a schematic methane flow in a micro-channel of 400 nm length by 10 nm width with the maximum velocity within the center following the Hagen-Poiseuille flow between two parallel plates but with a slip velocity at the pore walls.

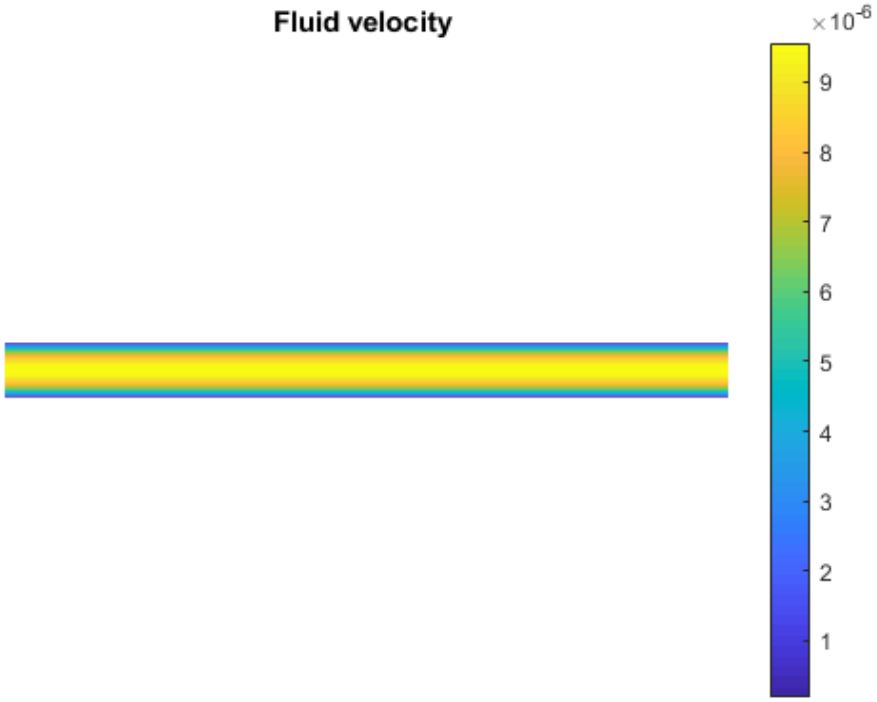

Figure 5.3: Methane flow in a schematic micro-channel with length of 400 nm and width of 10 nm

5.2.2 Effect of Pressure

The apparent permeability due to gas slippage is observed to be enhanced at low pressure (Table 5-3) than at the high pressure (Table 5-2). This is because the low pressure increases slippage and reduces thickness of the adsorbed layer. Figure 5.4 and Figure 5.5 shows the velocity profile of methane in a smaller (5 nm) micro-channel and a 10 nm channel, respectively; the slip velocity is observed to be pronounced in the smaller micro-channel.

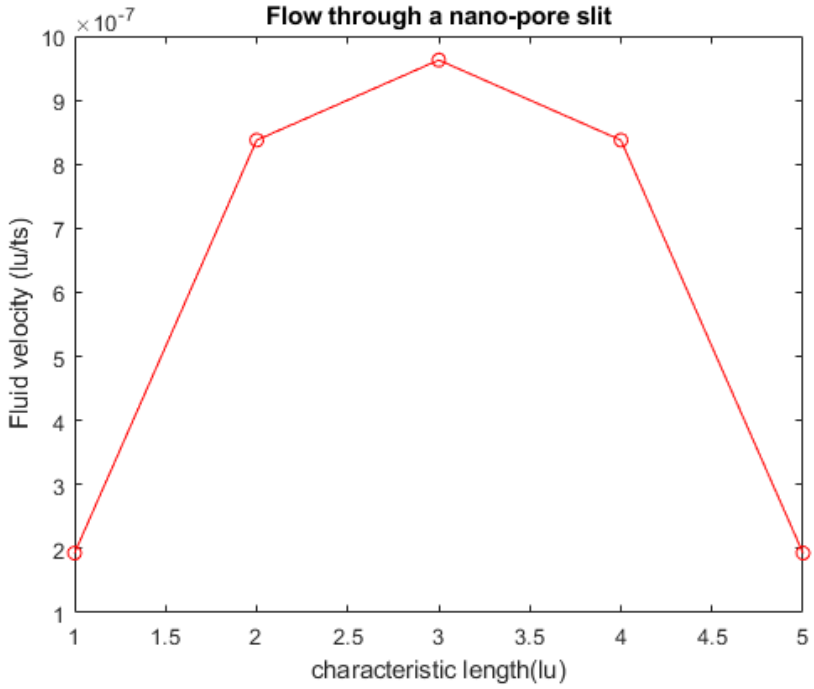

Figure 5.4: Velocity profile of methane gas within a micro-channel of 5 nm with pronounced slip velocity at 1.93 x 10^{-7} lu/ts

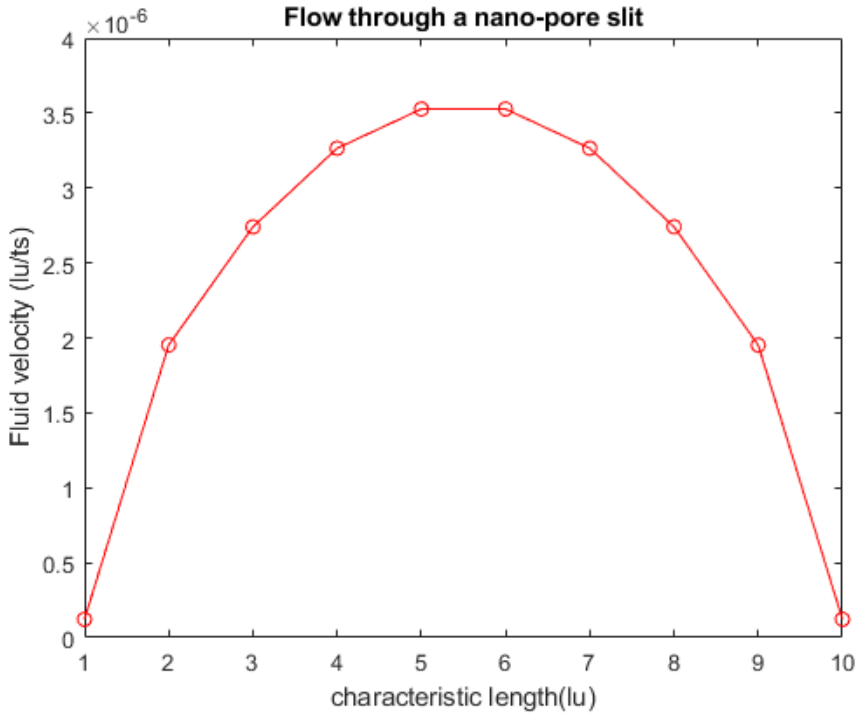

Figure 5.5: Velocity profile of methane gas within a micro-channel of 10 nm with gas slippage

5.3 Conclusion

- The LBM with a modified boundary condition of LSM is applied to varying micro-channel widths inferred from FIB-SEM of the LEF samples to factor in pore wall effects such as gas slippage and surface diffusion due to adsorption, otherwise neglected in permeability estimations.
- The effect of the varying channel width and pressure on the apparent permeability due to slippage and surface diffusion are analyzed.
- The apparent permeability due to gas slippage is enhanced at low pressures, which can be considered for later stages of hydrocarbon production from shale reservoirs, when the pressure declines.

6 SUMMARY

An integrated workflow is developed, which comprises of reservoir-scale and pore-scale characterization, respectively.

- Chapter 1: The reservoir-scale characterization combined seismic, well logs and laboratory measurements to develop a quality map capable of delineating spots for effective hydraulic fracturing in a Chattanooga shale interval with little or no prior detailed characterization information. The methods of defining petrophysical correlations among other results obtained can be applied to other shale formations.
- Chapter 2: Pore-scale characterization focused on advanced imaging using SEM/BSE/EDS and FIB-SEM to investigate organic vs. inorganic transport properties in LEF shale samples, while clarifying the *in-situ* processes that occur in the pore structure during hydrocarbon gas huff-n-puff. The complexity in the pore structure of shales, otherwise challenging to capture, are modeled under this study. The results acquired can be used in numerical simulation and rock characterization to optimize recoveries and economics of different shale formations for huff-n-puff.
- Chapter 3: Application of Raman spectroscopy improved understanding of compositional controls in kerogen (organic matter) contained in shales as well as the use of Raman spectroscopy for thermal maturity measurement at the micro-scale. It is often reported that the temperature is the only control of the decomposition of kerogen to generate hydrocarbons, and subsequently develop organic pores. But in this study, we found that the original maceral composition plays a significant role in the development of indicators of thermal maturity by analyzing two types of organic matter (MOM and depositional kerogen) from the same

maturity windows. These findings were applied to investigate its impact on gas huff-n-puff recovery, for which the displacement of a portion of the MOM (bitumen) was observed.

- Chapter 4: The NMR was used to evaluate hydrocarbon gas huff-n-puff from LEF samples and also estimate petrophysical properties of the core plugs. The NMR estimated hydrocarbon recoveries were comparable to that of mass balance estimations. Furthermore, the remaining fluid type after huff-n-puff and the pore systems in which they are confined, were determined for a better understanding of the huff-n-puff process for optimization.
- Chapter 5: The LBM was implemented in micro-channels of the LEF shale inferred from pore-scale analysis (FIB-SEM) to effectively estimate the gas permeability. Gas permeability in micro-channels and nano-pores of shales are mostly affected by pore wall interactions but are not effectively captured in laboratory measurements and Darcy's equation. A better understanding of the gas flow behavior through shale was acquired by evaluating these effects in individual micro-channels of varying widths.

7 REFERENCES

[1] M. Lambert, "Internal Stratigraphy of the Chattanooga Shale in Kansas and Oklahoma," *Oklahoma Geological Survey Circular,* vol. 93, pp. 1-353, 1992.

[2] R. Spears and S. Jackson, "Development of a Predictive Tool for Estimating Well Performance in Horizontal Shale Gas Wells in the Barnett Shale, North Texas, USA," *Petrophysics,* vol. 50, no. 1, pp. 19-31, 2009.

[3] 15 03 2011. [Online]. Available: http://http://maps.kgs.ku.edu/oilgas/.

[4] L. Lines and R. Newrick, Fundamentals of Geophysical Interpretation, vol. 13, Society of Exploration Geophysicists, 2004.

[5] E. Crain and P. Holgate, "A 12-Step Program to Reduce Uncertainty in Kerogen-Rich Reservoirs," in *GeoConvention: FOCUS*, Calgary, 2014.

[6] D. Hush and B. Horne, "Progress in Supervised Neural Networks," *IEEE Signal Process Magazine,* vol. 10, no. 1, pp. 8-39, 1993.

[7] G. Archie, "The Electrical Resistivity Logs as an Aid in Determining some Reservoir Characteristics," *Trans AIME,* vol. 146, pp. 54-62, 1941.

[8] N. Al-Bulushi, "Predicting Water Saturation Using Artificial Neural Networks (ANNs)," in *1st Annual Middle East Regional SPWLA Symposium*, Abu Dhabi, 2007.

[9] P. Simandoux, "Dielectric Measurements in Porous Media and Application to Shaly Formation," *Revue del'Institut Francais du Petrole, Supplementary Issue,* pp. 193-215, 1963.

[10] J. Schmoker and T. Hester, "Organic Carbon in Bakken Formation, United States Portion of Williston Basin," *AAPG Bulletin,* vol. 67, no. 12, pp. 2165-2174, 1983.

[11] Q. Passey, S. Creaney, J. Kulla, F. Moretti and J. Stroud, "A Practical Model for Organic Richness from Porosity and Resistivity Logs," *AAPG Special Volumes,* vol. 74, no. 12, pp. 1777-1794, 1990.

[12] R. Rickman, M. Mullen, E. Petre, B. Grieser and D. Kundert, "A Practical Use of Shale Petrophysics for Stimulation Design Optimization: All Shale Plays are not Clones of the Barnett Shale," in *SPE Annual Technical Conference and Exhibition*, Denver, 2008.

[13] F. Wang and J. Gale, "Screening criteria for shale-gas systems," *Gulf Coast Association of Geological Societies Transactions,* vol. 59, pp. 779-793, 2009.

[14] X. Jin, S. Shah, J.-C. Roegiers and B. Zhang, "Fracability Evaluation in Shale Reservoirs- An Integrated Petrophysics and Geomechanics Approach," in *SPE Hydraulic Fracturing Technology Conference*, The Woodlands, 2014.

[15] EIA, "Annual Energy Outlook 2019 with projections to 2050," Washington, 2019.

[16] Z. Jiang, W. Zhang, C. Liang, Y. Wang, H. Liu and X. Chen, "Basic characteristics and evaluation of shale oil reservoirs," *Petroleum Research,* 2016.

[17] C. Zou, "Chapter 2 - Unconventional Continuous Petroleum Accumulation," in *Unconventional Petroleum Geology*, C. Zou, Ed., Boston, Elsevier, 2013, pp. 27-60.

[18] T. Hentz and S. Ruppel, "Regional lithostratigraphy of the Eagle Ford: Maverick Basin to East Texas Basin," *Gulf Coast Association of Geological Societies Transactions,* vol. 60, pp. 325-337, 2010.

[19] EIA, "Upadates to the EIA Eagle Ford Play Maps," U.S. Department of Energy, Washington, DC 20585, 2014.

[20] R. Martin, J. Baihly, R. Malpani, G. Lindsay and W. Atwood, "Understanding Production from Eagle Ford-Austin Chalk System," in *SPE Annual Technical Conference and Exhibition*, Denver, 2011.

[21] A. Schaiberger, "Diagenesis in the Upper Cretaceous Eagle Ford Shale," Colorado School of Mines - Department of Geology and Geological Engineering, Golden, Colorado, 2016.

[22] C. Pope, T. Palisch and P. Saldungaray, "Improving Completion and Stimulation Effectiveness in Unconventional Reservoirs - Field Results in the Eagle Ford Shale of North America," in *SPE/EAGE European Unconventional Resources Conference and Exhibition*, Vienna, 2012.

[23] EIA, "Review of Emerging Resources: U.S. Shale Gas and Shale Oil Plays," U.S. Department of Energy, Washington, 2011.

[24] W. Dawson and W. Almon, "Eagle Ford Shale variability: Sedimentologic influences on source and reservoir character in an unconventional resource unit," *Gulf Coast Association of Geological Societies Transactions,* vol. 60, pp. 181-190, 2010.

[25] T. Wan, "Evaluation of the EOR Potential in Shale Oil Reservoirs by Cyclic Gas Injection," Texas Tech University - Petroleum Engineering, Lubbock, 2013.

[26] S. DiSavino, "Reuters," 20 03 2019. [Online]. Available: https://www.reuters.com/article/us-natgas-waha-pipelines/get-your-natural-gas-in-texas-for-a-dime-prices-fall-to-record-low-idUSKCN1R11EM. [Accessed 15 04 2019].

[27] D. Orozco, A. Fragoso, K. Selvan and R. Aguilera, "Eagle Ford Huff-and-Puff Gas Injection Pilot: Comparison of Reservoir Simulation, Material Balance and Real Performance of the Pilot Well," in *SPE Annual Technical conference and Exhibition*, Dallas, 2018.

[28] A. Fragoso, Y. Wang, G. Jing and R. Aguilera, "Improving Recovery of Liquids from Shales through Gas Recycling and Dry Gas Injection," in *SPE Latin American and Carribbean Petroleum Engineering Conference*, Quito, 2015.

[29] J. J. Sheng, "Optimization of huff-n-puff gas injection in shale oil reservoirs," *Petroleum,* vol. 3, no. 4, pp. 431-437, 2017.

[30] T. D. Gamadi, J. J. Sheng, M. Y. Soliman, H. Menouar, Watson M.C. and Emadibaladehi H., "An Experimental Study of Cyclic CO2 Injection to Improve Shale Oil Recovery," in *SPE Improved Oil Recovery Symposium*, Tulsa, 2014.

[31] R. R. R. R. S. a. J. D. Loucks, "Morphology, Genesis, and Distribution of Nanometer-Scale Pores in Siliceous Mudstones of the Mississippian Barnett shale," *Journal of Sedimentary Research,* pp. 848-861, 2009.

[32] C. Chen, D. Hu, D. Westacott and D. Loveless, "Nanometer-scale characterization of microscopic pores in shale kerogen by image analysis and pore-scale modeling," *Geochem. Geophys. Geosyst.,* vol. 14, no. 10, pp. 4066 - 4075, 2013.

[33] V. Shabro, S. Kelly, C. Torres-Verdin, K. Sepehrnoori and A. Revil, "Pore-scale modeling of electricla resistivity and permeability in FIB-SEM images of organic mudrock," *Geophysics,* vol. 79, no. 5, pp. D289 - D299, 2014.

[34] L. T. Ko, R. G. Loucks, S. C. Ruppel, T. Zhang and S. Peng, "Origin and characterization of Eagle Ford pore networks in the south Texas Upper Cretaceous shelf," *AAPG Bulletin,* vol. 101, no. 3, pp. 387-418, 2017.

[35] T. Saif, Q. Lin, A. Butcher, B. Bijeljic and M. Blunt, "Multi-scale multi-dimensional microstructure imaging of oil shale pyrolysis using X-ray micro-tomography, automated ultra-high resolution SEM, MAPS Mineralogy and FIB-SEM," *Applied Energy,* vol. 202, pp. 628-647, 2017.

[36] K. L. Milliken, L. T. Ko, M. Pommer and K. M. Marsaglia, "SEM Petrography of Eastern Mediterranean Sapropels: Analogue Data for Assessing Organic Matter in Oil and Gas Shales," *Journal of Sedimentary Research,* vol. 84, pp. 961-974, 2014.

[37] M. Curtis, R. Ambrose, C. Sondergeld and C. Rai, "Investigating the structure of gas shales on the nanoscale by FIB-SEM tomography and STEM imaging," in *The Society of Organic Petrology 28th Annual Meeting*, Halifax, Nova Scotia, Canada, 2011.

[38] R. Ambrose, R. Hartman, M. Diaz-Campos, I. Akkutlu and C. Sondergeld, "New Pore-Scale Considerations for Shale Gas in Place Calculations," in *SPE Unconventional Gas Conference*, Pittsburgh, 2010.

[39] C. Sondergeld, "Micro-Structural Studies of Gas Shales," in *SPE Unconventional Gas Conference*, Pittsburgh, 2010.

[40] S. Kelly, H. El-Sobky, C. Torres-Verdin and M. Balhoff, "Assessing the utility of FIB-SEM images for shale digital rock physics," *Advances in Water Resources,* vol. 95, pp. 302-316, 2016.

[41] J. Breyer, R. Denne, T. Kosanke, J. Spaw, J. Funk, P. Christianson, D. Bush and R. Nelson, "Facies, Fractures, Pressure and Production in the Eagle Ford Shale (Cretaceous) between the Maverick Basin and the San Marcos Arch, Texas, USA," in *Unconventional Resources Technology Conference*, Denver, 2013.

[42] W. Camp, "Diagenetic Evolution of Organic Matter Cements in Unconventional Shale Reservoirs," in *AAPG Annual Convention & Exhibition*, Denver, 2015.

[43] N. Fishman, J. Guthrie and M. Honarpor, "The Stratigraphic Distribution of Hydrocarbon Storage and its Effect on Producible Hydrocarbons in the Eagle Ford Formation, South Texas," in *Unconventional Resources Technology Conference*, Denver, 2013.

[44] K. Peters and M. Casa, "Applied Source Rock Geochemistry," in *The Petroleum System: From Source to Trap*, Tulsa, American Association of Petroleum Geologists, 1994, pp. 93-120.

[45] D. Jarvie, R. Hill, T. Ruble and R. Pollastro, "Unconventional shale-gas systems: The Mississippian Barnett Shale of North-Central Texas as one model for thermogenic shale-gas assessment," *AAPG Bulletin,* vol. 91, no. 4, pp. 475-499, 2007.

[46] L. Vicent and P. Soille, "Watersheds in Digital Spaces: An Efficient Algorithm Based on Immersion Simulations," *IEEE Transactions on Pattern Analysis and Machine Intelligences,* vol. 13, no. 6, pp. 583 - 598, 1991.

[47] N. R. Backeberg, F. Iacoviello, M. Rittner, T. M. Mitchell, A. P. Jones, R. Day, J. Wheeler, P. R. Shearing, P. Vermeesch and A. Striolo, "Quantifying the anisotropy and tortuosity of permeable pathways in clay-rich mudstones using models based on X-ray tomography," *Scientific Reports,* vol. 7, no. 1, pp. 1-12, 2017.

[48] J. Taillon, C. Pellegrinelli, Y.-L. Huang, E. Wachsman and L. Salamanca-Riba, "Improving microstructural quantification in FIB/SEM nanotomography," *Ultramicroscopy,* vol. 184, no. Part A, pp. 24-38, 2018.

[49] M. Matyka, A. Khalili and Z. Koza, "Tortuosity-porosity relation in porous media flow," *Physical Review E - Statistical, Nonlinear, and Soft Matter Physics,* vol. 78, no. 2, pp. 1-8, 2008.

[50] W. Camp, "Diagenetic Evolution of Organic Matter Cements in Unconventional Shale Reservoirs," in *AAPG Annual Convention & Exhibition*, Denver, CO, 2015.

[51] R. G. Loucks and R. M. Reed, "Scanning-electron-microscope petrographic evidence for distinguishing organic-matter pores associated with depositional organic matter versus migrated organic matter in mudrocks," *GCAGS Journal,* vol. 3, pp. 51-60, 2014.

[52] C. Marshall, H. Edwards and J. Jehlicka, "Understanding the Application of Raman Spectroscopy to the Detection of Traces of Life," *Astrobiology,* pp. 229 - 243, 2010.

[53] D. Long, Raman Spectroscopy, Great Britain: McGraw-Hill, 1977.

[54] S. R. Kelemen and H. L. Fang, "Maturity trends in Raman spectra from kerogen and coal," *Energy and Fuels,* 2001.

[55] M. Dresselhaus, A. Jorio and R. Saito, "Characterizing Graphene, Graphite, and Carbon Nanotubes by Raman Spectroscopy," *Annu. Rev. Condens. Matter Phys.,* pp. 89 - 108, 2010.

[56] F. Tuinstra and J. Koenig, "Raman spectrum of graphite," *J. Phys. Chem.,* vol. 53, pp. 1126-1130, 1970.

[57] M. Pimenta, G. Dresselhaus, M. Dresselhaus, L. Cancado, A. Jorio and R. Saito, "Studying disorder in graphite-based systems by Raman spectroscopy," *Phys. Chem. Chem. Phys.,* pp. 1276 - 1291, 2007.

[58] A. Jorio, R. Saito and M. Dresselhaus, Raman Spectroscopy in Nanoscience and Nanometrology: Carbon Nanotubes, Nanographite and Graphene, WeinHeim, Germany: Wiley-VCH Verlag GmbH & Co KGaA., 2010.

[59] A. C. Ferrari and J. Robertson, "Interpretation of Raman spectra of disordered and amorphous carbon," *Physical review B,* vol. 61, no. 20, pp. 95-107, 2000.

[60] F. Behar and M. Vandenbroucke, "Chemical modelling of kerogens," *Organic Geochemistry,* vol. 11, no. 1, pp. 15-24, 1987.

[61] K. Sato, R. Saito, Y. Oyama, J. Jiang, L. Cancado, A. Pimenta, G. Samsonidze, G. Dresselhaus and M. Dresselhaus, "D-band Raman intensity of graphitic materials as a function of laser energy and crystallite size," *Chem. Phys. Lett.,* vol. 427, pp. 117-121, 2006.

[62] S. Khatibi, M. Ostadhassan and A. Aghajanpour, "Raman spectroscopy: an analytical tool for evaluating organic matter," *J Oil Gas and Petrochem Sci.,* pp. 28-33, 2018.

[63] E. Krukowski and J. Howard, "Spatial Characterization of Organic Matter Maturity by Raman Microscope Mapping," in *Unconventional Resources Technology Conference (URTeC)*, Houston, 2018.

[64] S. Cheshire, P. Craddock, X. Guangping, B. Sauerer, A. Pomerantz, D. McCormick and A. Wael, "Assessing thermal maturity beyond the reaches of vitrinite reflectance and Rock-Eval pyrolysis: A case study from the Silurian Qusaiba formation," *International Journal of Coal Geology,* vol. 180, pp. 29-45, 2017.

[65] A. Schito, C. Romano, S. Corrado, D. Grigo and B. Poe, "Diagenetic thermal evolution of organic matter by Raman spectroscopy," *Organic Geochemistry,* vol. 106, pp. 57-67, 2017.

[66] B. Sauerer, P. R. Craddock, M. D. AlJohani, K. L. Alsamadony and W. Abdallah, "Fast and accurate shale maturity determination by Raman spectroscopy measurement with minimal sample preparation," *International Journal of Coal Geology,* vol. 173, pp. 150-157, 2017.

[67] M. Sato, "Thermochemistry of the formation of fossil fuels," *The Geochemical Society, Special Publication,* no. 2, pp. 271-283, 1990.

[68] B. Tissot and D. Welte, Petroleum Formation and Occurrence, Berlin Heidelberg New York Tokyo: Springer-Verlag, 1984, pp. 1-720.

[69] R. Pelet, "Evolution geochimique de la matiere organique," in *Kerogen*, B. Durand, Ed., Paris, Technip, 1980, pp. 475-499.

[70] F. Behar and P. Allix, "Kinetic modelling of kerogen cracking during oil shale process : influence of organic matter source," in *Oil shale symposium*, Golden, Colorado, 2012.

[71] J. Hunt, Petroleum Geochemistry and Geology, 2nd Edition ed., New York: W.H. Freeman&Company, 1996, p. 743.

[72] H. Tian, Z. Wang, Z. Xiao, X. Li and X. Xiao, "Oil cracking to gases: kinetic modeling and geological significance," *Chinese Science Bulletin,* vol. 51, no. 22, pp. 2763-2770, 2006.

[73] O. Beysacc, J.-N. Rouzaud, B. Goffe, F. Brunet and C. Chopin, "Graphitization in a high-pressure, low-temperature metamorphic gradient: a Raman microspectroscopy and HRTEM study," *Contrib Mineral Petrol,* vol. 143, no. 1, pp. 19-31, 2002.

[74] J. Forsman and J. Hunt, "Insoluble Organic Matter (Kerogen) in Sedimentary Rocks," *Geochmica et Cosmochimica Acta,* vol. 15, no. 3, pp. 170-182, 1958.

[75] J. Hunt and G. Jamieson, "Oil and Organic Matter in Source Rocks of Petroleum," *ibid,* vol. 40, no. 3, pp. 477- 488, 1956.

[76] C. Beny-Bassez and J. Rouzaud, "Characterization of carbonaceous materials by correlated electron and optical microscopy and Raman microspectroscopy," *Scanning Electron Microscopy,* no. 1, pp. 119-132, 1985.

[77] S. Cudjoe, R. Barati, R. Goldstein, J. Tsau, B. Nicoud, K. Bradford, D. Baldwin and D. Mohrbacher, "An Integrated Pore-Scale Characterization Workflow for Hydrocarbon Gas Huff-n-Puff Injection into the Lower Eagle Ford Shale," in *Unconventional Resources Technology Conference*, Denver, 2019.

[78] R. G. Loucks and R. M. Reed, "Scanning-electron-microscope petrographic evidence for distinguishing organic-matter pores associated with depositional organic matter versus migrated organic matter in mudrocks," *GCAGS Journal,* vol. 3, pp. 51-60, 2014.

[79] S. Bernard, R. Wirth, A. Schreiber, H. M. Schulz and B. Horsfield, "Formation of nanoporous pyrobitumen residues during maturation of the Barnett Shale (Fort Worth Basin)," *International Journal of Coal Geology,* pp. 3-11, 2012.

[80] N. Fishman, P. Hackley, H. Lowers, R. Hill, S. Egenhoff, D. Eberl and A. Blum, "The nature of porosity in organic-rich mudstones of the Upper Jurassic Kimmeridge Clay Formation, North Sea, offshore United Kingdom," *International Journal of Coal Geology,* pp. 32-50, 2012.

[81] R. T. McAllister, K. G. Taylor and B. Garcia-Fresca, "Diagenetic Evolution of the Eagle Ford Formation, SW Texas: Impacts upon Reservoir Quality and Rock Properties," in *Unconventional Resources Technology Conference (URTeC)*, San Antonio, 2015.

[82] R. Johnson, J. Birdwell and T. Mercier, "Petroleum Generation and Migration from the Oil Shale Interval of the Eocene Green River Formation, Uinta Basin, Utah," in *AAPG Pacific Section and Rocky Mountain Section Joint Meeting*, Las Vegas, 2017.

[83] N. Alharthy, T. W. Teklu, H. Kazemi, R. M. Graves, S. B. Hawthorne, J. Braunberger and B. Kurtoglu, "Enhanced Oil Recovery in Liquid-Rich Shale Reservoirs: Laboratory to Field," *SPE Reservoir Evaluation & Engineering,* vol. 21, no. 01, pp. 137-159, 20 9 2017.

[84] S. Hawthorne, C. Gorecki, J. Sorensen, E. Steadman, J. Harju and S. Melzer, "Hydrocarbon Mobilization Mechanisms from Upper, Middle, and Lower Bakken Reservoir Rocks Exposed to CO2," in *SPE Unconventional Resources Conference*, Calgary, 2013.

[85] G. R. Coates, L. Xiao and M. G. Prammer, NMR LOGGING PRINCIPLES & APPLICATIONS, Houston: Halliburton Energy Services, 1999, p. 251.

[86] H. Daigle, A. Johnson, J. P. Gips and M. Sharma, "Enhanced Formation Evaluation of Shales Using NMR Secular Relaxation* From Oil-Prone," in *AAPG Rocky Mountain Section Meeting*, Denver, 2010.

[87] M. Fleury and M. Romero-Sarmiento, "Characterization of shales using T1-T2NMR maps," *Journal of Petroleum Science and Engineering,* vol. 137, pp. 55-62, 2016.

[88] B. Nicot, N. Vorapalawut, B. Rousseau, L. Madariaga, G. Hamon and J.-P. Korb, "Estimating Saturations in Organic Shales Using 2D NMR," *Petrophysics,* vol. 57, no. 1, pp. 19-29, 2016.

[89] R. Kausik, K. Fellah, E. Rylander, P. M. Singer, R. E. Lewis and S. M. Sinclair, "NMR PETROPHYSICS FOR TIGHT OIL SHALE ENABLED BY CORE RESATURATION," in *nternational Symposium of the Society of Core Analysts*, Avignon, 2014.

[90] E. Rylander, P. M. Singer, T. Jiang, R. Lewis, Ryan Mclin and S. Sinclair, "NMR T2 Distributions in the Eagle Ford Shale: Reflections on Pore Size," in *SPE Unconventional Resources Conference*, The Woodlands, 2013.

[91] D. Veselinovic, D. Green and M. Dick, "Determination of Natural Fracture Porosity Using NMR," in *Unconventional Resources Technology Conference* , San Antonio, 2016.

[92] A. Valori, S. Van Den Berg, F. Ali and W. Abdallah, "Permeability Estimation from NMR Time Dependent Methane Saturation Monitoring in Shales," *Energy and Fuels,* vol. 31, no. 6, pp. 5913-5925, 15 6 2017.

[93] S. Dang, C. Sondergeld and C. S. Rai, "INTEPRETATION OF NMR RESPONSE TO HYDROCARBONS: APPLICATION ON MISCIBLE EOR EXPERIMENTS," in *International Symposium of the Society of Core Analysts*, Vienna, 2017.

[94] S. Cudjoe, R. Barati, R. Goldstein, J. Tsau, B. Nicoud, K. Bradford, A. Baldwin and D. Mohrbacher, "An Integrated Pore-Scale Characterization Workflow for Hydrocarbon Gas Huff-n-Puff Injection into the Lower Eagle Ford Shale," in *Unconventional Resources Technology Conference (URTeC)*, Denver, 2019.

[95] K. Dunn, D. Bergman and G. LaTorraca, Nuclear magnetic resonance: Petrophysical and logging applications, Pergamon: Elsevier Science, 2002.

[96] H. Carr and E. Purcell, "Effects of Diffusion on Free Precession in Nuclear Magnetic Resonance Experiments," *Physical Review,* vol. 94, no. 3, pp. 630-638, 1954.

[97] C. Lawson and R. Hanson, Solving Least Square Problems, Englewood Cliffs: Prentice-Hall, 1974.

[98] K. Dunn, G. LaTorraca, J. Warner and D. Bergman, "On the Calculation and Interpretation of NMR Relaxation Time Distributions," in *SPE 69th Annual Technical Conference and Exhibition*, New Orleans, 1994.

[99] M. Mehana and I. El-monier, "Shale characteristics impact on Nuclear Magnetic Resonance (NMR) fluid typing methods and correlations," *Petroleum,* pp. 138-147, 2016.

[100] S. Cudjoe, R. Barati, C. Marshall, R. Goldstein, J.-S. Tsau, B. Nicoud, K. Bradford, A. Baldwin and D. Mohrbacher, "Application of Raman Spectroscopy in Investigating the Effect of Source and Temperature on the Maturity of the Organic Matter Exposed to Hydrocarbon Gas Injection," in *Unconventional Resources Technology Conference*, Denver, 2019.

[101] Q. Fu, S. Cudjoe, R. Barati, J.-S. Tsau, X. Li, B. Nicoud, K. Bradford, A. Baldwin and D. Mohrbacher, "Experimental and Numerical Investigation of the Diffusion-Based Huff-n-Puff Gas Injection into Lower Eagle Ford Shale Samples," in *Unconventional Resources Technology Conference*, Denver, 2019.

[102] T. Zhang, G. Ellis, S. Ruppel, K. Miliken and R. Yang, "Effect of Organic-matter type and thermal maturity on methane adsorption in shale-gas systems," *J. Org. Geochem.,* vol. 47, pp. 120-131, 2012.

[103] A. Saada, B. Siffert and E. Papirer, "Comparison of the hydrophilicity/hydrophobicity of illite and kaolinites," *J. Colloid Interface Sci.,* vol. 174, pp. 185-190, 1995.

[104] G. Coates, R. Peveraro, A. Hardwick and D. Roberts, "The Magnetic Resonance Imaging Log Characterized by Comparison with Petrophysical Properties and Laboratory Core Data," in *SPE 66th Annual Technical Conference and Exhibition*, Dallas, 1991.

[105] A. Timur, "Pulsed nuclear magnetic resonance studies of porosity, movable fluid and permeability of sandstones," *Journal of Petroleum Technology,* vol. 21, no. 6, pp. 775-786, 1969.

[106] W. Kenyon, P. Day, C. Straley and J. Willemsen, "A three-part study of NMR longitudinal relaxation properties of water-saturated sandstones," *SPE Form. Eval.,* vol. 3, no. 3, pp. 622-636, 1988.

[107] H. Daigle and B. Dugan, "An improved technique for computing permeability from NMR measurements in mudstones," *J. Geophys. Res.,* vol. 116, pp. 1-14, 2011.

[108] P. Carman, "Flow through a granular bed," *Trans. Inst. Chem. Eng.,* vol. 15, pp. 150-156, 1937.

[109] J. Kozeny, "Uber kapillare Leitung des Wassers im Boden-Aufstieg, Versickerung und Anwendung auf die Bewasserung," *Sitz. Akad. Wiss. Wien,* vol. 136, pp. 271-306, 1927.

[110] T. Jiang, E. Rylander, P. Singer, R. Lewis and S. Sinclair, "Integrated Petrophysical Interpretation of Eagle Ford Shale with 1-D and 2-D Nuclear Magnetic Resonance (NMR)," in *SPWLA 54th Annual Logging Symposium*, New Orleans, 2013.

[111] A. A. Mohamad, Lattice Boltzmann Method: Fundamentals and Engineering Applications with Computer Codes, London Dordrecht Heidelberg New York: Springer-Verlag London Limited, 2011, p. 178 pp.

[112] S. Succi, The Lattice Boltzmann Equation for Fluid Dynamics and Beyond, Great Clarendon Street - Oxford: Oxford University Press, 2001.

[113] D. Wolf-Gladrow, Latttice-Gas Cellular Automata and Lattice Boltzmann Models - An Introduction, Berlin Heidelberg New York: Springer-Verlag, 2000.

[114] M. Sukop and D. Thorne, Lattice Boltzmann Modeling: An Introduction for Geoscientists and Engineers, Berlin Heidelberg New York: Springer-Verlag, 2006.

[115] U. Frisch, B. Hasslacher and Y. Pomeau, "Lattice-gas automata for the Navier-Stokes Equation," *Phys Rev Let,* vol. 56, pp. 1505-1508G, 1986.

[116] Z. Guo and C. Shu, Lattice Boltzmann Method and Its Applications in Engineering, Singapore: World Scientific Publishing Co. Pte. Ltd., 2013.

[117] G. McNamara and G. Zanetti, "Use of a Boltzmann Equation to Simulate Lattice-Gas Automata," *Phys. Rev. Lett.,* vol. 61, no. 20, pp. 2332-2335, 1988.

[118] Y. Qian, D. D'Humieres and P. Lallemand, "Lattice BGK Models for Navier-Stokes Equation," *Europhys. Lett.,* vol. 17, no. 6, pp. 479-484, 1992.

[119] Z. Guo and C. Shu, Lattice Boltzmann Method and Its Applications in Engineering, Singapore: World Scientific Publishing Co. Pte. Ltd., 2013.

[120] M. Sukop and D. Or, "Lattice Boltzmann Method for Modeling Liquid-Vapor Interface Configurations in Porous Media," *Water Resources Research,* vol. 40, no. W01509, p. W01509, 2004.

[121] P. Bhatnagar, E. Gross and M. Krook, "A Model for Collision Processes in Gases. I. Small Amplitude Processes in Charged and Neutral One-Component Systems," *Phys. Rev.,* pp. 511-525, 1954.

[122] D. A. Perumal and A. K. Dass, "A Review on the Development of Lattice Boltzmann Computation of Macro Fluid Flows and Heat Transfer," *Alexandria Engineering Journal,* vol. 54, pp. 955-971, 2015.

[123] I. Ginzburg, F. Verhaeghe and D. d'Humieres, "Two-Relaxation-Time Lattice Boltzmann Scheme: About Parametrization, Velocity, Pressure and Mixed Boundary Conditions," *Commun. Comput. Phys.,* vol. 3, no. 2, pp. 427-478, February 2008.

[124] P. Lallemand and L. Luo, "Theory of the lattice Boltzmann method: dispersion, dissipation, isotropy, Galilean invariance, and stability," *Phys. Rev. E,* vol. 61, pp. 6546-6562, 2000.

[125] D. d'Humieres, "Generalized lattice Boltzmann equation in rarefied gas dynamics: theory and simulations," *Progress in Astronautics and Aeronautics,* vol. 159, pp. 450-458, 1992.

[126] S. Zimny, K. Masilamani, K. Jain and S. Roller, "Lattice Boltzmann Simulations on Complex Geometries," in *Sustained Simulation Performance*, M. B. W. F. E. K. H. a. K. Y. Resch, Ed., Cham, Switzerland, Springer, Cham, 2013, pp. 49-62.

[127] K. Suga, S. Takenaka, T. Ito, M. Kaneda, T. Kinjo and S. Hyodo, "Evaluation of a lattice Boltzmann method in a complex nanoflow," *Physical Review E,* vol. 82, no. 016701, pp. 1-10, 2010.

[128] S. Succi, E. Foti and F. Higuera, "Three-Dimensional Flows in Complex Geometries with the Lattice Boltzmann Method," *EPL,* vol. 10, no. 5, pp. 433-438, 1989.

[129] H. Huang, M. Sukop and X.-Y. Lu, Multiphase Lattice Boltzmann Methods: theory and application, Chichester, West Sussex: John Wiley & Sons, Ltd, 2015.

[130] H. Huang, Z. Li, S. Liu and X.-y. Lu, "Shan-and-Chen-type multiphase lattice Boltzmann study of viscous coupling effects for two-phase flow in porous media," *Int. J. Numer. Meth. Fluids,* pp. 1-14, 2008.

[131] R. Benzi, L. Biferale, M. Sbragaglia, S. Succi and F. Toschi, "Mesoscopic modeling of a two-phase flow in the presence of boundaries: The contact angle," *Physical Review E,* vol. 74, pp. 1-14, 2006.

[132] N. Y., S. He, H. Liu and H. Wang, "Permeability Prediction Considering Surface Diffusion for Gas Shales by Lattice Boltzmann Simulations on Multi-

scale Reconstructed Digital Rocks," in *International Petroleum Technology Conference (IPTC)*, Bangkok, 2016.

[133] L. Chen, L. Zhang, Q. Kang, H. Viswanathan, J. Yao and W. Tao, "Nanoscale simulation of shale transport properties using the lattice Boltzmann method: permeability and diffusivity," *Scientific reports,* vol. 5, pp. 1-8, 2014.

[134] K. Wu, X. Li, G. C. and Z. Chen, "Adsorbed Gas Surface Diffusion and Bulk Gas Transport in Nanopores of Shale Reservoirs with Real Gas Effect-Adsorption -Mechanical Coupling," in *SPE Reservoir Simulation Symposium*, Houston, Texas, 2015.

[135] K. Wu, X. Li, C. Wang, W. Yu and Z. Chen, "Model for Surface Diffusion of Adsorbed Gas in Nanopores of Shale Gas Reservoirs," *Ind. Eng. Chem. Res.,* vol. 54, no. 12, pp. 3225-3236, 2015.

[136] E. Fathi, A. Tinni and I. Y. Akkutlu, "Correction to Klinkenberg slip theory for gas flow in nano-capillaries," *International Journal of Coal Geology,* vol. 103, pp. 51-59, 2012.

[137] D. Stops, "The Mean Free Path of Gas Molecules in the Transition Regime," *J. Phys. D: Appl. Phys.,* pp. 685-696, 1970.

[138] X. Zhang, L. Xiao, X. Shan and L. Guo, "Lattice Boltzmann Simulation of Shale Gas Transport in Organic Nano-pores," *Scientific reports,* pp. 1-6, 2014.

[139] F. Javadpour, "Nanopores and apparent permeability of gas flow in mudrocks (shales and siltstone)," *Journal of Canadian Petroleum Technology,* vol. 48, pp. 16-21, 2009.

[140] L. Klinkenberg, "The permeability of porous media to liquids and gases," *American Petroleum Institte, Drilling and Prodution practice,* pp. 200-213, 1941.

[141] S. Chen, D. Martinez and R. Mei, "On boundary conditions in lattice Boltzmann methods," *Physics of Fluids,* vol. 8, no. 2527, p. 2527, 1996.

[142] Q. Zou and X. He, "On pressure and velocity boundary conditions for the lattice Boltzmann BGK model," *Physics of Fluids,* vol. 9, no. 6, pp. 1591-1598, 1997.

[143] D. Noble, S. Chen, J. Georgiadis and R. Buckius, "A consistent hydrodynamic boundary condition for the lattice Boltzmann method," *Phys. Fluids,* vol. 7, no. 1, pp. 203-209, 1995.

[144] L. Zheng, B.-C. Shi and Z.-H. Chai, "Lattice Boltzmann Method for Simulating the Temperature Jump and Velocity Slip in Microchannels," *Commun. Comput. Phys.,* vol. 2, no. 6, pp. 1125-1138, December 2007.

[145] H. Huang, T. Lee and C. Shu, "Lattice Boltzmann Method Simulaiton Gas Slip Flow in Long Microtubes," *Int. J. Num. Methods for Heat & Fluid Flow,* vol. 17, no. 6, pp. 587-607, 2007.

[146] S. Chen and Z. Tian, "Simulation of thermal micro-flow using lattice Boltzmann method with Langmuir slip model," *International Journal of Heat and Fluid Flow,* vol. 31, no. 2, pp. 227-235, 2010.

[147] H. Kim, D. Kim, W. Kim, P. Chung and M. Jhon, "Langmuir Slip Model for Air Bearing Simulation Using the Lattice Boltzmann Method," *IEEE Transactions on Magnetics,* vol. 43, no. 6, pp. 2244-2246, June 2007.

[148] R. Myong, "Gaseous slip models based on the Langmuir adsorption isotherm," *Physics of Fluids,* vol. 16, no. 1, pp. 104-117, January 2004.

[149] J. Ren, P. Guo, Z. Guo and Z. Wang, "A Lattice Boltzmann Model for Simulating Gas Flow in Kerogen Pores," *Transp Porous Med,* vol. 106, pp. 285-301, 2015.

[150] X. Shan and H. Chen, "Lattice Boltzmann Model for Simulating Flows with Multi-phases and Components," *Physical Review E,* vol. 47, no. 3, pp. 1815-1819, 1993.

[151] N. Martys and H. Chen, "Simulation of multicomponent fluids in complex three-dimensional geometries by the lattice Boltzmann method," *Physical Review E,* vol. 53, no. 1, pp. 743-750, 1996.

[152] J. Wang, L. Chen, Q. Kang and S. Rahman, "Apparent permeability prediction of organic shale with generalized lattice Boltzmann model considering surface diffusion effect," *Fuel,* vol. 181, pp. 478-490, 2016.

[153] I. Langmuir, "The adsorption of gases on plane surfaces of glass, mica and platinum," *Journal of the American Chemical society,* vol. 40, no. 9, pp. 1361-1403, 1918.

[154] S. Cudjoe and R. Barati, "Lattice Boltzmann Simulation of CO2 Transport in Kerogen Nanopores - An Evaluation of CO2 Sequestration in Organic-Rich Shales," *Journal of Earth Science,* vol. 28, no. 5, pp. 926-932, 2017.